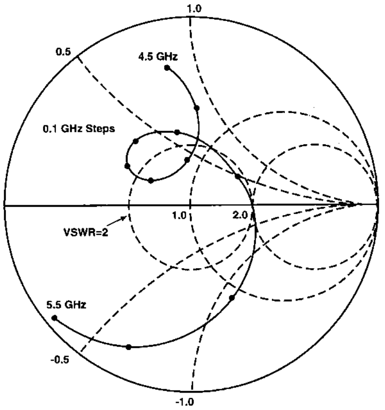

Applied Computational Electromagnetics Society Journal

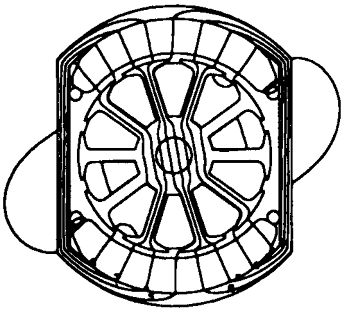

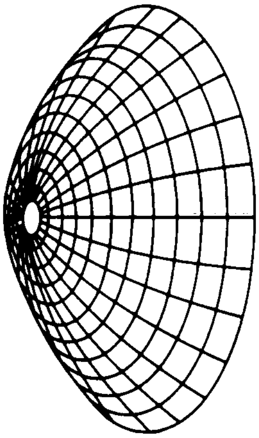

Editor-in-Chief
Atef Z. Elsherbeni

March 2003
Vol. 18 No. 1
ISSN 1054-4887

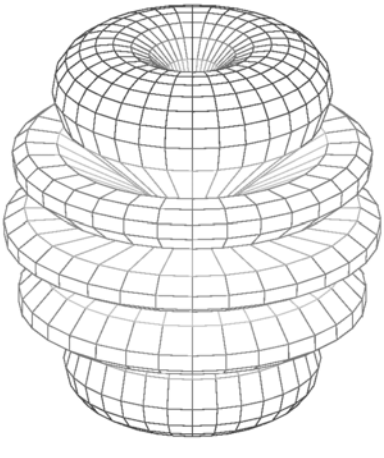

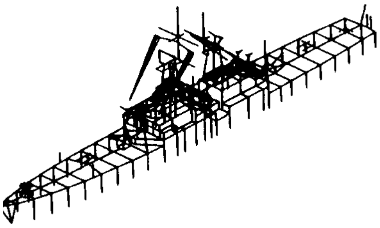

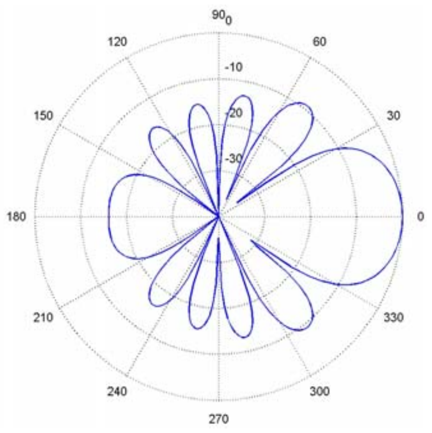

GENERAL PURPOSE AND SCOPE: The Applied Computational Electromagnetics Society ***(ACES)*** Journal hereinafter known as the ***ACES Journal*** is devoted to the exchange of information in computational electromagnetics, to the advancement of the state-of-the art, and the promotion of related technical activities. A primary objective of the information exchange is the elimination of the need to "re-invent the wheel" to solve a previously-solved computational problem in electrical engineering, physics, or related fields of study. The technical activities promoted by this publication include code validation, performance analysis, and input/output standardization; code or technique optimization and error minimization; innovations in solution technique or in data input/output; identification of new applications for electromagnetics modeling codes and techniques; integration of computational electromagnetics techniques with new computer architectures; and correlation of computational parameters with physical mechanisms.

SUBMISSIONS: The ***ACES Journal*** welcomes original, previously unpublished papers, relating to applied computational electromagnetics. Typical papers will represent the computational electromagnetics aspects of research in electrical engineering, physics, or related disciplines. However, papers which represent research in applied computational electromagnetics itself are equally acceptable.

Manuscripts are to be submitted through the upload system of ***ACES*** web site http://aces.ee.olemiss.edu See "Information for Authors" on inside of back cover and at ***ACES*** web site. For additional information contact the Editor-in-Chief:

Dr. Atef Elsherbeni
Department of Electrical Engineering
The University of Mississippi
University, MS 386377 USA
Phone: 662-915-5382 Fax: 662-915-7231
Email: atef@olemis.edu

SUBSCRIPTIONS: All members of the Applied Computational Electromagnetics Society who have paid their subscription fees are entitled to receive the ***ACES Journal*** with a minimum of three issues per calendar year and are entitled to download any published journal article available at http://aces.ee.olemiss.edu.

Back issues, when available, are $15 each. Subscriptions to ***ACES*** is through the web site. Orders for back issues of the ***ACES Journal*** and changes of addresses should be sent directly to ***ACES*** Executive Officer:

Dr. Richard W. Adler
ECE Department, Code ECAB
Naval Postgraduate School
833 Dyer Road, Room 437
Monterey, CA 93943-5121 USA
Fax: 831-649-0300
Email: *rwa@attglobal.net*

Allow four week's advance notice for change of address. Claims for missing issues will not be honored because of insufficient notice or address change or loss in mail unless the Executive Officer is notified within 60 days for USA and Canadian subscribers or 90 days for subscribers in other countries, from the last day of the month of publication. For information regarding reprints of individual papers or other materials, see "Information for Authors".

LIABILITY. Neither ***ACES***, nor the ***ACES Journal*** editors, are responsible for any consequence of misinformation or claims, express or implied, in any published material in an ***ACES Journal*** issue. This also applies to advertising, for which only camera-ready copies are accepted. Authors are responsible for information contained in their papers. If any material submitted for publication includes material which has already been published elsewhere, it is the author's responsibility to obtain written permission to reproduce such material.

APPLIED COMPUTATIONAL ELECTROMAGNETICS SOCIETY JOURNAL

Editor-in-Chief
Atef Z. Elsherbeni

March 2003
Vol. 18 No. 1

ISSN 1054-4887

The ACES Journal is abstracted in INSPEC, in Engineering Index, and in DTIC.

The first, fourth, and sixth illustrations on the front cover have been obtained from the Department of Electrical Engineering at the University of Mississippi.

The third and fifth illustrations on the front cover have been obtained from Lawrence Livermore National Laboratory.

The second illustration on the front cover has been obtained from FLUX2D software, CEDRAT S.S. France, MAGSOFT Corporation, New York.

THE APPLIED COMPUTATIONAL ELECTROMAGNETICS SOCIETY
http//:aces.ee.olemiss.edu

ACES JOURNAL EDITORS

EDITOR-IN-CHIEF/ACES
Andrew F. Peterson
Georgia Institute of Technology
Atlanta, GA, 30332-0250, USA

EDITORIAL ASSISTANT
Matthew J. Inman
University of Mississippi, EE Dept.
University, MS 38677, USA

EDITOR-IN-CHIEF, EMERITUS
David E. Stein
USAF Scientific Advisory Board
Washington, DC 20330, USA

EDITOR-IN-CHIEF/JOURNAL
Atef Elsherbeni
University of Mississippi, EE Dept.
University, MS 38677, USA

EDITOR-IN-CHIEF, EMERITUS
Ducan C. Baker
EE Dept. U. of Pretoria
0002 Pretoria, South Africa

EDITOR-IN-CHIEF, EMERITUS
Allen Glisson
University of Mississippi, EE Dept.
University, MS 38677, USA

MANAGING EDITOR
Richard W. Adler
833 Dyer Rd, Rm 437 EC/AB
NPS, Monterey, CA 93943-5121, USA

EDITOR-IN-CHIEF, EMERITUS
Robert M. Bevensee
Box 812
Alamo, CA 94507-0516, USA

EDITOR-IN-CHIEF, EMERITUS
Ahmed Kishk
University of Mississippi, EE Dept.
University, MS 38677, USA

ACES JOURNAL ASSOCIATE EDITORS

Giandomenico Amendola
Universita' della Calabria
Rende , Italy

John Beggs
NASA Langley Research Center
Hampton, VA, USA

John Brauer
Ansoft Corporation
Milwaukee, WI, USA

Magda El-Shenawee
University of Arkansas
Fayetteville AR, USA

Pat Foster
Microwave & Antenna Systems
Gt. Malvern, Worc. UK

Cynthia M. Furse
Utah State University
Logan UT, USA

Christian Hafner
Swiss Federal Inst. of Technology
Zurich, Switzerland

Michael Hamid
University of South Alabama,
Mobile, AL, USA

Andy Harrison
Radiance
Huntsville, AL

Chun-Wen Paul Huang
Anadigics, Inc.
Warren, NJ, USA

Todd H. Hubing
University of Missouri-Rolla
Rolla, MO, USA

Nathan Ida
The University of Akron
Akron, OH, USA

Yasushi Kanai
Niigata Institute of Technology
Kashiwazaki, Japan

Leo C. Kempel
Michigan State University
East Lansing MI, USA

Andrzej Krawczyk
Institute of Electrical Engineering
Warszawa, Poland

Stanley Kubina
Concordia University
Montreal, Quebec, Canada

Samir F. Mahmoud
Kuwait University
Safat, Kuwait

Ronald Marhefka
Ohio State University
Columbus, OH, USA

Edmund K. Miller
LASL
Santa Fe, NM, USA

Krishna Naishadham
Wright State University
Dayton, OH, USA

Giuseppe Pelosi
University of Florence
Florence, Italy

Vicente Rodriguez
ETS-Lindgren
Cedar Park, TX, USA

Harold A. Sabbagh
Sabbagh Associates
Bloomington, IN, USA

John B. Schneider
Washington State University
Pullman, WA, USA

Abdel Razek Sebak
University of Manitoba
Winnipeg, MB, Canada

Amr M. Sharawee
American University
Cairo, Egypt

Norio Takahashi
Okayama University
Tsushima, Japan

THE APPLIED COMPUTATIONAL ELECTROMAGNETICS SOCIETY

JOURNAL

Vol. 18 No. 1 March 2003

TABLE OF CONTENTS

APPLICATION OF HIERARCHICAL HIGHER-ORDER TANGENTIAL VECTOR FINITE ELEMENTS IN A HYBRID FEM/MOM METHOD

Hao Wang, ChunLei Guo, and Todd H. Hubing
Department of Electrical and Computer Engineering
University of Missouri-Rolla
Rolla, MO 65409

ABSTRACT

Hybrid FEM/MoM methods combine the finite element method (FEM) and the method of moments (MoM) to model inhomogeneous unbounded problems. These two methods are coupled by enforcing field continuity on the boundary that separates the FEM and MoM regions. Hierarchical higher-order tangential vector finite elements (TVFE's) are of practical interest because they can be easily combined with low-order elements to improve the accuracy of numerical solutions. This paper presents a hybrid FEM/MoM formulation applying a set of hierarchical TVFE's developed by Webb and Forghani. Higher-order FEM elements are coupled to MoM elements based on *Rao-Wilton-Glisson (RWG)* functions. The FEM matrix assembly procedure is described in sufficient detail to aid other investigators who wish to develop codes employing this technique. Three practical electromagnetic problems are presented that demonstrate the advantages of the higher-order elements.

I. INTRODUCTION

The hybrid finite-element-method and method-of-moments (FEM/MoM) can be used to analyze many kinds of electromagnetic problems effectively by applying FEM to model the fields in regions with geometric complexity and using MoM to model larger, simpler structures outside this region and to provide an accurate radiation boundary condition (RBC) to terminate the FEM mesh. Both the MoM and FEM are powerful methods, but each of these methods has its own advantages and disadvantages. MoM handles unbounded problems very effectively but is less efficient when complex inhomogeneities are present. Inhomogeneities are easily handled by the FEM, which requires less computer time and storage. However, the FEM is most suitable for bounded problems. Hence, hybrid FEM/MoM methods that combine MoM and FEM are advantageous for treating electromagnetic problems involving unbounded, complex structures.

Conventional hybrid FEM/MoM codes employ linear tangential vector finite elements (TVFE's). These elements are commonly referred to as Whitney elements defined by Nedelec [1]. Because the functions do not impose normal component continuity between tetrahedra, they do not produce the spurious modes that can be generated by using node-based elements [2]. However, these elements limit the accuracy of the finite element solution since they only support a constant tangential value along element edges and a linear field variation inside the element (CT/LN). Thus, when electric fields in a certain region vary quickly, the number of tetrahedra has to be relatively high to obtain reasonable accuracy. Higher-order elements that support non-linear field variations can be used to model rapidly varying fields using fewer elements. One set of higher-order basis functions for tetrahedra supports a linear tangential, quadratic normal (LT/QN) representation of the fields. Basis functions of the next higher order have a quadratic tangential, cubic normal (QT/CuN) representation for the fields. A set of TVFE's is referred to as interpolatory if values within the element can be interpolated from node or edge values. It is referred to as hierarchical if the lower-order basis functions are a subset of the higher order basis functions. Webb and Forghani [3], Savage and Peterson [4], Graglia *et al.* [5], and Andersen and Volakis [6] have employed LT/QN basis functions. The TVFE's presented in [4] and [5] are interpolatory while those presented in [3] and [6] form a hierarchical set with the Whitney TVFE. Hierarchical sets of TVFE's allow for selective field expansion using different order elements in different regions of the computational domain. Hence, for the regions where the fields vary slowly, the lowest order TVFE's can be employed, while for the regions where the fields vary rapidly, higher-order TVFE's can be employed. This can save memory and CPU time without compromising computational accuracy. Andersen developed and applied mixed-order hierarchical TVFE's in [7].

For MoM techniques based on EFIE formulations, Nedelec [1] presented a general family of divergence-conforming functions whose lowest-order member was a set of CN/LT basis functions, known as *Rao-Wilton-Glisson (RWG)* or *triangular rooftop* functions. These functions are widely used for representing surface currents in EFIE formulations.

In a hybrid FEM/MoM technique, hierarchical sets of TVFE's are readily coupled to linear MoM boundary elements because the coefficients corresponding to any higher-order terms on the boundary can be set to zero to enforce the continuity of the tangential fields.

The coefficient matrices generated by FEM/MoM codes may have large condition numbers. When LT/QN basis functions are used in the FEM, the condition numbers of the hybrid matrix generally become much larger. Savage [8] showed that interpolatory vector basis functions are generally better conditioned than hierarchical vector basis functions. However, only the condition numbers of individual element matrices were studied in [8]. Andersen [9] examined the inter-relationships between the condition numbers of element and global matrices based on various interpolatory and hierarchical TVFE's using a cavity resonator example. However because they were solving for the eigenvalues of a cavity resonator, the condition numbers of the global FEM matrices were not considered.

In this paper, the hybrid FEM/MoM formulation using the LT/QN TVFE's described by Webb and Forghani in [3] is developed and applied to different electromagnetic problems. Section II presents the hybrid FEM/MoM formulation. Section III presents the FEM matrix assembly procedure for LT/QN TVFE's. Section IV presents a set of numerical results that demonstrates the improved performance of the higher-order TVFE in the context of the 3-D hybrid FEM/MoM.

II. FORMULATION

In the hybrid FEM/MoM, an electromagnetic problem is divided into an interior equivalent part and an exterior equivalent part. The interior part is modeled using the FEM and the exterior part is modeled using a surface integral equation method-of-moments technique (MoM). The two equivalent parts are coupled by enforcing the continuity of tangential fields on the FEM and MoM boundary [10].

2.1 The Finite Element Method Using Higher - Order TVFE's

FEM can be used to analyze the interior equivalent part by solving the weak form of the vector wave equation as follows [7]:

$$\int_V \left[\left(\frac{\nabla \times \mathbf{E}(\mathbf{r})}{j\,\omega\,\mu_0\,\mu_r} \right) \bullet (\nabla \times \mathbf{w}(\mathbf{r})) + j\,\omega\,\varepsilon_0 \varepsilon_r \mathbf{E}(\mathbf{r}) \bullet \mathbf{w}(\mathbf{r}) \right] dV$$

$$= \int_S (\hat{n} \times \mathbf{H}(\mathbf{r})) \bullet \mathbf{w}(\mathbf{r})\, dS - \int_V \mathbf{J}^{\mathrm{int}}(\mathbf{r}) \bullet \mathbf{w}(\mathbf{r})\, dV \qquad (1)$$

where S is the surface enclosing volume V, $\mathbf{w(r)}$ is the weighting function, and $\mathbf{J}^{\mathrm{int}}$ is an impressed source. Equation (1) shows that efficient finite-element analysis of electromagnetic fields in 3-D regions requires computation of two element matrices. These two matrices are

$$E_{ij} = \int_V \nabla \times \mathbf{w}_i \bullet \nabla \times \mathbf{w}_j \, dV \qquad (2)$$

$$F_{ij} = \int_V \mathbf{w}_i \bullet \mathbf{w}_j \, dV \qquad (3)$$

where $\mathbf{w}_i$ represents the i*th* vector basis function and V indicates integration over one tetrahedron. The six edges and four faces of a tetrahedron are numbered as indicated in Table 1 and Figure 1 [4].

Table 1. Node and edge numbering scheme of a tetrahedron

Edge#	Node 1	Node 2	
1	1	2	
2	1	3	
3	1	4	
4	2	3	
5	2	4	
6	3	4	
Face#	Node 1	Node 2	Node 3
1	1	2	3
2	1	2	4
3	1	3	4
4	2	3	4

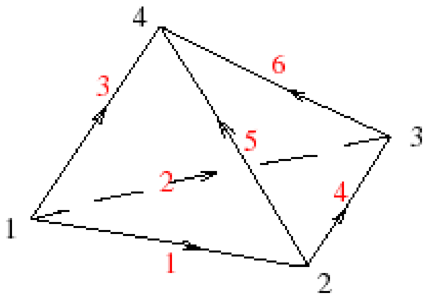

Figure 1. Edge and face definition of a tetrahedron.

The linear-tangential, quadratic-normal (LT/QN) basis functions developed by Webb exist in two forms. One is edge-based functions, which are associated with tetrahedron edges. The other is face-based functions, which are associated with tetrahedron faces. The two edge-based LT/QN basis functions associated with edge *i* are,

$$\mathbf{w}_k^{\mathbf{e1}} = l_k (L_{k1} \nabla L_{k2} - L_{k2} \nabla L_{k1}) \quad k = 1, \cdots, 6 \qquad (4)$$

$$\mathbf{w}_k^{\mathbf{e2}} = l_k (L_{k1} \nabla L_{k2} + L_{k2} \nabla L_{k1}) \quad k = 1, \cdots, 6 \qquad (5)$$

where "e1" represents the first type of edge basis function, and "e2" represents the second type of edge basis function. L_i is the area coordinate associated with the node *i.* It is unity at node *i* and decays in a linear fashion to zero at the other three nodes of the cell. l_i is the length of edge i.

Figure 2 shows vector plots of the edge-based functions in a face of a tetrahedron. The two face-based elements associated with face *i* are,

$$\mathbf{w}_i^{\mathrm{f1}} = L_{i1}L_{i2}\nabla L_{i3} - L_{i1}L_{i3}\nabla L_{i2} \quad i = 1,\cdots 4 \tag{6}$$

$$\mathbf{w}_i^{\mathrm{f2}} = L_{i1}L_{i2}\nabla L_{i3} - L_{i2}L_{i3}\nabla L_{i1} \quad i = 1,\cdots 4 \tag{7}$$

where "*f1*" represents the first type of face basis function, and "*f2*" represents the second type of face basis function. Figure 3 shows vector plots of the face-based functions on a face of a tetrahedron. It shows that the field distributions in *f1* elements and *f2* elements are similar but they rotate in different directions.

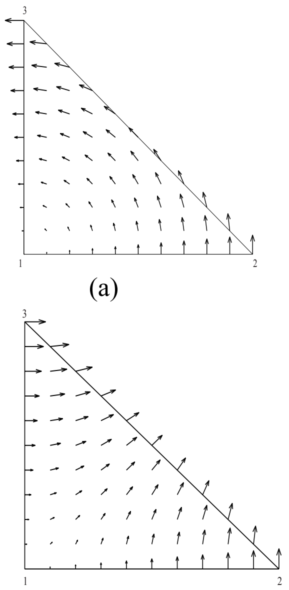

(b)

Figure 2. Plot of the edge based basis functions. (a) $\mathbf{w}_i^{\mathrm{e1}}$, (b) $\mathbf{w}_i^{\mathrm{e2}}$.

Using these basis functions, the electric field **E** in the interior region can be expanded as the sum of four terms,

$$\mathbf{E(r)} = \sum_{k=1}^{N_v}(E_k^{\mathrm{e1}}\mathbf{w}_k^{\mathrm{e1}} + E_k^{\mathrm{e2}}\mathbf{w}_k^{\mathrm{e2}} + E_k^{\mathrm{f1}}\mathbf{w}_k^{\mathrm{f1}} + E_k^{\mathrm{f2}}\mathbf{w}_k^{\mathrm{f2}}) \cdot \tag{8}$$

The basis function $\mathbf{w}_k$ has the following properties:

$$\mathbf{e}_k \bullet \mathbf{w}_k^{\mathrm{e1}} = l_k \frac{L_{k1} + L_{k2}}{l_k} = L_{k1} + L_{k2} = 1 \tag{9}$$

$$\mathbf{e}_k \bullet \mathbf{w}_k^{\mathrm{e2}} = l_k \frac{L_{k1} - L_{k2}}{l_k} = L_{k1} - L_{k2} \tag{10}$$

where $\mathbf{e}_k$ is a unit edge vector corresponding to the k^{th} edge. Hence, the terms associated with "*e1*" elements can be viewed as the *main* terms that describe fields along tetrahedron edges roughly, while the terms associated with "*e2*" elements can be viewed as *adjustment* terms that describe the field's linear variation along tetrahedron edges.

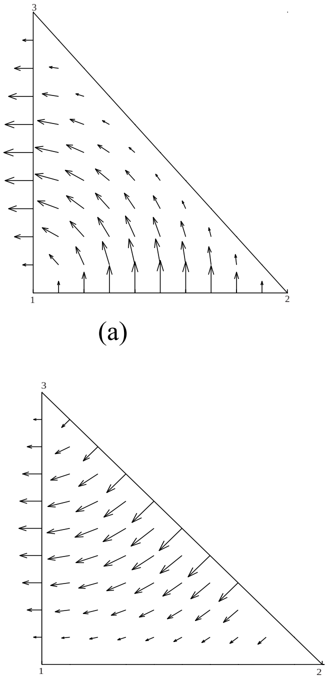

(b)

Figure 3. Plot of the face based basis functions, (a) $\mathbf{w}_i^{\mathrm{f1}}$, (b) $\mathbf{w}_i^{\mathrm{f2}}$.

Since CT/LN functions have one unknown per edge, they generate 6×6 local matrices. LT/QN functions have two unknowns per edge and two unknowns per face so they generate 20×20 local matrices. Applying the LT/QN basis functions to (1), a global FEM matrix can be constructed as follows,

$$\begin{bmatrix} A_{ii}^{\mathrm{e1e1}} & A_{id}^{\mathrm{e1e1}} & A_{ii}^{\mathrm{e1e2}} & A_{ii}^{\mathrm{e1f}} \\ A_{di}^{\mathrm{e1e1}} & A_{dd}^{\mathrm{e1e1}} & A_{di}^{\mathrm{e1e2}} & A_{di}^{\mathrm{e1f}} \\ A_{ii}^{\mathrm{e2e1}} & A_{id}^{\mathrm{e2e1}} & A_{ii}^{\mathrm{e2e2}} & A_{ii}^{\mathrm{e2f}} \\ A_{ii}^{\mathrm{fe1}} & A_{id}^{\mathrm{fe1}} & A_{ii}^{\mathrm{fe2}} & A_{ii}^{\mathrm{ff}} \end{bmatrix} \begin{bmatrix} E_i^{\mathrm{e1}} \\ E_d^{\mathrm{e1}} \\ E_i^{\mathrm{e2}} \\ E_i^{\mathrm{f}} \end{bmatrix} =$$

$$\begin{bmatrix} 0 & 0 \\ 0 & B_{dS} \end{bmatrix} \begin{bmatrix} 0 \\ J_S \end{bmatrix} + \left[g^{\mathrm{int}} \right]. \tag{11}$$

The unknown coefficients $[E_n]$ are partitioned into four types according to their corresponding basis functions and edge functions. The four categories are interior edges of "*e1*" type, which are denoted by the subscript *i*, dielectric boundary edges of type "*e1*", which are denoted by the subscript *d,* interior edges of type "*e2*", and interior faces of type "*f*", which are also denoted by the subscript *i*. The type "*f1*" and type "*f2*" basis functions have been combined into one common "*f*" type because they are essentially the same when they share the same face and rotate along the same edge. E_k^{e2}, E_k^{f1} and E_k^{f2} are set equal to zero on the MoM boundary to enforce the continuity of the tangential electric fields. Using this approach, the MoM part (employing linear basis functions) does not have to be modified to work with FEM elements of different order. $[J_s]$ is a set of unknown complex scalar coefficients for the surface electric current densities on the FEM and MoM boundary *S*. $[g^{\mathrm{int}}]$ is the source term, representing sources located within the FEM region. The elements of $[A]$, $[B_{dS}]$, and $[g^{\mathrm{int}}]$ are given by,

$$A_{mn} = \int_V [\frac{(\nabla \times \mathbf{w_n}(\mathbf{r})) \bullet (\nabla \times \mathbf{w_m}(\mathbf{r}))}{j\omega\mu_0\mu_r} + j\omega\varepsilon_0\varepsilon_r \mathbf{w}_{\mathrm{n}}(\mathbf{r}) \bullet \mathbf{w}_{\mathrm{m}}(\mathbf{r})] dV \tag{12}$$

$$B_{mn} = \int_{S_d} \mathbf{f_n}(\mathbf{r}) \bullet \mathbf{w_m}(\mathbf{r}) dS \tag{13}$$

$$g_m^{\mathrm{int}} = -\int_V \left[\mathbf{J}^{\mathrm{int}} + \frac{1}{j\,\omega\,\mu_0\,\mu_r} \left(\nabla \times \mathbf{M}^{\mathrm{int}} \right) \right] \bullet \mathrm{w}_{\mathrm{m}}(\mathbf{r})\, dV\ . \tag{14}$$

2.2 The MoM Using EFIE

The exterior equivalent part can be analyzed using the EFIE [8].

$$\frac{\mathbf{E}(\mathbf{r})}{2} = \mathbf{E}^{\mathrm{inc}}(\mathbf{r}) + \int_S [-\mathrm{M}(\mathbf{r}') \times \nabla' \mathrm{G}_0(\mathbf{r}, \mathbf{r}') - j\, k_0 \eta_0 \mathbf{J}(\mathbf{r}') \mathbf{G_0}(\mathbf{r}, \mathbf{r}') + j \frac{\eta_0}{k_0} \nabla' \bullet \mathbf{J}(\mathbf{r}') \nabla' \mathbf{G_0}(\mathbf{r}, \mathbf{r}')] dS \tag{15}$$

The equivalent surface electric current **J(r)** and magnetic current **M(r)** in (15) can be discretized using the *Rao-Wilton-Glisson* basis function **f(r)** [9].

$$\mathbf{J}(\mathbf{r}) = \sum_{\mathrm{n}=1}^{\mathrm{N}_S} (J_s)_{\mathrm{n}} \mathbf{f}_{\mathrm{n}}(\mathbf{r}) \tag{16}$$

$$\mathbf{M}(\mathbf{r}) = \sum_{\mathrm{n}=1}^{\mathrm{N}_d} \left(E_d^{\mathrm{e1}}\right)_{\mathrm{n}} \mathbf{f}_{\mathrm{n}}(\mathbf{r}) \tag{17}$$

where N*s* is the total number of edges on the FEM and MoM boundary *S*, and N*d* is the total number of edges on the dielectric boundary S*d*. **E(r)** in Equation (15) can be expanded using the tetrahedral CT/LN basis function $\mathbf{w}^{\mathrm{e1}}(\mathbf{r})$ as follows,

$$\mathbf{E}(\mathbf{r}) = \sum_{\mathrm{n}=1}^{\mathrm{N}_d} \left(E_d^{\mathrm{e1}}\right)_{\mathrm{n}} \mathbf{w}_{\mathrm{n}}^{\mathrm{e1}}(\mathbf{r}) \tag{18}$$

On the surface *S*, the triangular basis function **f(r)** and the CT/LN basis function $\mathbf{w}^{\mathrm{e1}}(\mathbf{r})$ are related by,

$$\mathbf{w}^{\mathrm{e1}}(\mathbf{r}) = \hat{n} \times \mathbf{f}(\mathbf{r})\,. \tag{19}$$

After multiplying by weighting functions $\mathbf{f_n}(\mathbf{r})$, n=1, ... N, the EFIE in Equation (15) can be discretized as follows,

$$[C][J_s] = [D]\left[E_d^{\mathrm{e1}}\right] - \left[F^i\right]. \tag{20}$$

2.3 The Hybridization of FEM and MoM

Equations (11) and (20) form a coupled and determined system. Three different formulations, *the combined formulation*, *the inward-looking formulation and the outward-looking formulation*, can be used to solve the coupled system [11], [14]. The outward-looking formulation was used for the examples in this paper. From (20),

$$J_s = C^{-1} D\, E_d^{\mathrm{e1}} - C^{-1} F^i\,. \tag{21}$$

Substituting Equation (21) into Equation (11) yields a determined matrix equation,

$$\begin{bmatrix} A_{ii}^{\mathrm{e1e1}} & A_{id}^{\mathrm{e1e1}} & A_{ii}^{\mathrm{e1e2}} & A_{ii}^{\mathrm{e1f}} \\ A_{di}^{\mathrm{e1e1}} & A_{dd}^{\mathrm{e1e1}} - B_{dS} C^{-1} D & A_{di}^{\mathrm{e1e2}} & A_{di}^{\mathrm{e1f}} \\ A_{ii}^{\mathrm{e2e1}} & A_{id}^{\mathrm{e2e1}} & A_{ii}^{\mathrm{e2e2}} & A_{ii}^{\mathrm{e2f}} \\ A_{ii}^{\mathrm{fe1}} & A_{id}^{\mathrm{fe1}} & A_{ii}^{\mathrm{fe2}} & A_{ii}^{\mathrm{ff}} \end{bmatrix} \begin{bmatrix} E_i^{\mathrm{e1}} \\ E_d^{\mathrm{e1}} \\ E_i^{\mathrm{e2}} \\ E_i^{\mathrm{f}} \end{bmatrix} = \begin{bmatrix} g_{\mathrm{int}}^{\mathrm{e1}} \\ g_{\mathrm{int}}^{\mathrm{e2}} \\ g_{\mathrm{int}}^{\mathrm{f}} \end{bmatrix} + \left[B_{dS} C^{-1} F^i\right] \tag{22}$$

Equation (22) can be solved using iterative solvers. The preconditioning technique reported in [14] can be used to improve the convergence rate and accuracy of the iterative solvers.

III. ASSEMBLY

The aim of the assembly procedure in FEM is to construct the global matrix (11) by summing the element matrix terms for each tetrahedron in the mesh while guaranteeing continuity of the tangential electric field on the boundary between any two tetrahedra. For CT/LN basis functions, the assembly procedure is relatively straight-forward. However, for LT/QN basis functions, more details have to be considered in order to get the correct global matrix. This section describes the assembly procedure for LT/QN TVFE's.

For "*e1*" elements, Equation (4) and Figure 2(a) indicate that the complex scalar E_k^{e1} is the projection of the electric field onto the k^{th} edge. When the local edge vector (as defined in Table 1) is reversed, Equation (4) will be reversed at the same time. Therefore, to ensure the continuity of the tangential electric field across all edges, a unique global edge direction must be defined (e.g. always pointing from the smaller node number to the larger node number). Equation (4) must be multiplied by (-1) if the local edge vector does not have the same direction as the global edge direction.

For "*e2*" elements, the continuity of the tangential electric field across all edges must also be satisfied. From Figure 2 (b) and Equation (5), it is clear that when the local edge vector is reversed, there is no change in Equation (5). Therefore Equation (5) should not be multiplied by (-1) even when the local edge vector does not have the same direction as the global edge direction. When a FEM edge is on the boundary between FEM and MoM, E_k^{e2} associated with this edge is set to zero.

For "*f1*" and "f2" elements, the continuity of the tangential field needs to be enforced across all faces. From Figure 3, two local E_k^{f} can be regarded as a common global unknown only if they share the same face and rotate along the same edge. When the local edge vector, as defined in Table 1, is reversed, Equation (6) and Equation (7) will be reversed at the same time. Therefore, Equation (6) and Equation (7) should be multiplied by (-1) if the local edge vector does not have the same direction as the global edge direction.

As illustrated in Figure 4, there are generally four kinds of faces. In (a), the three edges of the face are all within the FEM volume. In (b), one or two edges of the face are on the FEM/MoM boundary. In (c), the three edges of the face are all on the FEM/MoM boundary while the area of the face is located in the FEM volume. In (d), the three edges and the area of the face are all on the FEM and MoM boundary. Normally, at the interface between higher-order FEM elements and CN/LT MoM elements, the higher-order terms, E_k^{f}, are set to zero. However, for the faces of type (a), (b) and (c), the complex scalar E_k^{f} rotating along the edge that is located on the FEM/MoM boundary, represents fields within the FEM volume and cannot be set to zero. Allowing these terms to have a non-zero value will not affect the coupling between FEM and MoM, since their projection on the boundary is equal to zero. For the faces of type (d), complex scalars E_k^{f1} and E_k^{f2} corresponding to this type must be set to zero.

IV. NUMERICAL RESULTS

This section describes three examples illustrating the performance of the hybrid FEM/MoM with CT/LN and LT/QN FEM basis functions. All matrices were solved using a biconjugate gradient stabilized solver [11]. A 750-MHz Pentium III computer was used to perform the computation.

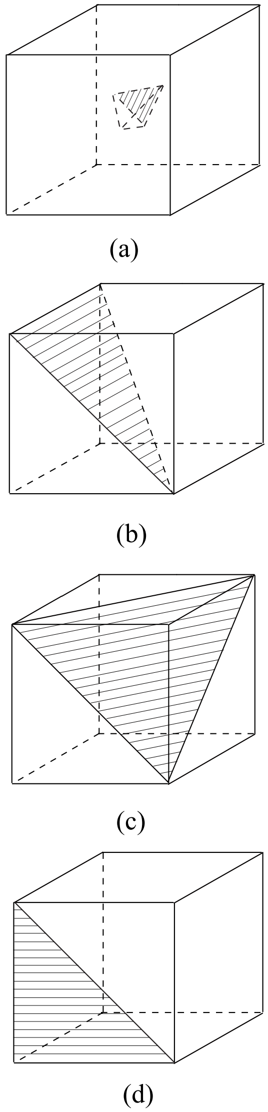

(a)

(b)

(c)

(d)

Figure 4. Faces in a tetrahedron.

4.1 The Scattered Field from a Sphere

This example models the scattering of an electromagnetic plane wave by a dielectric sphere. As shown in Figure 5, the radius of the sphere is 0.09 m and the relative permittivity is 4.5. The incident wave propagates in the $+\hat{z}$ direction. The wave has amplitude E_0 and is polarized in the $\hat{x}$ direction,

$$\mathbf{E}(x,y,z,t)=E_0\mathbf{e}_x e^{j(wt-\beta z)}. \qquad (23)$$

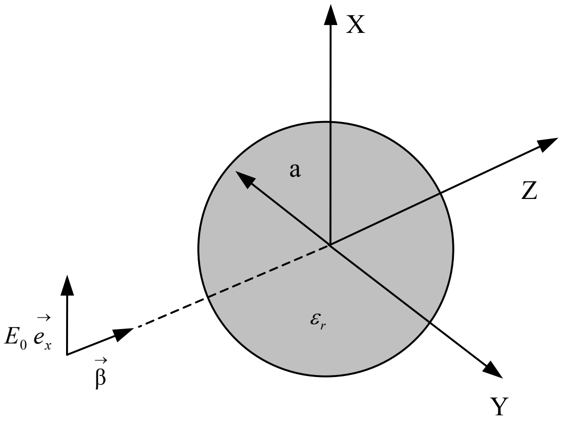

Figure 5. Scattered field from a dielectric sphere.

A commercial software package was used to discretize the FEM volume with different densities to demonstrate the advantages of the proposed higher-order TVFE's. The MoM boundary was chosen to coincide with the physical boundary of the dielectric sphere. The number of MoM basis functions was fixed during the whole process. For validation, results using the Mie series [15] were compared to the FEM/MoM results. In Figure 6, we compare results for the three-dimensional bistatic scattering cross section at a frequency of 583 MHz. The Mie series result is denoted "Mie." For a mesh with a small number of tetrahedra, the result using the CT/LN TVFE is denoted "CT/LN TVFE coarse," and the result using the LT/QN TVFE is denoted "LT/QN TVFE coarse." For a mesh with a larger number of tetrahedra, the result using the CT/LN TVFE is denoted "CT/LN TVFE dense."

In Figure 6, the "CT/LN TVFE coarse" result is seen to compare fairly well with the exact Mie series result when the observation angle is between 100 degrees and 180 degrees. When the observation angle is below 100 degrees, a 1-dB discrepancy can be seen because the mesh is relatively coarse. For the denser mesh, the "CT/LN TVFE dense" result shows a significant improvement. By keeping the original coarse mesh and applying the LT/QN basis functions, the "LT/QN TVFE coarse" result agrees with the exact result very well. Even compared with the "CT/LN TVFE dense" result, the "LT/QN TVFE result" is closer to the exact result. Table 2 presents relevant parameters for the three results. Improved accuracy is obtained with less computer resources using LT/QN FEM basis functions.

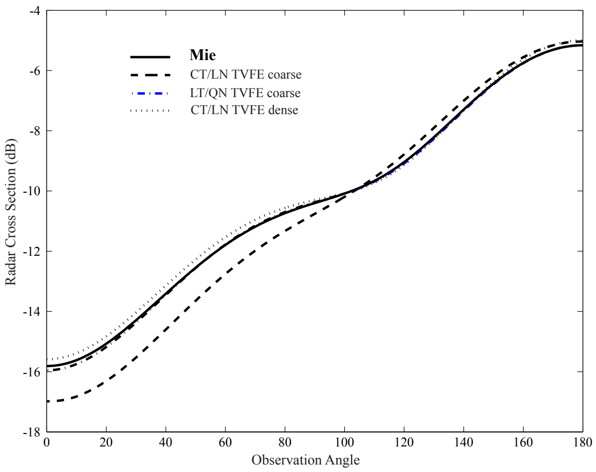

Figure 6. Bistatic RCS of the dielectric sphere at 583 MHz.

Table 2. Comparison between the results in Fig. 6

FEM Part	FEM Unkno-wns	MoM Unkno-wns	Average Edge Length (mm)	FEM Matrix Non - zeros	Solver Time (sec)
CT/LN Coarse	405	346	9.1	2379	28
CT/LN Dense	3266	346	4.3	18336	275
LT/QN Coarse	2430	346	9.1	51052	213

4.2 Input Impedance of a Power Bus Structure

This example models a printed circuit board (PCB) power bus structure. As shown in Figure 7, the board dimensions are 7.6 cm × 5.1 cm × 1.1 mm. The top and bottom planes are perfect electric conductors (PECs). The dielectric between the PEC layers has a relative permittivity of 3.81(1-j0.01). The MoM boundary is chosen to coincide with the physical boundary of the board. A source is identified at the location shown in Figure 7.

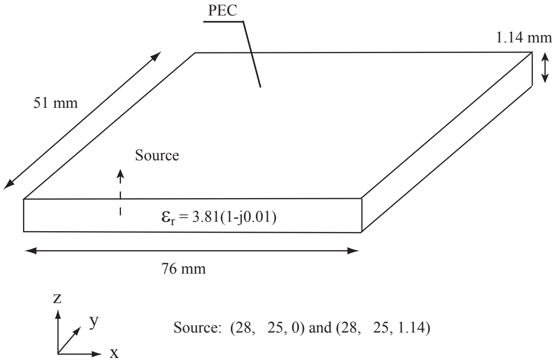

Figure 7. A PCB power bus structure.

Unlike the previous example, the fields in this configuration are relatively uniform. The electric field in the FEM region is vertically oriented and constant in the vertical direction. It is not obvious that a higher-order FEM element would benefit the analysis of this configuration.

The FEM uses a current filament on tetrahedron edges to model sources located within the FEM region [16]. A current source along the z-axis can be expressed as,

$$\mathbf{J}^{\text{int}} = I\delta(x - x_f)\delta(y - y_f)\hat{\mathbf{z}} \tag{24}$$

where (x_f, y_f) specifies its position, I denotes the electric current magnitude, and $\delta(x)$ is the Dirac delta function. The contribution to vector [g^{int}] in Equation (24) is simply,

$$\mathbf{g}^{\text{int}} = I\iiint \hat{z}\bullet\{\mathbf{w}\}\delta(x - x_f)\delta(y - y_f)\,dxdydz\,\cdot \tag{25}$$

For an *e1* basis function,

$$\mathbf{g}_{\text{int}}^{\text{e1}} = I\int_0^l l_1^e \frac{L_1^e + L_2^e}{l_1^e}dz = I\int_0^l dz = Il\,\cdot \tag{26}$$

For an *e2* basis function,

$$\mathbf{g}_{\text{int}}^{\text{e2}} = I\int_0^l l_1^e \frac{L_1^e - L_2^e}{l_1^e}dz = 0\,\cdot \tag{27}$$

For *f1* and *f2* basis functions

$$\mathbf{g}_{\text{int}}^{\text{f}} = 0 \tag{28}$$

since the tangential components of these functions along element edges are zero.

The power bus structure can also be modeled analytically as a cavity with two PEC and four perfect magnetic conductor (PMC) walls. The analytical resonance frequencies are given as follows (for $\mu_r = 1.0$) [17],

$$f_{m,n} = \frac{c}{2\pi\sqrt{\varepsilon_r}}\sqrt{\left(\frac{m\pi}{a}\right)^2 + \left(\frac{n\pi}{b}\right)^2} \quad m,n = 0, 1, 2, \ldots \tag{29}$$

where a and b are the length and width of the cavity, respectively; m and n are the mode indices; c is the speed of light in free space; and ε_r is the relative permittivity of the material in the cavity. For this power bus structure, only TM_z modes are excited. From Equation (29), the TM_z (1,0) mode's resonance frequency is 1011.1 MHz and the TM_z (2,0) mode's resonance frequency is 2022.3 MHz.

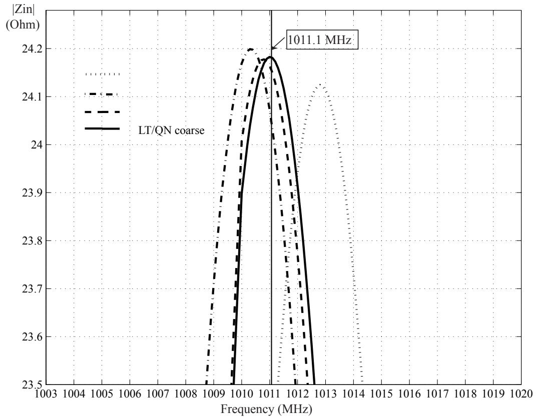

(a) TM_z (1,0) mode

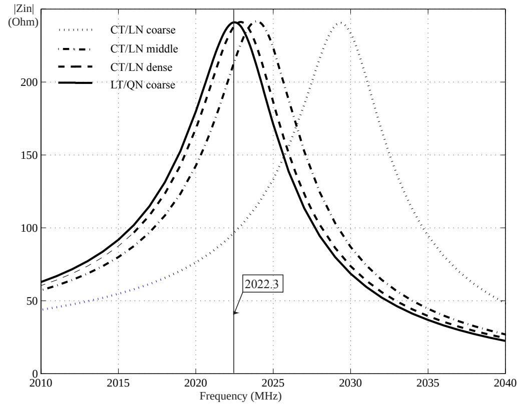

(b) TM_z (2,0)

Figure 8. Input impedance of the power bus structure.

In Figure 8, the computed input impedances of the power bus structure near these two resonance frequencies are compared. For a mesh with a number of tetrahedra between that of coarse mesh and dense mesh, the result using the CT/LN TVFE is denoted "CT/LN middle." The "LT/QN coarse" and "CT/LN coarse" examples employ the same mesh. It can be seen from Figure 8 that of the four cases, the "LT/QN coarse" results most accurately predict the resonance frequencies. Table 3 presents relevant parameters for the four cases. Once again the LT/QN coarse mesh yields more accurate results with fewer computer resources than a dense CT/LN mesh.

Table 3. Comparison between different formulations

Formulations	Unknowns	FEM non-zero	Solver time (sec)
CT/LN Coarse	467	4097	0.89
CT/LN Middle	1162	9940	1.54
CT/LN Dense	5041	42039	14.3
LT/QN Coarse	4124	87970	6.8

In [9], the inter-relationships between the condition numbers of individual elements as well as global matrices based on various interpolatory and hierarchical TVFE's were studied using a cavity resonator example. It was found that the LT/QN TVFE by Andersen and Volakis [7] resulted in better conditioned FEM matrices than the TVFE by Webb and Forghani. Since resonant structures like this power bus can be particularly susceptible to numerical error, this structure was also analyzed using higher-order elements based on the LT/QN elements in [7]. Figure 9 compares the condition numbers of the global FEM matrices generated by this example based on Andersen's and Webb's LT/QN basis functions. The term 'norm' denotes the normalized basis functions described in Appendix A. Up to 3 GHz, the LT/QN TVFE in [7] yields slightly better conditioned matrices than the TVFE in [5]. Normalized vector basis functions yield much smaller condition numbers than unnormalized vector basis functions.

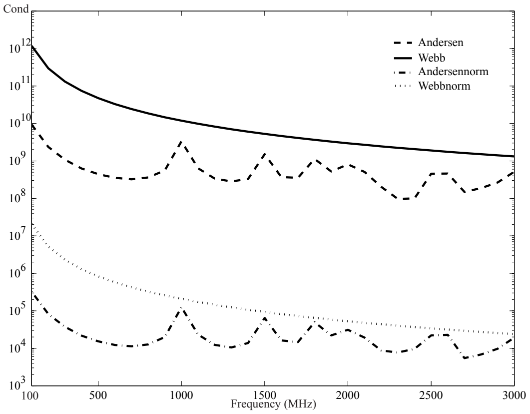

Figure 9. Condition numbers of the global FEM matrix based on different LT/QN basis functions.

4.3 Input Impedance of a Microstrip Structure

Numerical models of printed circuit board (PCB) geometries often include at least one microstrip structure (i.e. a trace over a plane). When these structures are modeled using a finite element technique with CT/LN basis elements, it is not uncommon to model the space between the trace and the plane with a single layer of elements. This approach generally yields good results when the trace is wide (e.g. the power bus structure) or when far-field results are calculated. However, for narrow traces or when calculating near-field properties (e.g. input impedance or crosstalk), a single layer of elements may not be adequate [16].

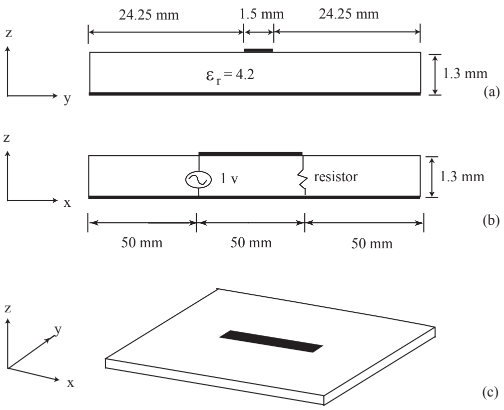

Figure 10. The geometry of a microstrip structure.

Figure 10 shows the geometry of a PCB with a thin trace. The trace width is only slightly greater than the trace height. The board is made of a dielectric with ε_r=4.2. The trace is excited by a current source at one end, and is terminated by a 47-ohm resistor at the other end. The MoM boundary is chosen to coincide with the physical boundary of the board.

The FEM code models load impedances Z_L as dielectric posts on tetrahedron edges [17]. Those posts have a finite conductivity given by

$$\sigma = \frac{l}{Z_L S} \tag{30}$$

where l is its length, and S is the cross sectional area. If the load is treated as a lumped element, its contribution to the finite element matrix is,

$$\left[A^{\mathrm{e1}}\right] = \frac{l}{Z_L S}\iiint \left\{\mathbf{w}^{\mathrm{e1}}\right\}\bullet\left\{\mathbf{w}^{\mathrm{e1}}\right\}^T \delta(x-x_L)(y-y_L)\,dxdydz = \frac{l^2}{Z_L} \tag{31}$$

for the *e1* basis function, and,

$$\begin{aligned}\left[A^{\mathrm{e2}}\right] &= \frac{l}{Z_L S}\iiint \left\{\mathbf{w}^{\mathrm{e2}}\right\}\bullet\left\{\mathbf{w}^{\mathrm{e2}}\right\}^T \delta(x-x_L)(y-y_L)\,dxdydz \\ &= \frac{l}{Z_L}\int_0^l (L_1-L_2)^2\,dz \\ &= \frac{l^2}{3Z_L}\end{aligned} \tag{32}$$

for the *e2* basis function, and,

$$\left[A^{\mathrm{f}}\right] = 0 \tag{33}$$

for the *f1* and *f2* basis functions. The electric field lines around the trace are illustrated in Figure 11 [18]. Since the electric field around the trace varies dramatically, the coarse mesh used to divide the FEM volume in the previous power bus example does not work here. Figure 11 also shows two meshes for a microstrip geometry. The coarse mesh is one element tall and the fine mesh is two elements tall.

Figure 12 shows the measured and calculated results for a 47-ohm termination up to 1 GHz. Note that the coarse mesh yields a poor result with CT/LN elements while the dense mesh results are close to the measured results. The LT/QN result with the coarse mesh also yields an accurate result.

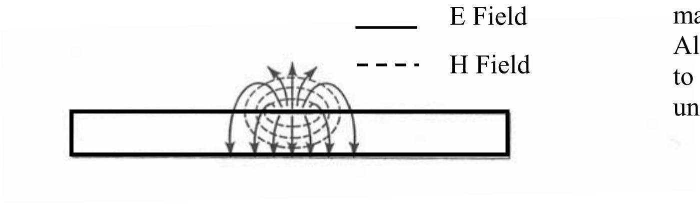

(a) Electric and magnetic field lines

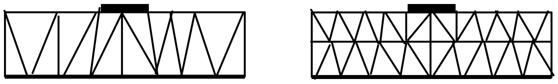

(b) Coarse Mesh (c) Fine Mesh

Figure 11. Cross-sectional view of the electric field and FEM meshes used to analyze the microstrip structure.

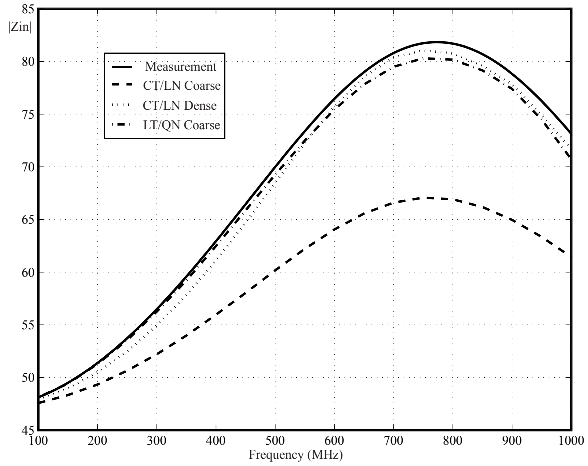

Figure 12. Input impedance of microstrip structure

VI. CONCLUSIONS

This paper presents a hybrid FEM/MoM formulation using higher-order (LT/QN) tangential vector finite elements. There are several kinds of LT/QN TVFE's. The basis functions developed by Webb and Forghani are applied here since they result in simpler derivations compared to other hierarchical higher-order basis functions. The properties of the LT/QN basis functions are discussed and compared to traditional CT/LN basis functions. Three examples demonstrate that higher-order basis functions are capable of providing more accurate results with a coarser tetrahedral mesh and less computational resources. The condition numbers of the global FEM matrices derived from a power bus structure on the basis of various hierarchical LT/QN basis functions are compared. It is confirmed that the TVFE by Andersen results in somewhat better conditioned matrices than the TVFE by Webb and Forghani. Also, normalized vector basis functions are observed to result in much smaller condition numbers than unnormalized vector basis functions.

REFERENCES

[1] J. C. Nedelec, "Mixed finite elements in R3," *Num. Math.*, vol. 35, pp. 315-341, 1980.

[2] J. L. Volakis, A. Chatterjee, and L. C. Kempel, *Finite element method for electromagnetics*. New York: IEEE Press, 1998, ch. 2.

[3] J. P. Webb and B. Forghani, "Hierarchical scalar and vector tetrahedra," *Digest of the Fifth Biennial IEEE Conference on Electromagnetic Field Computation*, Aug., 1992.

[4] J. S. Savage and A. F. Peterson, "Higher-order vector finite elements for tetrahedral cells," *IEEE Trans. Microwave Theory Tech.*, vol. 44, pp. 874-879, June 1996.

[5] R. Graglia, D. R. Wilton, and A. F. Petersen. "High order interpolatory vector bases for computational electromagnetics," *IEEE Transactions on Antennas and Propagation*, vol. AP-45, pp. 329-342, March 1997.

[6] L. S. Andersen and J. L. Volakis, "Hierarchical tangential vector finite elements for tetrahedral," *IEEE Microwave and Guided Wave Letters*, vol. 8, pp. 127-129, no. 3, March 1998.

[7] L. S. Andersen and J. L. Volakis, "Development and application of a novel class of hierarchical tangential vector finite elements for electromagnetics," *IEEE Transactions on Antenna and Propagation*, vol. AP-47, pp. 112-120, January 1999.

[8] J. S. Savage. "Comparing high order vector basis functions," *Proc. Of the 14th Annual Review of Progress in Applied Computational Electromagnetics*, Monterey, CA, USA, pp. 524-529, March 1999.

[9] L. S. Andersen and J. L. Volakis, "Condition numbers for various FEM matrices," *Journal of Electromagnetic Waves and Applications*, vol. 13, pp. 1661-1677. December 1999.

[10] Y. Ji and T. H. Hubing, "EMAP5: A 3D hybrid FEM/MoM code," *Appl. Computat. Electromagn. Soc. (ACES) J.*, vol. 15, pp. 1-12, March 2000.

[11] A. F. Petersen, S. L. Ray, and R. Mittra, *Computational Methods for Electromagnetics*, New York: IEEE Press and Oxford University Press, 1997.

[12] J. J. H. Wang, *Generalized Moment Methods in Electromagnetics*, New York: John Wiley & Sons, 1990, ch. 6.

[13] S. M. Rao, D. R. Wilton, and A. W. Glisson, "Electromagnetic scattering by surfaces of arbitrary shape," *IEEE Trans. Antennas and Propagation*, vol. AP-30, no. 3, pp. 409-418, May 1982.

[14] Y. Ji, H. Wang, and T. H. Hubing, "A novel preconditioning technique and comparison of three formulations for the hybrid FEM/MoM method," *Appl. Computat. Electromagn. Soc. (ACES) J.*, vol. 15, pp. 103-114, July 2000.

[15] J. J. Bowman, T. B. A. Senior, P. L. E. Uslenghi, *Electromagnetic and acoustic scattering by simple shapes*, Hemisphere Publishing Corporation, New York: 1987.

[16] H. Wang, C. Guo, T. Hubing, J. Drewniak, T. Van Doren and R. DuBroff, "Application of higher-order FEM elements to the analysis of microstrip structures", *Proc. of the 2002 IEEE International Symposium on Electromagnetic Compatibility*, Minneapolis, MN, August 2002, pp. 1015-1019.

[17] J. –M. Jin, *The Finite Element Method in Electromagnetic,* 2nd edition, New York: John Wiley & Sons, 2002.

[18] D. M. Pozar, *Microwave Engineering*, 2nd edition, New York: John Wiley & Sons, 1998.

APPENDIX A

FEM analysis requires computation of two matrices. These two matrices are,

$$E_{ij} = \int_V \nabla \times \mathbf{w}_i \bullet \nabla \times \mathbf{w}_j \, dV \qquad \text{(A1)}$$

$$F_{ij} = \int_V \mathbf{w}_i \bullet \mathbf{w}_j \, dV \cdot \qquad \text{(A2)}$$

A. CT/LN TVFE

$$\mathbf{w}_{\mathrm{i}} = l_i (L_{i1} \nabla L_{i2} - L_{i2} \nabla L_{i1}) \cdot \qquad \text{(A3)}$$

B. Webb's unnormalized LT/QN TVFE

Edge element

$$\mathbf{w}_i^{\mathrm{e}1} = l_i (L_{i1} \nabla L_{i2} - L_{i2} \nabla L_{i1}) \qquad \text{(A4)}$$

$$\mathbf{w}_i^{\mathrm{e}2} = l_i (L_{i1} \nabla L_{i2} + L_{i2} \nabla L_{i1}) \quad i = 1, \cdots 6 \qquad \text{(A5)}$$

Face element

$$\mathbf{w}_i^{\mathrm{f}1} = L_{i1} L_{i2} \nabla L_{i3} - L_{i1} L_{i3} \nabla L_{i2} \qquad \text{(A6)}$$

$$\mathbf{w}_i^{f2} = L_{i1} L_{i2} \nabla L_{i3} - L_{i2} L_{i3} \nabla L_{i1} \quad i = 1, \cdots 4 \qquad \text{(A7)}$$

B. Webb's normalized LT/QN TVFE

Edge element

$$\mathbf{w}_i^{\mathrm{e}1} = L_{i1} \nabla L_{i2} - L_{i2} \nabla L_{i1} \qquad \text{(A8)}$$

$$\mathbf{w}_i^{\mathrm{e}2} = L_{i1} \nabla L_{i2} + L_{i2} \nabla L_{i1} \quad i = 1, \cdots 6 \qquad \text{(A9)}$$

Face element

$$\mathbf{w}_i^{\mathrm{f}1} = L_{i1} L_{i2} \nabla L_{i3} - L_{i1} L_{i3} \nabla L_{i2} \qquad \text{(A10)}$$

$$\mathbf{w}_i^{f2} = L_{i1} L_{i2} \nabla L_{i3} - L_{i2} L_{i3} \nabla L_{i1} \quad i = 1, \cdots 4 \qquad \text{(A11)}$$

C. Andersen's unnormalized LT/QN TVFE

Edge element

$$\mathbf{w}_i^{\mathrm{e}1} = l_i (L_{i1} \nabla L_{i2} - L_{i2} \nabla L_{i1}) \qquad \text{(A12)}$$

$$\mathbf{w}_i^{\mathrm{e}2} = l_i (L_{i1} - L_{i2})(L_{i1} \nabla L_{i2} - L_{i2} \nabla L_{i1}) \quad i = 1, \cdots 6 \qquad \text{(A13)}$$

Face element

$$\mathbf{w}_i^{\mathrm{f}1} = L_{i1} L_{i2} \nabla L_{i3} - L_{i1} L_{i3} \nabla L_{i2} \qquad \text{(A14)}$$

$$\mathbf{w}_i^{f2} = L_{i1} L_{i2} \nabla L_{i3} - L_{i2} L_{i3} \nabla L_{i1} \quad i = 1, \cdots 4 \qquad \text{(A15)}$$

D. Andersen's normalized LT/QN TVFE

Edge element

$$\mathbf{w}_i^{\mathrm{e}1} = L_{i1} \nabla L_{i2} - L_{i2} \nabla L_{i1} \qquad \text{(A16)}$$

$$\mathbf{w}_i^{\mathrm{e}2} = (L_{i1} - L_{i2})(L_{i1} \nabla L_{i2} - L_{i2} \nabla L_{i1}) \quad i = 1, \cdots 6 \qquad \text{(A17)}$$

Face element

$$\mathbf{w}_i^{\mathrm{f}1} = L_{i1} L_{i2} \nabla L_{i3} - L_{i1} L_{i3} \nabla L_{i2} \qquad \text{(A18)}$$

$$\mathbf{w}_i^{f2} = L_{i1} L_{i2} \nabla L_{i3} - L_{i2} L_{i3} \nabla L_{i1} \quad i = 1, \cdots 4 \qquad \text{(A19)}$$

Hao Wang received his B.S. degree in electrical engineering from Tsinghua University, Beijing, China in 1996, and M.S. and Ph.D. degrees in electrical engineering from the University of Missouri-Rolla, in 2000 and 2002, respectively.

From 1999 to 2002, he was with the Electromagnetic Compatibility Laboratory, University of Missouri-Rolla. He then joined the Advanced Systems Research Laboratory of Micron Technology, Boise, ID, as a signal integrity engineer. His research interests include numerical and experimental analysis of signal integrity and electromagnetic compatibility issues related to memory products, development of PCB design as needed to define next-generation DRAMs.

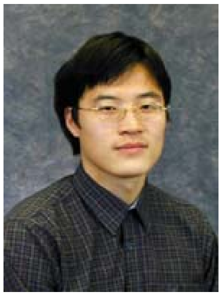

Chunlei Guo was born in China in 1975. He received the B.S. and M.S. degrees in electrical engineering from Tsinghua University, Beijing, China, in 1998 and 2000 respectively.

From 2000, he was with the Electromagnetic Compatibility Laboratory, University of Missouri-Rolla. His research interests include numerical and experimental analysis of signal integrity and electromagnetic compatibility issues related with high-speed digital systems.

Todd Hubing received the BSEE degree from the Massachusetts Institute of Technology, Cambridge, MA in 1980, the MSEE degree from Purdue University, West Lafayette, IN, in 1982, and the Ph.D. degree in electrical engineering from North Carolina State University, Raleigh, NC in 1988.

He is currently a Professor of electrical engineering at the University of Missouri-Rolla (UMR). Prior to joining UMR in 1989, he was an Electromagnetic Compatibility Engineer with IBM, Research Triangle Park, NC. Since joining UMR, the focus of his research has been measuring and modeling sources of electromagnetic interference. He is currently the 2002-2003 President of the IEEE Electromagnetic Compatibility Society.

High Accuracy Calculation of the Magnetic Vector Potential On Surfaces

Malcolm M. Bibby* and Andrew F. Peterson**
*Gullwings, Weston, MA 02493 e-mail: mbibby@gullwings.com
**Georgia Institute of Technology, Atlanta, GA; e-mail: peterson@ee.gatech.edu

Abstract. The calculation of integrals containing the free-space Green's function in electromagnetic problems is difficult to perform with great accuracy. Three approaches to the calculation are investigated. The inadequacy of the singularity-subtraction method is demonstrated. The Duffy transform is shown to provide good results when the test-point is on the surface being investigated. A Maclaurin series expansion with integration prior to summation is shown to be efficient and reliable both on and off the surface under study. Solutions, in both Cartesian and cylindrical coordinate systems, that allow the calculations to be performed to a pre-defined level of accuracy are presented.

Introduction.

The magnetic vector potential, or MVP, is an important quantity that appears in many electromagnetic problems that involve evaluation of electric and/or magnetic fields. For example, it is a component in the definition of the electric field integral equation, EFIE [1, p17]. In this context it may exist in its basic form or it may be subject to differentiation. Its use is at its most basic when used in the solution of Hallen's integral equation for a cylindrical dipole. When used for solving Pocklington's integro-differential equation for the same dipole the second differential of the MVP must be considered. Derivatives of the MVP are also derivatives of the Green's function contained within the definition of the MVP. Because the three-dimensional Green's function contains a singularity, it is preferable to keep the order of differentiation to a minimum, preferably zero. When it cannot be kept to zero, then one of two actions are generally undertaken. Either the derivatives must be transferred to the basis/testing function used in the solution of the particular EFIE under investigation or one of the special formulations that have been developed to accommodate the differentiation [2] [3] must be considered. Even when one examines the evaluation of just the non-differentiated form of the MVP one has certain numerical difficulties to face. These difficulties are addressed in this report. Accurate evaluation of the MVP is gaining importance as the use of higher and higher order basis functions is considered. Also, as we shall see, evaluation of the MVP when the test-point is located a short distance from the test surface is a requirement that, while of interest in many applications, is handled poorly by current techniques.

As the title of this paper suggests, the over-riding issue here is one of solution accuracy. When calculating entries in a matrix, Z, and then solving the corresponding matrix equation, $ZI = V$, Miller [4] has shown that the solution error, $\|dI\|/\|I\|$, is comparable to the product of the error in the terms in the matrix and the condition number of the matrix. For example, if the error of the matrix terms, $\|dZ\|/\|Z\|$, is 10^{-6} and the condition number is 10^{4}, the error of the solution may be no better than 10^{-2} - if nothing else introduces further errors. The resulting accuracy is at the lower limit of usefulness. It can be improved by either reducing the condition number of the

1054-4887 © 2002 ACES

matrix or by reducing the error in the calculation of the matrix entries. This work is about the latter.

After setting out some basic definitions, this report will investigate the difficulties associated with the most widely used approach to the evaluation of the MVP. The second section will examine the use of the Duffy [5] transform which was originally conceived to address issues arising in the evaluation of integrals such as found in the MVP. The third section will show how the MVP can be dealt with in a manner that is not only rigorous but also efficient. This will be followed by a discussion of testing, concluding with a statement of key findings.

Definitions.

The three-dimensional MVP is defined as:

$$I_3 = \iiint \bar{J}(\bar{r}')\frac{e^{-jk\left|\bar{r}-\bar{r}'\right|}}{4\pi\left|\bar{r}-\bar{r}'\right|}dv' \qquad (1)$$

When examining currents on surfaces, this definition reduces to:

$$I_2 = \iint \bar{J}(\bar{r}')\frac{e^{-jk\left|\bar{r}-\bar{r}'\right|}}{4\pi\left|\bar{r}-\bar{r}'\right|}dv' \qquad (2)$$

In the above, $\bar{r}$ denotes the position vector to the test/observation point, and $\bar{r}'$ is the position vector to the surface under study. The scalar component(s), I_s, of the surface current will be represented by polynomials, in u, in the form: $I_s = \sum_{i=0}^{p} a_i u^i$.

Machine precision will be referred to often in this study. By machine precision we will be referring to machine epsilon, ε , which is the gap between 1 and the next larger floating point number [6, p14]. $\varepsilon = 2^{-(p-1)}$ where p is the precision of the machine in bits. Machine precision is:

$$\log_{10}(\varepsilon) = -(p-1)\log_{10}(2) \qquad (3)$$

Results for Compaq Fortran on an Alpha processor are shown in Table I.

Relative error, Rel. error, is defined as:

$$\text{Rel. error} = \frac{\left|f_{approx} - f_{ref}\right|}{\left|f_{ref}\right|}. \qquad (4)$$

f_{ref} will be defined each time that relative error is discussed. When evaluating integrals one frequently compares the result, f_n, obtained in the most recent evaluation, to the result, f_{n-1} obtained in the prior evaluation. This is more accurately defined as convergence rate and:

$$\text{Convergence Rate} = \frac{\left|f_n - f_{n-1}\right|}{\left|f_n\right|} \qquad (5)$$

Singularity Subtraction.

The free-space Green's function is defined as $G(R) = e^{-jkR}/R$ where R is the distance between the source and the observation or test point. The mathematical definition of R is specific to the coordinate system in use and will be elaborated on later. For this section of the report we define $R = \sqrt{u^2 + \delta^2}$ where u is an independent variable and δ will assume various fixed values. $G(R)$ is split into two parts $G(R) = G_r(R) + G_s(R)$, where $G_r(R)$ is the non-singular part and $G_s(R)$ is the singular part [7]. Specifically, we have:

$$G_r(R) = e^{-jkR}/R - 1/R_0 \qquad (6a)$$

$$G_s(R) = 1/R_0 \qquad (6b)$$

$G_s(R)$ is developed from a Taylor series expansion of $G(R)$ and when possible it is evaluated analytically [8]. An example of a solution in the Cartesian coordinate system is given in [1, p420]. In the event an analytical solution is not available, a recent discussion

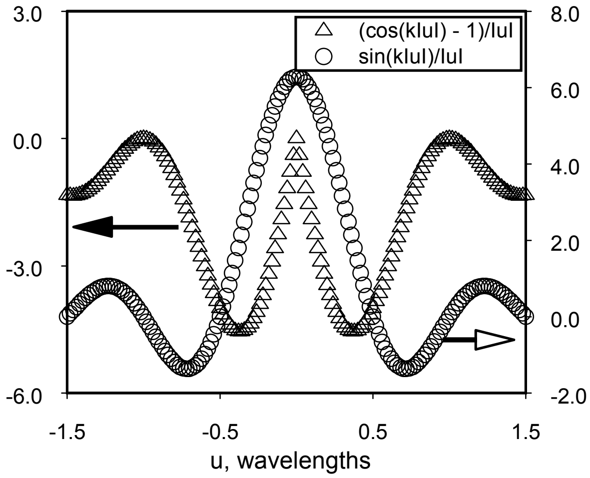

Figure 1. Plots of the real and imaginary parts of G(R) as a function of u.

of numerical methods is available in [9]. The focus in the following is on $G_r(R)$.

For purposes of this immediate analysis we express $G_r(R)$ in terms of its real and imaginary components:

$$G_r(R) = (\cos(kR) - 1)/R - j\sin(kR)/R \qquad (7)$$

These two components, when $R = |u|$ (i.e. $\delta = 0$) are plotted in Figure 1. Both components are finite throughout the range. However, the real component is obviously not 'smooth' at $u = 0.0$.

The results for integrating the real component of $G_r(R)$ with Gauss-Legendre quadrature are plotted in Figure 2a, where d is the same as δ in the text. The reference values were calculated using the series expansion method described later. It is observed that the integration convergence becomes worse as $\delta \to 0$, a finding which is somewhat unexpected, counter-intuitive and disconcerting. A similar observation is implied in Figure 2 in [10].

When evaluating integrals numerically, particularly close to the source, it is important to remember that integration rules generally exhibit an error that is proportional to the derivatives of the function being integrated.

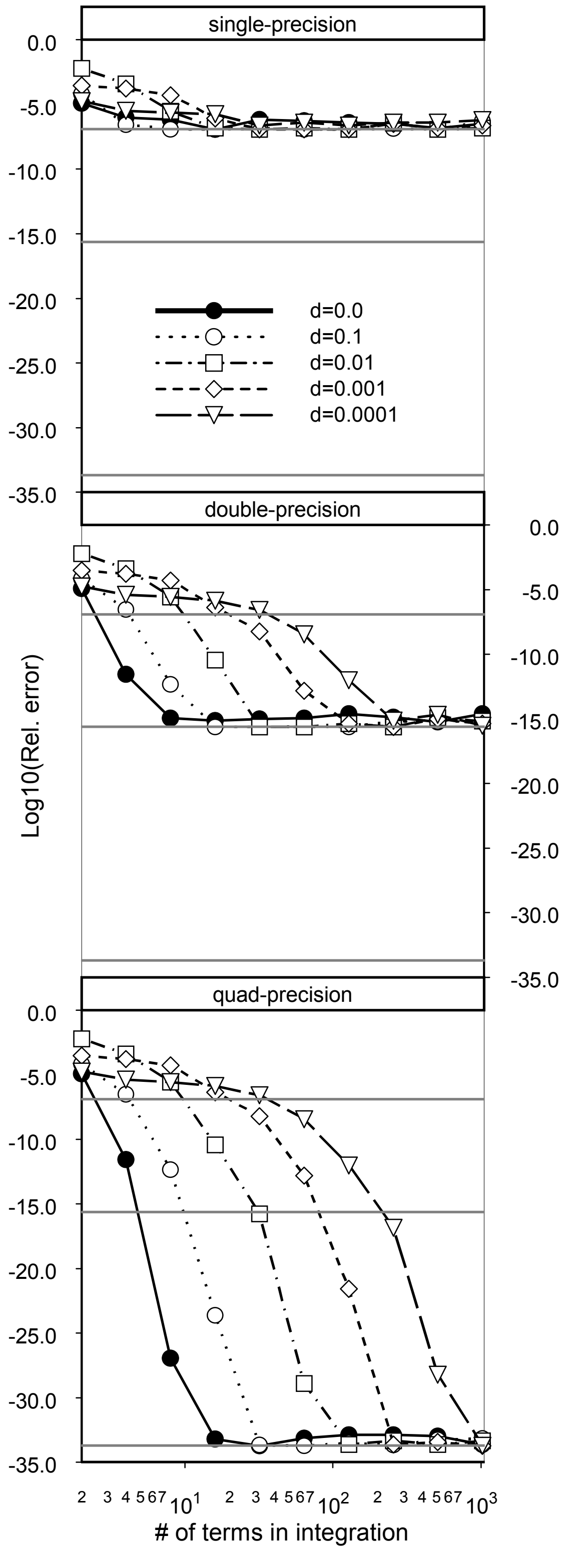

Figure 2a. The effect of d on the relative error in the integration of the real part of the Green's function.

In the case of: $f = (\cos(kR) - 1)/R$ (8a)

then $\dfrac{df}{du} \approx \dfrac{-k^2 u}{2R}$ (8b)

and $\dfrac{d^2 f}{du^2} \approx -\dfrac{k^3 u^2}{3R^2} - \dfrac{k^2 \delta^2}{2R^3}$ (8c)

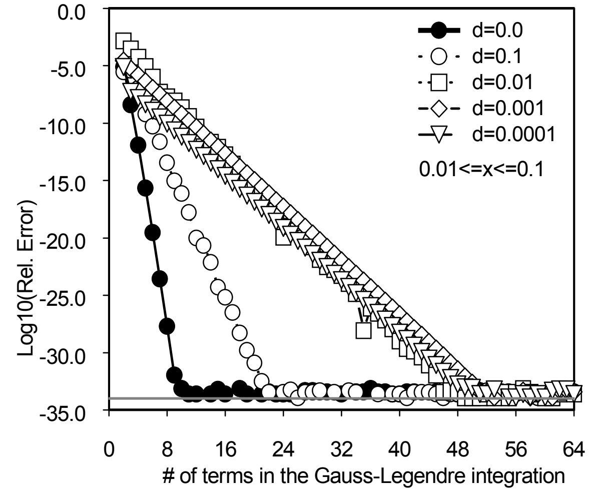

Figure 2b. Effect of n on the integration of (cos(k|R|) - 1)/R when x is not at the origin.

From this last equation we see that as:

$$u \to 0, \; \frac{d^2 f}{du^2} \to -\frac{k^2}{2\delta} \tag{8d}$$

which provides an explanation for the behavior of the curves in Figure 2a. To illustrate that it is, in fact, the presence of the discontinuity at $u = 0$ that creates the problems, the lower limit of integration was moved from $u = 0$ to $u = 0.01$. The results of this change are shown in Figure 2b and clearly demonstrate that the problem has been significantly mitigated.

For the special case of $\delta = 0$, we find that although there is a jump in the values of $\dfrac{df}{du}, \dfrac{d^2 f}{du^2}$ and higher derivatives when u moves from 0_- to 0_+ they are finite in that region nevertheless, and so the integration rules hold for this special case.

For double/triple integrals δ is introduced into the inner integral by the outer integral defining the MVP and thus δ may become arbitrarily

$$I_{cart} = \int_0^{x_1}\int_0^{y_1} \frac{e^{-jkr}}{r} dx dy = \int_0^{x_1} dx \int_0^{Kx} \frac{e^{-jkr}}{r} dy + \int_0^{y_1} dy \int_0^{y/K} \frac{e^{-jkr}}{r} dx \text{ where } r = \sqrt{x^2 + y^2 + z_0^2} \text{ and } K = y_1/x_1$$

Substituting $y = uKx$ and $x = vy/K$ in the inner integrals, we arrive at:

$$I_{cart} = \int_0^{x_1} dx \int_0^1 \frac{e^{-jkr} du}{\sqrt{u^2 + (1/K)^2 + (z_0/Kx)^2}} + \int_0^{y_1} dy \int_0^1 \frac{e^{-jkr} dv}{\sqrt{v^2 + K^2 + (z_0 K/y)^2}} \tag{9}$$

$$I_{cyl} = \int_0^{\pi/2}\int_0^{z_1} z^p \frac{e^{-jkr}}{r} d\theta\, dz = \int_0^{\pi/2} d\theta \int_0^{\theta/K} z^p \frac{e^{-jkr}}{r} dz + \int_0^{z_1} z^p dz \int_0^{Kz} \frac{e^{-jkr}}{r} d\theta$$

where $r = \sqrt{z^2 + \Delta\rho_0^2 + 4a(a + \Delta\rho_0)\sin^2\theta}$, $\mathrm{K} = \dfrac{\pi}{2\mathrm{z}_1}$

Substituting $z = u\theta/K$ and $\theta = vKz$ in the inner integrals we obtain:

$$I_{cyl} = \int_0^{\pi/2} d\theta \int_0^1 \frac{(u\theta/K)^p e^{-jkr} du}{\sqrt{u^2 + 4a(a + \Delta\rho_0)(K\sin\theta/\theta)^2 + (K\Delta\rho_0/\theta)^2}} +$$

$$\int_0^{z_1} z^p dz \int_0^1 \frac{e^{-jkr} dv}{\sqrt{(1/K)^2 + 4a(a + \Delta\rho_0)(\sin(vKz)/Kz)^2 + (\Delta\rho_0/Kz)^2}} \tag{10}$$

Equation Set 1. The MVP equation, expressed in two different coordinate systems, transformed, by the Duffy method, to remove the singularity at the origin.

small, but non-zero, leading to these problems. Consequently, when evaluating the real part of $G_r(R)$, it would appear that all quadrature rules, when applied directly, are doomed to fail as even the simple trapezoid rule requires that the second derivative of the integrand be well behaved. With this conclusion it is advisable to seek alternative methods.

Singularity Removal by Transformation.

In 1982, Duffy [5] proposed a method that, through a change of variable, causes the removal of the singularity in the integrand of two and three dimensional integrals. His method is presented here first with a constant current, for simplicity, in the Cartesian coordinate system. Currents of polynomial form u^p, are included with the discussion of the cylindrical coordinate system.

The formalism for each of the two coordinate systems is shown in Equation Set 1. It allows for the test/observer point to be offset from the surface – by amount z_0 in the Cartesian system and $\Delta\rho_0$ in the cylindrical system.

When the offset is zero, the formulae in the Cartesian system clearly show that the singularity has been removed. Furthermore, in this case, the denominator in the integrand is not dependant on the variable associated with the outer loop other than through the value of K, which is fixed. Consequently, the derivatives of the integrand are all well behaved and one can expect that quadrature integration will work well, and indeed it does.

Precision	ε	Outer Integral	Inner Integral
Single	1.2E-07	7	7
Double	2.3D-16	7	13
Quad	2.0D-34	13	37

Table I. The number of terms required in one of the double integrals for a square domain using the Duffy transform.

For example, using Gauss-Legendre for both the inner and outer integrals, the numbers of terms necessary for computing the double integral, to a precision of 2ε, on a flat surface are shown in Table 1. The dimensions of the cell were $0.0 \le x \le 0.1,\ 0.0 \le y \le 0.1$. Because of symmetry in this example, the numbers of terms, required in the two double integrals, are the same. All the integrals terminate when the convergence rate falls below the precision level, 2ε.

When examining a cylindrical case we look at a cell width of 0.1 wavelengths on a cylinder of radius 0.007 wavelengths. In addition, polynomial representations of the current, to the degree p, are incorporated. Again, the examination takes place on the surface, so that $\Delta\rho_0 = 0$. For this case we track the number of terms in the outer(out) and inner(in) integrals for the two transformed double integrals. We identify these as u-out, u-in, v-out and v-in. The results, calculated in double precision to a precision level of 2ε, are shown in Table II. They indicate no dependence between the degree, p, and the number of terms.

p	u-out	u-in	v-out	v-in	Total
0	11	36	8	10	476
1	9	38	9	10	432
2	10	36	10	9	450
3	13	34	9	10	532
4	12	29	10	9	438
5	11	29	10	9	409

Table II. The number of terms required in each of the integrals for the cylindrical surface using the Duffy transform.

The good performance of the Duffy transform when the offset is zero does not follow through when the offset is some finite value. This is revealed when the data of Table III is examined. This table shows the total number of iterations needed by the integrals as a function of the value of the offset, $\Delta\rho_0$. The dimensions on a cylindrical surface are the same as used in Table II. A value of $p = 0$ was used.

Offset	**Duffy**	**G-L**
0.0	476	N/A
0.0001	12280	4356
0.001	4504	1860
0.01	1370	952
0.1	311	143

Table III. The effect of the offset value on the number of integration terms for the cylindrical surface using the Duffy transform and Gauss-Legendre applied directly to the double integral.

For comparative purposes Table III also shows the results when the MVP is integrated directly. This is possible when the offset is finite. We conclude that for test/observation points off the surface, the Duffy transform is unacceptably inefficient. Nevertheless, when the test/observation point is on the surface the transform offers a method that provides rigorous convergence in the integrals associated with the MVP.

A Series Expansion for $G(R)$.

The Maclaurin expansion for the real and imaginary components of the Green's function are:

$$\cos(kR)/R = 1/R - k^2R/2! + k^4R^3/4!.. \quad (11a)$$

$$\sin(kR)/R = k - k^3R^2/3! + k^5R^4/5!... \quad (11b)$$

The method proposed integrates the expansions in (11a) and (11b), term by term, until the ratio of the last term evaluated to the largest term evaluated is less than machine-precision. In this way it is possible to develop analytical terms for the inner integral. The terms for the expansion in (11a) are shown in the series (12a)–(12d) and the terms for the expansion of (11b) are shown in (13a)–(13d). Each of these integrals is exact for a given value of δ. The formulae are shown with a lower limit of $u = 0.0$, but this is done for convenience only.

The Green's function is rarely evaluated on a stand-alone basis; rather it is evaluated in conjunctions with a representation of the current on the surface being studied. We will adopt the polynomial summation defined earlier. The integrals of interest are:

$$G_{\mathrm{Re}} = \int_{u_1}^{u_2} u^p \frac{\cos(kR)}{R} du \quad (16a)$$

$$G_{\mathrm{Im}} = \int_{u_1}^{u_2} u^p \frac{\sin(kR)}{R} du \quad (16b)$$

The case of $p = 0$ has already been presented in equations (12) and (13). The case for $p = 1$ is shown in equation (14) and for $p \geq 2$ the relevant equation is (15). This last equation is applicable to the computations of both G_{Re} and G_{Im}. Thus, once the terms for $p = 0$ and $p = 1$ have been evaluated, the evaluations for higher values of p are straightforward.

The Series Expansion, Integration and Summation, SEIS, process described above was tested in several ways. The first test revisits the calculations performed for use in Figure 2a. We examine the effect of varying δ on the number of terms required to achieve convergence in the summations of the series. The results of such calculations on G_{Re} for $p = 0$, shown in Figure 3, demonstrate that the value of δ has little impact in this context and thus we conclude that a major goal of the present work has been achieved.

The second series of tests performed involved the inclusion of basis functions as discussed earlier. Shown below, in Equation Set III, are analytical expressions for some inner integrals. Using these expressions, the accuracy of the present method can be examined for the inner integral when p is odd. As a practical note, the calculation of these inner integrals (17) to high accuracy required the use of extremely high precision software. That used here was developed by Bailey [11].

$$\int_0^b \frac{du}{R} = \log(b + \sqrt{b^2 + \delta^2}) - \log(|\delta|) \tag{12a}$$

$$\int_0^b R\,du = \frac{1}{2}\left[bR_b + \delta^2 \int_0^b \frac{du}{R}\right] \text{ where } R_b = \sqrt{b^2 + \delta^2} \tag{12b}$$

$$\int_0^b R^3 du = \frac{1}{4}\left[bR_b^3 + 3\delta^2 \int_0^b R\,du\right] \tag{12c}$$

$$\vdots$$

$$\int_0^b R^{2m-1} du = \frac{1}{2m}\left[bR_b^{2m-1} + (2m-1)\delta^2 \int_0^b R^{2m-3} du\right] \text{ where } m \geq 1 \tag{12d}$$

$$\int_0^b du = b \tag{13a}$$

$$\int_0^b R^2 du = \int_0^b (u^2 + \delta^2) du = \frac{b^3}{3} + \delta^2 b \tag{13b}$$

$$\int_0^b R^4 du = \int_0^b (u^2 + \delta^2)^2 du = \frac{b^5}{5} + 2\delta^2 \frac{b^3}{3} + b \tag{13c}$$

$$\vdots$$

$$\int_0^b R^{2n} du = \int_0^b (u^2 + \delta^2)^n du = \frac{b^{2n+1}}{2n+1} + \frac{n\delta^2 b^{2n-1}}{2(2n-1)} \text{........} + \delta^{2n} b \tag{13d}$$

When $p = 1$

$$\int_{u_1}^{u_2} uR^{m-1} du = \left.\frac{R^{m+1}}{m+1}\right|_{u=u_1}^{u=u_2} \text{ where } 0 \leq m \tag{14}$$

When $p \geq 2$, a recurrence formula can be derived which takes the form:

$$\int_{u_1}^{u_2} u^p R^m du = \frac{1}{p+m+1}\left[u^{p-1}R^{m+2}\Big|_{u=u_1}^{u=u_2} - (p-1)\delta^2 \int_{u_1}^{u_2} u^{p-2} R^m du\right] \text{ where } -1 \leq m \tag{15}$$

Equation Set II. The basic equations for the term-by-term integration of a Maclaurin series expansion of the Green's function and its product with a polynomial.

The results for G_{Re} appear in Figure 4. Results for G_{Im} and G_{Re} are not visually distinguishable and hence only the results for G_{Re} are shown. The plots clearly show that, at most, 5, 8, or 14 terms, for single, double or quad precision respectively, are needed in the series expansion for this integration range. The plots also clearly show that the relative error is not dependant on p, the exponent in the basis function used to represent the current. The results presented in Figure 5, for the even values of p, are referenced with respect to their own machine precision limited values. Their behavior is similar to the results for odd values of p, which are referenced to analytical values.

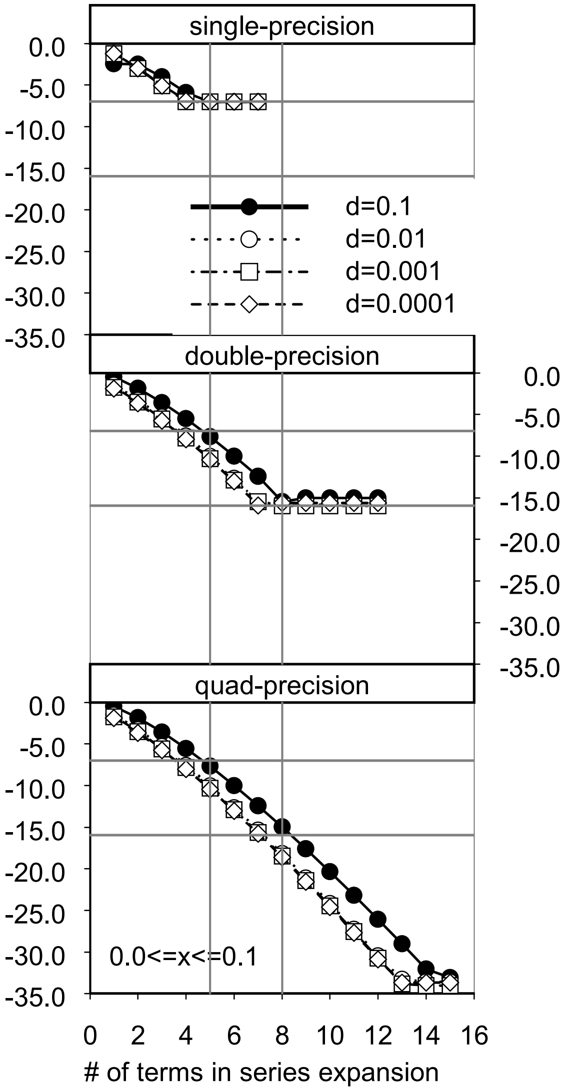

Figure 3. Convergence curves for the real component of the Green's function for different values of d.

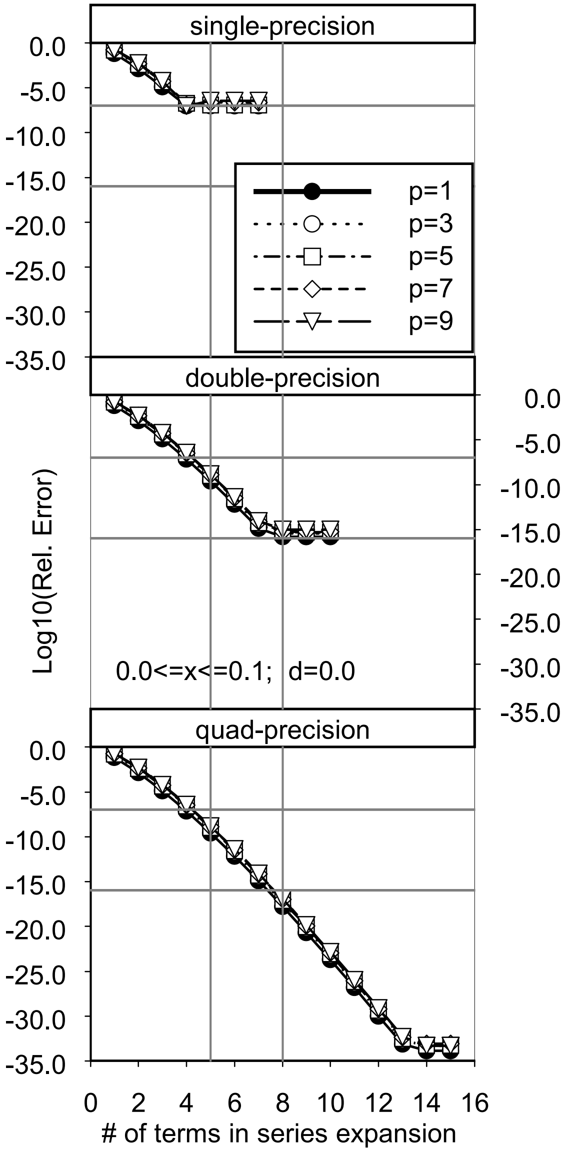

Fig4. Convergence curves for the integrals with odd powers of p.

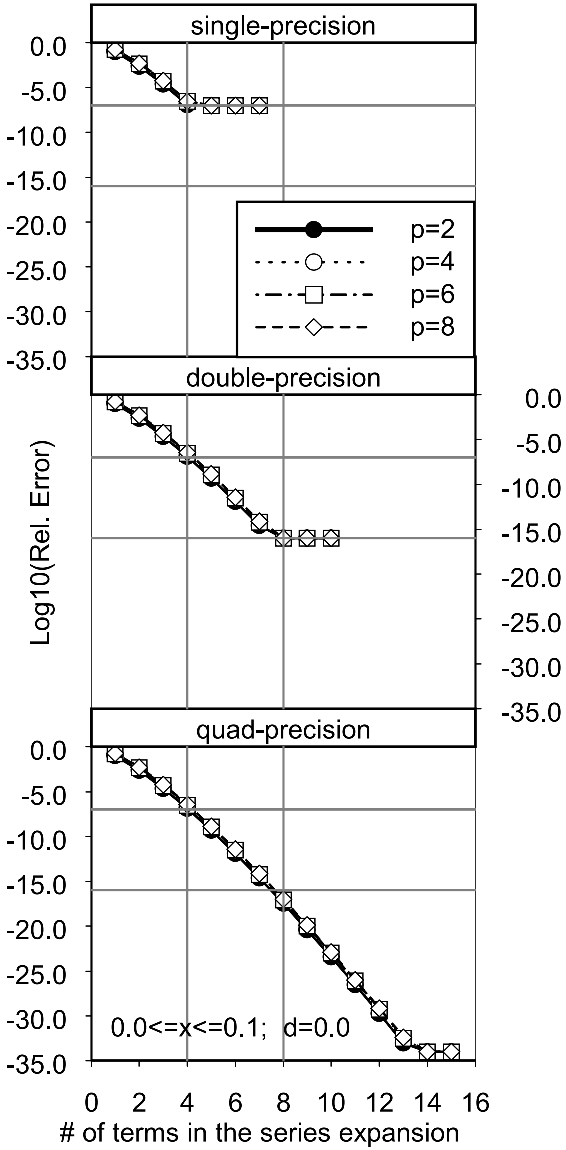

Fig5. Convergence curves for integrals with even values of p.

Consider $I_p = \int_{u_1}^{u_2} \frac{u^p e^{-jkR}}{R} du$ where $R = \sqrt{u^2 + \delta^2}$. With the substitution $dR = \frac{udu}{R}$ we get $I_p = \int u^{p-1} e^{-jkR} dR$. When p is odd, this integral can be solved analytically. For example:

$$p = 1;\ I_p = \left.\frac{je^{-jkR}}{k}\right|_{u_1}^{u_2} \tag{17a}$$

$$p = 3;\ I_p = \left[e^{-jkR}\left[u^2\left(\frac{j}{k}\right) - 2R\left(\frac{j}{k}\right)^2 + 2\left(\frac{j}{k}\right)^3\right]\right]_{u_1}^{u_2} \tag{17b}$$

$$p = 5;\ I_p = \left[\frac{je^{-jkR}}{k}\left[u^4 - 4\left[u^2R + (\delta^2 - 3R^2)\left(\frac{j}{k}\right) + 6R\left(\frac{j}{k}\right)^2 - 6\left(\frac{j}{k}\right)^3\right]\right]\right]_{u_1}^{u_2} \tag{17c}$$

Equation Set III. Examples of analytical solutions for the integral for odd p.

Application to the Magnetic Vector Potential.

The application of the above procedure to double integrals is straightforward. The inner integral is computed as above and then a quadrature integration formula is applied to the outer integral.

Cartesian coordinates. A double integral of interest is given by:

$$I_{Cart} = \int_{y}^{y_2} dy \int_{x_1}^{x_2} (x - x_0)^p \frac{e^{-jkR}}{R} dx$$

where $R = \sqrt{(x - x_0)^2 + (y - y_0)^2 + z_0^2}$.

The surface is in the x-y plane and the test point is at (x_0, y_0, z_0). In terms of the inner integral we replace $(x - x_0)$ by u, $((y - y_0)^2 + z_0^2)$ by δ^2 and adjust the integration limits appropriately.

Cylindrical coordinates. Here, the double integral is given by:

$$I_{cyl} = \frac{1}{2\pi}\int_{0}^{2\pi} d\phi \int_{z_1}^{z_2} (z - z_0)^p \frac{e^{-jkR}}{R} dz$$ where $R = \sqrt{(z - z_0)^2 + (\Delta\rho_0)^2 + 4a(a + \Delta\rho_0)\sin^2\phi}$

The surface is that of a cylinder of radius a, and with $\Delta\rho_0 \geq -a$ the test point is at $(a + \Delta\rho_0, 0, z_0)$. In this instance $\delta^2 = (\Delta\rho_0)^2 + 4a(a + \Delta\rho_0)\sin^2\phi$ and $u = (z - z_0)$ and again the limits of integration are appropriately adjusted.

The results for the calculation of the MVP for a section of a cylindrical dipole with values of $a = 0.007\lambda$ and $0.0 \leq z \leq 0.1$ are shown in Figures 6a and 6b. Two quadrature methods were investigated – the Gauss-Legendre method and the Linlog method [12]. The reason for choosing the latter method is that the series containing even p always contains log terms in its real component. Linlog was designed specifically to integrate functions that contain polynomials and logarithmic terms.

Both sets of calculations were performed in quad precision. The reference values were calculated using 42 terms with the respective quadrature methods. The superiority of the Linlog approach, when applied for even powers of p, is clearly visible. The relative error is seen to reach a level of approximately –21.4 and then remains constant. The nodes and weights, as originally reported, are only known to 20 digits, hence the observation is hardly surprising. This, then, is the bound on

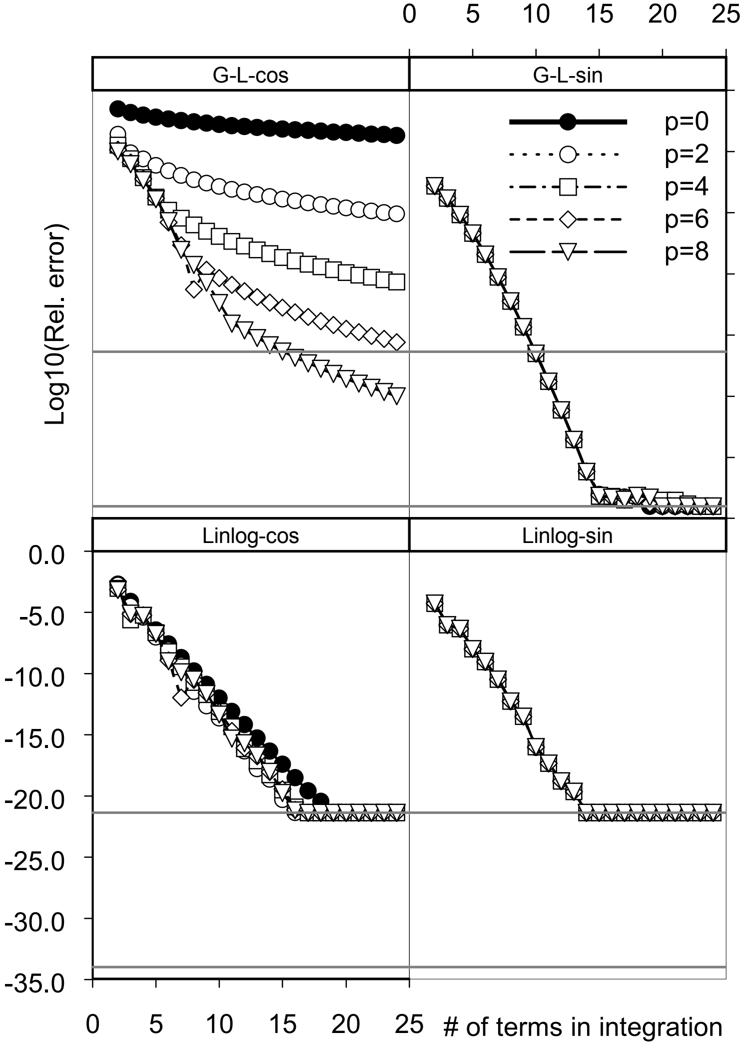

Figure 6a. Performance of two integration methods on the real and imaginary parts of the magnetic vector potential on the surface of a cylindrical dipole, for even values of p.

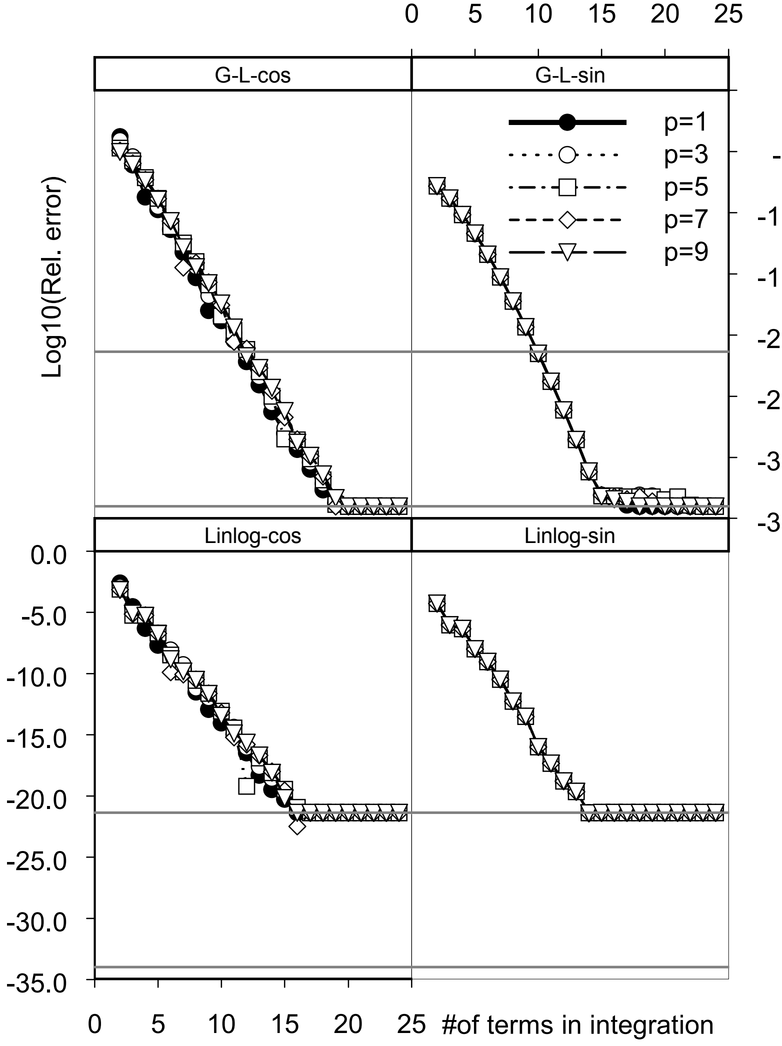

Figure 6b. Performance of two integration methods on the real and imaginary parts of the magnetic vector potential on the surface of a cylindrical dipole, for odd values of p.

the accuracy to which this particular MVP can be calculated using today's tools.

It remains to examine the effect of the offset value as was done for the Duffy transform and reported in Table III. Again the work is done in double precision and is for $p = 0$. The ensuing results are shown in Table IV. Compared with the results in Table III, it is clear that the value of the offset has little effect on the number of terms needed to achieve a relative accuracy equal to the machine precision.

Offset	Outer	Series	Total
0.0	14	8	112
0.1	17	9	153
0.01	23	7	161
0.001	24	8	192
0.0001	24	7	168

Table IV. The effect of the offset values on the number of integration terms for the cylindrical surface using the term-by-term integration of a Maclaurin series.

Comparison Between Duffy and SEIS.

The efficiency of the calculation of the MVP by the two methods – the Duffy transform and the SEIS method – was investigated for the cylindrical case already discussed. In the case of the Duffy transform the number of function evaluations of both inner integrals was counted. In the case of the SEIS the count was the product of the number of nodes in the outer integral and the number of terms in the series expansion. The results are shown in Figure 7. The reference line is located at πa. It appears that both methods are most efficient when the aspect ratio of the cell under consideration is approximately 1:1. The Duffy transform is particularly susceptible to this phenomenon. In the case of the SEIS approach, at the high end of the z range, the number increases as the value of z increases – due to the need for more terms in the series expansion. At the low end of the range, the number of terms needed in the series expansion falls off – but the number of nodes needed in the Linlog integration increases.

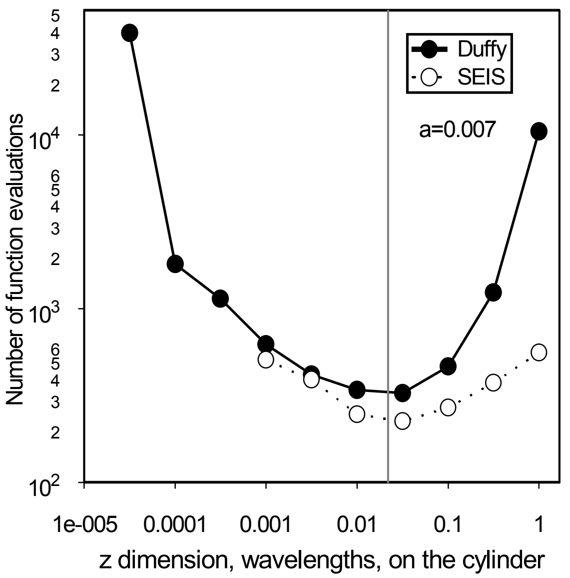

Figure 7. The effect of the z dimension on the number of 'evaluations' needed to compute the MVP using the Duffy transform and the SEIS methods.

In this example, the number of integration nodes needed for z=0.001 was 39.

Key Findings

1) It was shown that conventional numerical methods give misleading results when integrating the Green's function. Consider the results of Figure 2a. When $\delta = 0.0001$ the relative error changes very little as the number of integration terms is increased until very large numbers of terms are employed. The slow improvement in the error curve would normally be interpreted as convergence – leading to an inaccurate evaluation. It was shown that this behavior is a direct consequence of the derivatives in the neighborhood of $u = 0$.

2) The results presented in Figures 2a and 6 emphatically illustrate the poor performance of Gauss-Legendre methods for evaluating the real component of any of the integrals studied. This finding is applicable to all quadrature methods that are applied directly to this class of problem.

3) The Duffy transform provides a reliable method for computing the MVP when the test point is on the surface. As implemented here, it is not suitable for use when the test point is off the surface. It has the advantage that the integrals can be evaluated using standard integration techniques such as Gauss-Legendre.

4) The use of a Maclaurin expansion of the Green's function, followed by term by term integration and careful summation provides a stable means for calculating both the real and imaginary components of the function. The method is efficient and can be used both on and off the surface being examined.

5) Analytical solutions for the integral of the Green's function and its product with polynomial representations, of odd degree, of the surface current have been presented. These solutions provide a method for evaluating both the convergence and the accuracy of the series-expansion-integration-summation approach.

6) The analytical results presented for current representations of odd degree would appear to offer an accurate and efficient approach to the evaluation of those integrals. However, it was found that rounding errors seriously degraded the accuracy of such calculations when the range of integration was small and such an approach should be avoided unless high precision software is employed.

7) The algorithm used for the outer integral, when using the series expansion-integration-summation approach must recognize the presence of the logarithmic terms in the series expansion when p is even. This means using the Linlog method [12] for this particular integration.

Final Remarks

The calculation of integrals associated with the magnetic vector potential has been examined in depth. The integration of the Green's function should not be attempted with quadrature methods, unless some suitable transformation to remove the singularity has been undertaken. An example of the latter is the transform due to Duffy, and this is quite suitable when the test point is on the surface. For all-round performance, it is proposed that the inner integral, that includes the Green's function, be evaluated by means of the integration of each term of a Maclaurin expansion. The outer integral can then be evaluated using the Linlog rule. In all cases, the integration can be taken to the precision of the machine/compiler (single, double or extended/quad), except that the Linlog nodes/weights currently limit the relative error to approximately 20 digits. The integration of the Maclaurin series prior to summation provides a method that is efficient and accurate.

References.

[1] A. F. Peterson, S. L. Ray, R. Mittra, *Computational Methods for Electromagnetics*, IEEE Press, 1998.

[2] D. B. Miron, "The Singular Integral Problem in Surfaces", *IEEE Trans. Ant. & Prop.*, Vol. AP-31, No. 3, pp. 507-509, May 1983.

[3] A. D. Yaghijan, "Electric Dyadic Green's Functions in the Source Region", *Proc. IEEE*, Vol. 68, No. 2, pp. 248-263, Feb. 1980.

[4] E. K. Miller, "A Computational Study of the Effect of Matrix Size and Type, Condition Number, Coefficient Accuracy and Computation Precision on Matrix-Solution Accuracy", *Intl. Symp. On Ant. & Prop. Digest, Newport Beach, CA*, pp. 1020-1023, June 1995.

[5] M. G. Duffy, "Quadrature Over a Pyramid or Cube of Integrands with a Singularity at a Vertex", *SIAM J. Numer. Anal.*, Vol. 19, No. 6, pp. 1260-1262, Dec. 1982.

[6] M. L. Overton, *Numerical Computing with IEEE Floating Point Arithmetic*, SIAM, 2001.

[7] D. R. Wilton, C. M. Butler, "Effective Methods for Solving Integral and Integro-

Differential Equations", *Electromagnetics*, Vol. 1, pp. 289-308, 1981.

[8] J. M. Song, W. C. Chew, "Moment Method Solutions Using Parametric Geometry", *J. of Electromagnetic Waves and Appl*., Vol. 9, pp. 71-83, 1995.

[9] A. Herschlein, J. v. Hagen, W. Wiesbeck, "Methods for the Evaluation of Regular, Weakly Singular and Strongly Singular Surface Reaction Integrals Arising in Method of Moments", *ACES Journal,* Vol. 15, No. 1, pp. 63-73, March 2002.

[10] M. Gimersky, S. Amari, J. Bornemann, "Numerical Evaluation of the Two-Dimensional Generalized Exponential Integral", *IEEE Trans. Ant. & Prop.,* Vol. AP-44, No. 10, pp. 1422-1425, 1996.

[11] D. H. Bailey, "A Portable High Performance Multi-precision Package", *RNR Technical Report RNR-90-022*, May 18, 1993. See also www.nersc.gov/~dhbailey/mpdist/.

[12] J. H. Ma, V. Rohklin, S. Wandzura, "Generalized Gaussian Quadrature Rules for Systems of Arbitrary Functions", *SIAM J. Numer. Anal.,* Vol. 33, pp. 971-996, June 1996.

Addendum: Procedural Considerations.

In order to assure the best possible accuracy when evaluating series such as those in equations (12) - (15), several "good practice" issues need to be followed.

1) Terms that are to be added need to be stored separately from those that are to be subtracted. Thus the values associated with the upper limit in an integration formula must be separated from those associated with the lower limit of integration. A similar separation should be maintained when implementing the Maclaurin series, noting that this involves the additional complication of a series with alternating signs.

2) When evaluating the terms associated with the real part of the overall integral, negative values may occur due to the presence of the log term. These should be identified and stored appropriately.

3) Terms should be added by starting with the smallest and proceeding to the largest. To this end, the two sets of terms need to be sorted in ascending order prior to summation.

4) There is considerable repetition in the components from one term to the next. This observation can be exploited to create a fast, resource-conserving algorithm.

Malcolm M. Bibby received the B.Eng. and Ph.D. degrees in Electrical Engineering from the University of Liverpool, England in 1962 and 1965 respectively. He has been interested in the numerical aspects associated with antenna design for the last twenty years.

Andrew F. Peterson received the B.S., M.S., and Ph.D. degrees in Electrical Engineering from the University of Illinois, Urbana-Champaign in 1982, 1983, and 1986 respectively. Since 1989, he has been a member of the faculty of the School of Electrical and Computer Engineering at the Georgia Institute of Technology, where he is now Professor and Associate Chair for Faculty Development. Within ACES, he served for six years (1991-1997) as a member of the Board of Directors, and has been the Finance Committee Chair and the Publications Committee Chair.

Efficient GRE Techniques for the Scattering of Three-Dimensional Arbitrarily Shaped Deep Cavities

Shumin Wang
Department of Electrical Engineering, The Ohio State University,
1320 Kinnear Road, Columbus, OH 43212, U.S.A
Email: james.wang@ieee.org

Mingzhi Li, Changqing Wang and Xili Zhu
Department of Electronics, Beijing University, Beijing, 100871, P. R. China

ABSTRACT: An efficient implementation of the Generalized Ray Expansion (GRE) method for computing the scattering of three-dimensional (3-D) arbitrarily shaped deep cavities is studied in this paper. Efficiency is being sought from two aspects: ray racing in discrete cavities and reflection from individual patches. An improved algorithm for detecting intersections between a ray and triangular patches has been proposed, which is about 2.83 times faster than the traditional algorithm. Also, sectional algorithm and Wavefront Advancing and Candidate Narrowing (WACN) algorithm for tracing rays inside 3-D cavities are proposed to boost efficiency. As to reflection from individual patches, different local cavity reconstruction methods are being tested and interpolative triangular patches are found to be an efficient choice. Finally, several numerical examples further demonstrate the versatility and validity of our approach.

I. INTRODUCTION

Electromagnetic scattering from arbitrarily shaped deep cavities is of great importance in radar cross section (RCS) estimation of modern jet aircraft [1]-[8]. Because these targets are usually composed of two different parts, i.e., an electrically large, smooth varying air duct and a relatively short, geometrically complex termination, methods suitable for one part generally become unsuitable or even fail for the other part. Due to this discrepancy, hybrid methods are often used instead to solve for different parts [8]. In this article, we shall focus on efficient computation of the electrically large, smooth varying air duct. The methods involved generally include differential equation-based methods [7], integral equation-based methods, waveguide modal analysis and high frequency asymptotic methods [3]. Differential equation- and integral equation-based methods are accurate while much less efficient for deep cavity problems due to the prohibitive amount of memory and CPU requirements. Furthermore, differential equation-based methods suffer from numerical dispersion error for electrically large problems and their applications to deep cavity scattering are limited. Waveguide modal analysis also provides accurate results [3], [4], but the exact waveguide eigenmodes have only been found for simple cross sections. These methods are most often used to give reference solutions.

Because of the smooth varying property of the air duct required by aerodynamics, ray and beam techniques are usually used for high frequency asymptotic methods. The early version was the Shooting and Bouncing Ray (SBR) method which utilizes Geometric Optics (GO) for ray tracing and Aperture Integration (AI) or Reciprocal Integral (RI) for far field computations [1]-[4], [6]. The major problem with the SBR method is that it does not consider higher order effects -especially the field diffracted into the cavity by the rim of the open end. Thus it generally provides an envelope but not details of the scattering pattern. Gaussian Beam (GB) is another approach which instead traces Gaussian beams [3], [5]. Since the Gaussian beam is caustic free by its nature and because it considers fields diffracted into the cavity from the open end, it has much better accuracy than the SBR method. But the beam distortion after a few reflections generally prevents this method from deep cavity problems. The GRE method could be thought of as a combination of SBR and GB methods in some sense [3]. Based on the sub-aperture expansion techniques of the GB method, the GRE method traces GO rays instead of Gaussian beams to improve the beam distortion problem. Since the GRE method includes the interior diffraction by the edge of the open end, it is also more accurate than the SBR method.

The usage of the GRE method is limited by the necessity of tracing massive amounts of rays. This is in turn related to the modeling of a cavity. For simple geometry, analytical functions could be used thus ray tracing is obviously not a problem. For realistic large and arbitrarily shaped cavities, modeling a cavity with ordered 3-D discrete points, which could either be the results of physical measurements or generated by CAD software, is of great versatility and generality.

When applying GRE methods to such realistic 3-D *discrete* cavities, two essential issues need to be

1054-4887 © 2003 ACES

considered. The fist issue is fast ray tracing algorithms in 3-D *discrete* cavities. This topic is rarely documented because most 3-D ray tracing algorithms are designed for 3-D bodies. We shall solve this problem from two aspects: fastening the intersection test of a ray and a triangular patch and reducing the total number of such test needed. An improved intersection test algorithm is proposed for the first aspect and two other algorithms, a sectional algorithm for general cavities and a WACN algorithm for convex cavities, are proposed for the second aspect. The second issue is local cavity reconstruction. There are quite a few choices ranging from simple triangular patches to complex Hermitian bicubic patches. We shall study the accuracy of using different reconstruction methods for reflection computation. We found that an interpolative triangular patch, which is simple to implement and highly accurate, was the best choice.

This article is organized as follows: Section II briefly introduces the GRE method. Section III discusses the efficiency issues. Section IV provides numerical examples. Finally, some conclusions are drawn in Section V.

II. GRE METHOD

In the GRE method, the open end of the cavity is divided into multiple sub-apertures. The electric field radiated by the n-*th* sub-aperture is determined by far zone Kirchhoff approximation with the cavity wall absent. Cone-shaped angular grids of ray-tube are launched from the center of each sub-aperture to represent the spherical wave entering into the cavity. By assuming a local plane wave at the open end and using Physical Optics (PO) to obtain the equivalent electric and magnetic currents, the electric field of the p-*th* ray-tube of the n-*th* sub-aperture is expressed as

$$\begin{aligned}\vec{E}_n\left(\vec{r}_n^{\,p}\right) &= -\frac{jk}{4\pi}\frac{e^{-jkr_n^p}}{r_n^p}\{\iint_{S_n} \hat{r}_n^p \times\left[\hat{s}_n' \times \vec{E}_i\left(\vec{r}_n'\right)\right] e^{jk\vec{r}_n'\cdot\vec{r}_n^p}\, dS' \\ &\quad - Z_0 \cdot \hat{r}_n^p \times \iint_{S_n} \hat{r}_n^p \times\left[s_n' \times \vec{H}_i\left(\vec{r}_n'\right)\right] e^{jk\vec{r}_n'\cdot\vec{r}_n^p}\, dS'\} \\ &= \frac{e^{-jkr_n^p}}{r_n^p}\vec{F}_n(\hat{r}_n^p, \vec{E}_i)\end{aligned} \tag{1}$$

where k is the wave number, $\vec{r}_n^{\,p} = r_n^p \hat{r}_n^p$ and $\hat{r}_n^p$ is the unit vector representing the direction of the p-*th* ray-tube, $\vec{r}_n'$ represents the location of an equivalent source on the sub-aperture, $\hat{s}_n'$ is the unit surface normal pointing inwards the cavity, and $\vec{E}(\vec{r})$ and $\vec{H}(\vec{r})$ represent the incident electric and magnetic field respectively. The integration is over the sub-aperture. Note that the far zone radiating field is decomposed into the product of a spherical wave and a vector far zone pattern. Portions of the spherical wave could be individually traced as GO rays. Incident field information is only contained in the vector far zone pattern $\vec{F}_n(\hat{r}_n^p, \vec{E}_i)$. Ray tracing and the calculation of $\vec{F}_n(\hat{r}_n^p, \vec{E}_i)$ are independent. Thus the GRE method could generate the result at any incident angle in the effective angular range ($10^\circ - 15^\circ$ narrower than the largest ray tracing angle) with just one ray tracing. Also, ray tracing is time consuming rather than memory consuming. The independency of each ray tracing makes it very suitable to utilize distributed computer systems because there are virtually no communications between different processes and load balancing is easy to handle.

The total transmitted field could be written as

$$\vec{E}\ (\vec{r}) = \sum_{n=1}^{N}\sum_{p=1}^{P}\vec{E}_n^{\,p}(\vec{r}_n^{\,p}) \tag{2}$$

To evaluate $\vec{F}_n(\hat{r}_n^p, \vec{E}_i)$, we first express the incident field as

$$\vec{E}_i(\vec{r}_n') = \vec{p}_e E_i(\vec{r}_n') \tag{3}$$

$$\vec{H}_i(\vec{r}_n') = \vec{p}_h H_i(\vec{r}_n') = \vec{k}_i \times \vec{E}_i(\vec{r}_n')/Z_0$$

where $\vec{p}_e$ and $\vec{p}_h$ represent the directions of the incident electric and magnetic field respectively and Z_0 is the free space wave impedance. Establishing a local coordinate system, say Γ', originating at the center of a sub-aperture and in which $\hat{e}_x, \hat{e}_y$ are any two orthogonal unit vectors tangential to the sub-aperture, and in which $\hat{e}_z$ points into the cavity, $\vec{F}_n(\hat{r}_n^p, \vec{E}_i)$ could be decomposed into $\hat{\theta}$ and $\hat{\phi}$ polarization

$$\vec{F}_n(\hat{r}_n^p, \vec{E}_i) = F_{n\theta}(\hat{r}_n^p, \vec{E}_i)\hat{\theta}_n + \vec{F}_{n\phi}(\hat{r}_n^p, \vec{E}_i)\hat{\phi}_n \tag{4}$$

with

$$\begin{aligned}\vec{F}_{n\theta}(\hat{r}_n^p, \vec{E}_i) = [(&p_{ex} + p_{hy}\cos\theta_n^p)\cos\phi_n^p + \\ &(p_{ey} - p_{hx}\cos\theta_n^p)\sin\phi_n^p]I(\hat{r}_n^p, \vec{E}_i)\end{aligned} \tag{5}$$

$$\begin{aligned}\vec{F}_{n\phi}(\hat{r}_n^p, \vec{E}_i) = [(&p_{ey}\cos\theta_n^p - p_{hx})\cos\phi_n^p - \\ &(p_{hy} + p_{ex}\cos\theta_n^p)\sin\phi_n^p]I(\hat{r}_n^p, \vec{E}_i)\end{aligned} \tag{6}$$

where θ_n^p and ϕ_n^p represent the elevation and azimuth angles of the axis of the *p-th* ray-tube of the *n-th* sub-aperture, measured in the local coordinate system Γ', p_{ex} and p_{ey} are the components of $\vec{p}_e$ in Γ' and similar for p_{hx} and p_{hy}. The exact form of $I(\hat{r}_n^p, \vec{E}_i)$ relies on the shape of the sub-aperture (see Ref. [3]).

Rays are bounced back and forth inside the cavity. After each reflection, the magnitude is determined by

$$\vec{E}(\vec{r}_i) = [R]\cdot \vec{E}(\vec{r}_{i-1})\cdot [DF]_{i-1} e^{-jks} \qquad (7)$$

where $\vec{r}_i$ is the location of the i-*th* reflection, $s = \left|\vec{r}_i - \vec{r}_{i-1}\right|$, $[DF]_{i-1}$ is the divergence factor at the (i-1)-*th* reflection location, [R] is the reflection matrix of the cavity wall which could be written in the PEC case as

$$\vec{E}^r = \begin{bmatrix} E_\perp^r \\ E_{//}^r \end{bmatrix} = [R]\cdot \vec{E}^i = \begin{bmatrix} -1 & 0 \\ 0 & 1 \end{bmatrix} \cdot \begin{bmatrix} E_\perp^i \\ E_{//}^i \end{bmatrix}$$

where superscripts *r* and *i* denote the reflected and incident wave respectively, and where $\perp$ and // represent the perpendicular and parallel polarization. When a cavity is coated with materials, the impedance boundary condition could be used casually instead of the PEC boundary condition. Easy manipulation of boundary conditions is another advantage of ray-based techniques over other methods. The divergency factor is determined by *s* and the principal radii of the curvature of the wavefront, say R_1 and R_2, at $\vec{r}_{i-1}$

$$[DF]_{i-1} = \frac{1}{\sqrt{1+s/R_1}}\cdot\frac{1}{\sqrt{1+s/R_2}} \qquad (8)$$

Note that the reflection field is singular if the i-*th* reflection is located at the caustics, i.e., $s = -R_1$ or $s = -R_2$. The caustic problem is inherent to all GO-based techniques. When it occurs, we chose to abandon the ray being traced for efficiency considerations.

Rays could exit from either the front end or the rear end. In the first case, the far zone scattering field is determined by the AI method. In the second case, RI could be used to calculate the far field contribution of a ray tube directly without tracing it back. Without wall losses, the cross section area of the reflected ray-cube, say *S*, could be determined via energy conservation by

$$S_0\left|\vec{E}_0\right|^2 = S\left|\vec{E}\right|^2 \qquad (9)$$

where S_0 is the initial beam solid angle of the ray-tube.

III. EFFICIENCY IMPROVEMENTS

The major thrust of the GRE method is to trace massive amounts of ray-tubes inside an arbitrarily shaped cavity. Usually, 10^5 - 10^6 rays are expected; however, if the axial length of the cavity is about 100λ, this number could reach 10^7 - 10^8. Therefore, ray tracing efficiency is of paramount importance.

Ray tracing is essentially a computer graphics topic. In our context, its efficiency is determined rather by the accuracy of scattering field computation than by the quality of graphic displaying. We can further divide the ray tracing problem into two weakly coupled problems: determination of the reflection position and computation of the reflected field. In general, when we calculate a GO ray reflection, we need to reconstruct the local cavity from those discrete points surrounding the reflection point. For a fixed set of discrete points, if their is a better way to reconstruct the local surface so that the resultant reflection calculation is more accurate, we can use less discrete points to model the cavity. The efficiency of determining the reflection position in a discrete cavity is essentially dominated by the number of discrete points being used to describe the cavity. Thus these two problems are weakly coupled in this sense. In general, we can improve the overall efficiency by working on each problem individually.

A. Ray Tracing

Ray tracing involves finding the reflection of a ray-tube. During each ray tracing, triangular patches were used to determine the reflection position, though in some cases as a preliminary step. Basic ray tracing algorithms include two procedures: 1) Determination of possible intersections of a ray and all triangular patches; 2) Sorting the distance between the current position and all possible intersections. The shortest distance corresponds to the actual reflection. We attempt to improve the efficiency of each procedure in the following.

A.1 Determine Intersections

The traditional way to determine a possible intersection starts from calculating the intersection of a ray and the plane where a triangular patch is located [9]. Considering a ray originating at (x_0 , y_0 , z_0) and shooting towards (k_x , k_y , k_z), the ray function is written as

$$x = k_1(z - z_0) + x_0, y = k_z(z - z_0) + y_0$$

with $k_1 = k_x / k_z$ and $k_2 = k_y / k_z$. This requires two multiplications and four summations (we do not consider those operations solely related to the ray function because they are performed only once for a ray but not for all triangular patches being tested.). The plane function of a triangular patch, written as $ax + by + cz + d = 0$, could be determined by the coordinates of its three vertices by solving a set of inhomogeneous linear equations, which requires 36 multiplications/divisions and 20 summations. The solution of the intersection needs additional seven multiplications/divisions and six summations. Next, the intersection is tested to determine whether it is inside the triangular patch or not. We adopt the following scheme: 1) Three vectors were constructed by connecting three vertices to the intersection. This requires nine summations. 2) All cross products between any two of the three vectors were gathered. This requires 18 multiplications and nine summations.

3) All dot products of any two vectors obtained in step two were obtained. This requires nine multiplications and six summations. If the intersection is inside the triangular patch, all cross products must be in the same direction if being calculated with a certain circulation order. Otherwise, their must be one cross product with a sign different from the others. In fact, if we find that two dot products have different signs, we can reach a conclusion immediately. This step requires 27 multiplications and 24 summations in the worst case. Thus in the traditional method, totally 72 multiplications/divisions and 64 summations are needed in the worst case (136 flops).

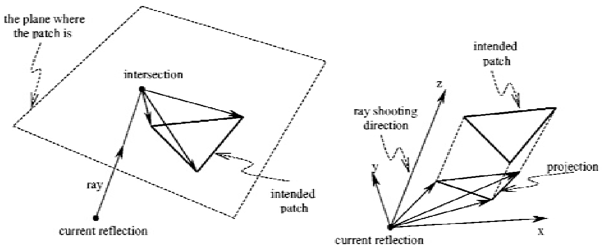

Traditional intersection determination approach.

Proposed intersection determination approach.

Fig. 1. Comparison of traditional and proposed intersection determination approaches.

The key to efficiency improvements is to bring 3-D operations to two-dimensional (2-D) operations. To do so, we first project the three vertices of a triangular patch onto the *x*-*y* plane of another coordinate system originating at (x_0, y_0, z_0) and whose *z*-axis coincides with the direction of the ray. This requires 18 multiplications and 21 summations. Then all cross products between any two of three 2-D vectors obtained in the first step are calculated. If the intersection is inside the triangular patch, all three cross products must be of the same sign when being calculated with a certain circulation order. Otherwise, their must be one cross product with a sign different from the others. This step requires six multiplications and three summations. Therefore, the proposed scheme requires a total of 24 multiplications and 24 summations (48 flops). Compared with the traditional approach, this algorithm needs 35% less flops and hence is 2.83 times faster. Moreover, this algorithm is more accurate and robust because it does not involve any division operation.

A.2 Ray Tracing In Cavities

As has already been pointed out, the heart of any ray tracing algorithm is sorting and the key to efficiency improvements is exploiting data coherence [9], [10]. An efficient algorithm is typically achieved by avoiding expensive intersection computation as much as possible and by sorting the least possible amount of intersections or no such sorting at all. If all 3-D discrete points are given without any coherence, it would be hard to improve the efficiency.

Let us assume that all discrete points are given in *m* consecutive cuts along the *z*-axis and let us call them *z*-cut. Discrete points in one *z*-cut form a polygon (*z*-polygon) and those in adjacent cuts form a section of the cavity when connected. The whole cavity is formed by (m -1) such sections, e.g. Fig.5 and Fig.6. With this model, we can search for the next reflection section by section from where the current reflection is and along either positive or negative *z*-directions, depending on the direction of the ray. In this manner, the first intersection must be the actual reflection and no sorting is needed at all. We call this method the sectional algorithm.

In fact, 3-D discrete points are either specified by physical measurement or generated by CAD software. It would be natural to require them to be generated in the above manner. For those models which are different and can not be regenerated, we may run a pre-processing program to reform them. In the following, we shall assume that such a model is always available.

The sectional algorithm totally avoids sorting, but the number of intersection computations could still be large. We can further improve the performance for convex cavities with the following Wavefront Advancing and Candidate Narrowing (WACN) algorithm. This algorithm starts from computing the intersection of a ray and a *z*-cut and determining whether the intersection is inside the *z*-polygon. If the intersection is out of the current *z*-polygon but is inside the previous *z*-polygon, it must be reflected by the section formed by these two *z*-polygons. To test whether an intersection is inside a *z*-polygon, we need to specify a gauge point for each *z*-polygon. To understand the role of gauge points, we notice that any 2-D line (formed by adjacent vertices of a *z*-polygon) divides a 2-D space (or hyper plane) into two half-spaces. When all points in one half-space are substituted into the line equation, the results must bear the same sign [10]. If the line equation is adjusted such that any point from the interior of the polygon yields a positive (or negative) sign when being substituted into the line equation, we can determine whether an intersection is inside a *z*-polygon or not. A gauge point serves this purpose and it could be any point inside a *z*-polygon. A 2-D line equation $ax+by+cz+d=0$ could be solved by the coordinates of its two vertices with six multiplications/divisions and three summations. The gauging and the determination procedures totally require four multiplications and four summations. Thus for one possible triangular patch, ten multiplications/divisions and seven summations (17 flops) are required. This is about 35% of the proposed intersection tests needed. Since the current wavefront advances consecutively, we call it Wavefront Advancing.

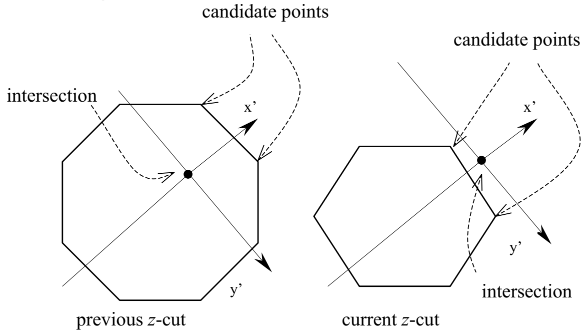

Fig. 2. The local coordinate systems and candidate points that the candidate triangular patch must contain.

If a reflection is about to happen in a section, the candidate triangular patches which are possible for actual reflection could be further narrowed down. This is accomplished through the following steps: 1) In the previous *z*-cut (where the intersection is inside the *z*-polygon), construct a Cartesian coordinate system whose *x'*-axis is the projection of the ray on the *z*-cut and whose *y'*-axis is perpendicular to the *x'*-axis. 2) Transform all vertices of the *z*-polygon to this new coordinate system and *only* compute their *y'* components. 3) Check the signs of all *y'* components consecutively. If two adjacent *y'* components are of opposite sign, record their indices. 4) Calculate the *x'* components of the two pairs of points obtained in step three. The candidate triangular patch must contain the pair of points which both have positive *x'* components. 5) Repeat steps one to three for the current *z*-cut (where the intersection is out of the *z*-polygon). 6) Calculate the *x'* components of the two pairs of points obtained in step five. The candidate triangular patch must contain the pair of points closest to the *x'* -axis. After the above steps, only those triangular patch (not necessarily two patches) containing the two pairs of points in the current and previous *z*-cuts are possible for the actual reflection. The candidate triangular patches are narrowed down and we call this step Candidate Narrowing. Note that obtaining either the *x'* components or the *y'* components only requires two multiplications and one summation, thus expensive intersection tests are replaced by these simple operations.

B. Elementary Reflection

In this subsection, the effect of using different cavity reconstruction methods for computing the reflection will be discussed.

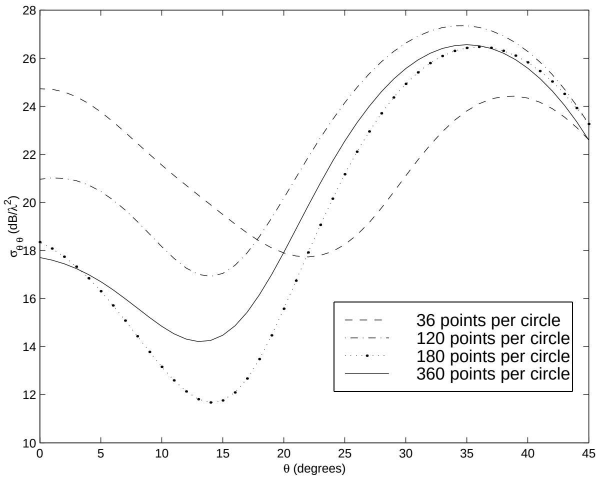

Fig. 3. Convergence of simple triangular patches for $\sigma_{\theta\theta}$ of 3λ x 9λ circular waveguide.

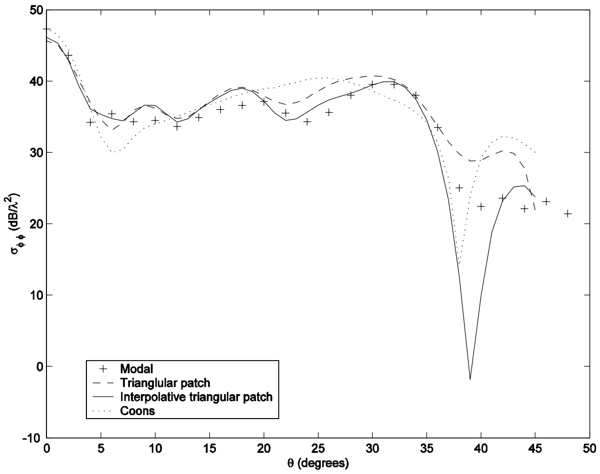

Fig. 4. $\sigma_{\varphi\varphi}$ of 10λ x 10λ circular waveguide calculated by using different reconstruction methods.

B.1 Simple Triangular Patch

In this approach, each triangular patch is considered as a simple plane. Since the principal radii are infinite, the caustic problem does not exit. In general, more triangular patches should be used if better accuracy is required. To study the convergency, we calculate the θθ polarized mono-static RCS of a circular waveguide. The waveguide is of 3λ in diameter and 9λ in length. Different numbers of triangular patches per section, which are in turn represented by the number of discrete points per circle, is being used. The results are shown in Fig.3. We observe that when only 36 points per circle (72 patches per section) are used, there are significant errors for all angles. As the number of patches is increased, the performance improves and 180 points per circle yields errors within 3dB/ λ^2 compared with 360 points per circle. Fig.4 shows the φφ polarized mono-static RCS of a circular waveguide of 10λ in diameter and 10λ in length. 180 points per circle are used for reconstruction by simple triangular patches. Ray tracing is confined within 45^o and the effective angle is up to 30^o - 35^o according to theory [3]. It is observed that the results agree with those obtained by Modal analysis well up to 35^o.

Using more triangular patches makes ray tracing less efficient. In the following, we shall explore other possibilities with better performances.

B.2 Coons Patch

Since the inaccuracy with simple triangular patches is caused by the assumption of infinite principal radii, it is natural to consider using surfaces with curvature. Here we choose Coons patch. The Coons patch belongs to the family of Hermitian bicubic parametric patches. It only uses the information on its four corners to determine the parameters. To further introduce this method, let us denote a Coons patch with two parameters (u, v) as $R(u, v) = \{x(u, v), y(u, v), z(u, v)\}$, with $0 \le u \le 1$ and $0 \le v \le 1$. If uv is used as an abbreviation for $R(u, v)$, then 00, 01, 10, 11 represent the four corners respectively; 00_u, 01_u, 10_u, 11_u, 00_v, 01_v, 10_v, 11_v represent the first order tangential derivatives at each corner; and 00_{uv}, 01_{uv}, 10_{uv}, 11_{uv} represent the second order tangential derivatives at each corner, which are also called *twists*. A Coons patch is then expressed as

$$uv = (u^3, u^2, u, 1) \cdot [H] \cdot [M] \cdot [H]^T \cdot (v^3, v^2, v, 1)^T \tag{10}$$

where

$$[M] = \begin{bmatrix} 00 & 01 & 00_v & 01_v \\ 10 & 11 & 10_v & 11_v \\ 00_u & 01_u & 00_{uv} & 01_{uv} \\ 10_u & 11_u & 10_{uv} & 11_{uv} \end{bmatrix}$$

$$[H] = \begin{bmatrix} 2 & -2 & 1 & 1 \\ -3 & 3 & -2 & -1 \\ 0 & 0 & 1 & 0 \\ 1 & 0 & 0 & 0 \end{bmatrix}$$

Other options for bicubic surfaces include Bézier surface and B-spline surface. They differ from Coons patch primarily by the meaning of [M] and the form of [H]. Since they are more often used in interactive graphic design, we shall not consider them here.

The great advantage of the Coons patch (as with other Hermitian patches) is that when two adjacent Coons patches are constructed separately, the first order continuity (C^1 continuity) across the patch edges is guaranteed. Thus we can construct a Coons patch whenever needed without considering the global C^1 continuity. Compared with triangle patches, which are of C^0 continuity, C^1 continuity is preferred in computer graphics because of more realistic results.

On the other hand, the Coons patch is a cubic function of each of its parameter u and v. This property causes unnecessary surface twists and it is disadvantageous when being used to calculate the reflection and the divergence factor $[DF]_i$. Fig.4 shows the φφ polarized mono-static RCS of a 10λ x 10λ circular waveguide calculated by using Coons patches with 36 points per circle. We observe that except for the main lobe, the results roughly deviate from the reference values the most.

To find the exact reflection position, we need to solve a set of linear and non-linear equations including Eq. (10) and the ray function. If the Newton iterative method is used, three to four iterations should be expected with good initial guesses and appropriate accuracy control. This procedure consumes more CPU time than the computation of the reflection field itself.

B.3 Interpolative Triangular Patch

In this approach, the reflection position is determined by treating a triangular patch as a simple plane. To compute the reflection direction and the divergence factor $[DF]_i$, the triangular patch is assumed to have curvature. Its first and second order derivatives at the reflection position are obtained by linear interpolation of those at the vertices. Compared with the Coons patch, this approach not only eliminates surface twists, but also simplifies the calculation of the reflection.

Fig.4 also depicts the φφ polarized mono-static RCS of a 10λ x 10λ circular waveguide calculated by using interpolative triangular patches with 36 points per circle. As can be seen, the results are much better than those for Coons patches with the same amount of points per circle and agree with the reference values the best (within effective angle 35^o). Compared with that of simple triangular patches, the consideration of curvature improves the accuracy to higher degree at large angles (20^o above) than at small angles. Bearing in mind that the improvements are obtained by using 20% discrete points, as in the case of simple triangular patches, we consider this as our best choice.

IV. NUMERICAL EXAMPLES

Besides the example shown in Fig.4 as a verification of our approach, we further show some more realistically shaped examples to demonstrate the versatility. The first example is a PEC cavity with a slanted front end. The cavity is formed by six sections. The first section is a slanted aperture of 10λ in length. The angle between the normal to the aperture, i.e. $\hat{n}$, and the z-axis, is 45^o. The angle between the plane, in which $\hat{n}$ and the z-axis are located, and the x-axis is 0^o.

The second section is 10λ in length and its cross section is a square with side lengths of 10λ. The third section is a 6.7λ transition region where the cross section changes from a square with a side length of 10λ to a circle of 10λ in diameter. The fourth section is 8.3λ in length and its cross section is a circle of 10λ in diameter. The fifth section is another transition region of 8.3λ in length and its cross section changes from a circle of 10λ in diameter to a circle of 8λ in diameter. The final section is of 6.7λ in length and its cross section is a circle of 8λ in diameter. The geometry is shown in Fig.5 with adjusted axial ratios. The side view is shown in Fig.7 with real axial ratios. All figures are in the unit of wavelength.

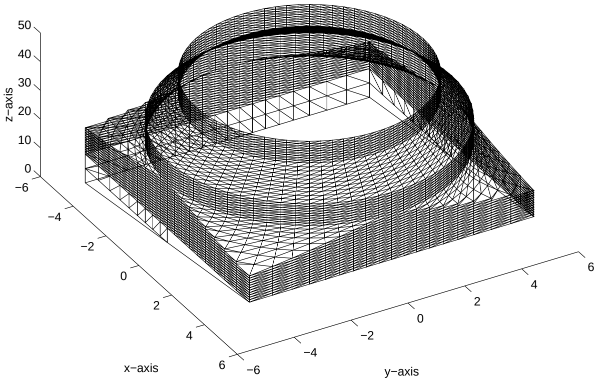

Fig. 5. Cavity with slanted front end.

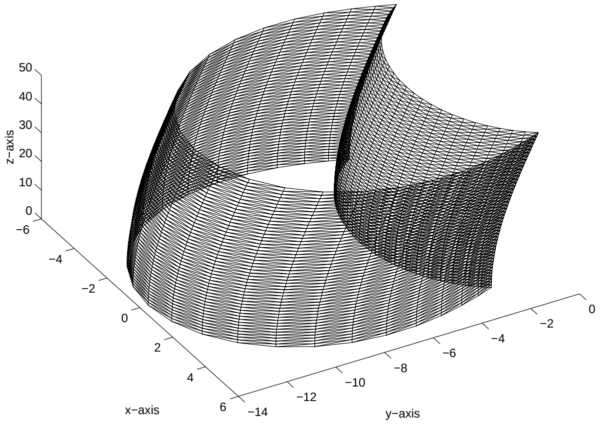

Fig. 6. Cavity with axial lofting.

For comparison, we built another model with a normal front end. The only difference is that the first section has the same cross section as the second section, i.e. the front end is perpendicular to the z-axis. Both cavities are terminated with simple PEC plates.

We use interpolative triangular patches to reconstruct the cavity with 72 points per cross section and WACN algorithm for ray tracing. Fig.9 and Fig.10 show that both θθ and φφ polarized RCS at $\varphi = 0^o$. θ takes a positive sign when an observation has a positive *x* coordinate and negative sign otherwise. As we see, the main lobes of $\sigma_{\theta\theta}$ and $\sigma_{\varphi\varphi}$ of the cavity with normal front end do not occur at the normal incidence but at some larger angles. When the front end becomes slanted, the main lobe is close to the normal incidence but shifts slightly towards negative θ direction.

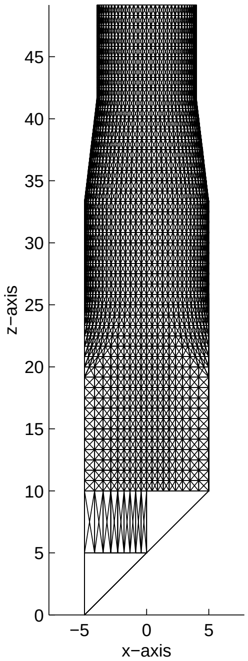

Fig. 7. Side view of the cavity with slanted front end.

Note that the results for the cavity with normal front end are not exactly symmetrical. This is due to the low grid density (eight points per λ) being used in aperture integration. The results converge slowly to symmetrical forms if grid density becomes denser. Without exception, all aperture integration in this section will be performed with the above grid density.

The second example is a concave cavity with axial lofting as shown in Fig.6 with adjusted axial ratios. A side view with real axial ratios is depicted in Fig.8. The axis is described by the following function with *z* as a parameter

$$x = 0, \qquad y = 2(\lambda - \cos(\pi z / 100\lambda))$$

Each cross section is formed by two parts. The shorter one is an arc of a circle of 5λ in radius. The longer one is described by a curve $5\lambda(\sqrt{3\lambda - \sin^2\psi} + \cos\psi)$ with $4\pi/3 \leq \varphi \leq 8\pi/3$. Both are centered at the axis. The cavity is also terminated by a PEC plate.

We use interpolative triangular patches to reconstruct the cavity with 24 points per arc, and sectional algorithm for ray tracing. Fig.11 and Fig.12 reveal that the RCS of θθ and φφ polarization at $\varphi = 0^o$ and $\varphi = 90^o$. At $\varphi = 0^o$, θ takes a positive sign when an observation has a positive *x* coordinate and a negative sign otherwise. A similar convention holds at φ = 90°. The RCS at φ = 0° has main lobes at normal incidence. The weak asymmetry is also caused by insufficient grid density in aperture integration. At φ = 90°, the main lobes of both polarization shift toward the negative direction. This corresponds to the direction where the termination could be illuminated directly. Note that there are actually two main lobes for the θθ polarization and its scattering is much stronger than that of the φφ polarization.

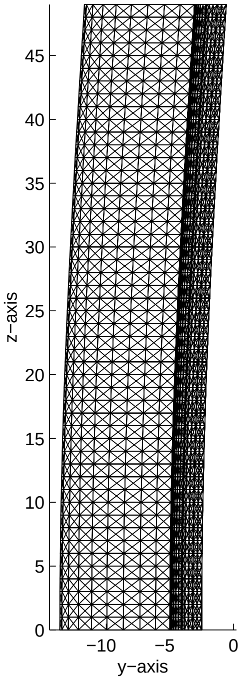

Fig. 8. Side view of the cavity with axial lofting.

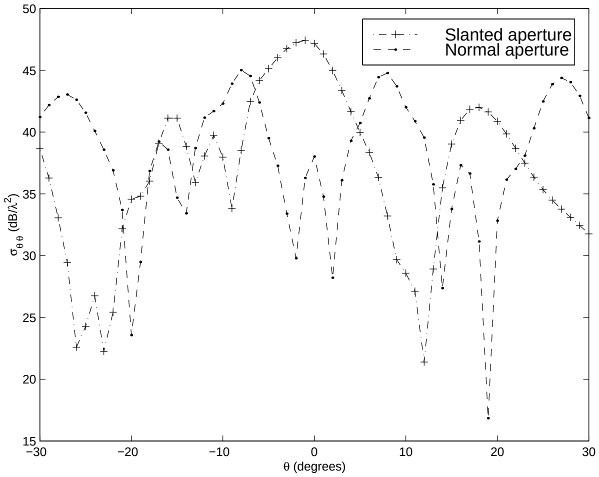

Fig. 9. Comparison of $\sigma_{\theta\theta}$ at φ = 0° of cavities with slanted and normal aperture.

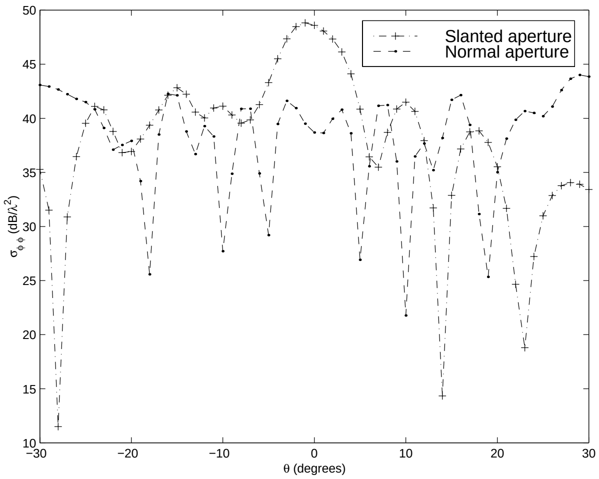

Fig. 10. Comparison of $\sigma_{\varphi\varphi}$ at φ = 0° of cavities with slanted and normal aperture.

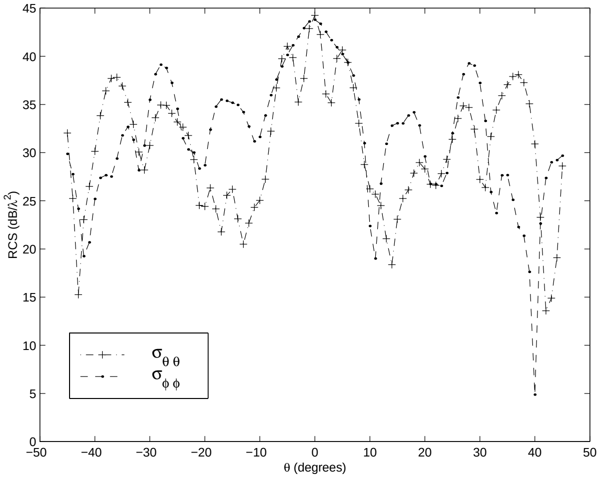

Fig. 11. $\sigma_{\theta\theta}$ and $\sigma_{\varphi\varphi}$ at φ = 0° of the cavity with axial lofting.

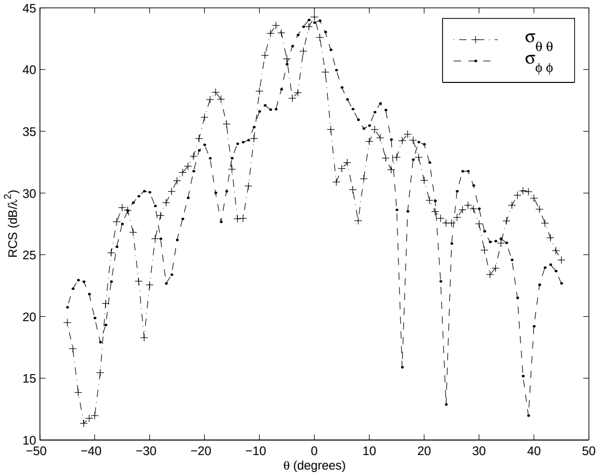

Fig. 12. $\sigma_{\theta\theta}$ and $\sigma_{\varphi\varphi}$ at φ = 90° of the cavity with axial lofting.

V. CONCLUSION

In this article, we have discussed several efficiency considerations of the GRE method for computing electromagnetic scattering from 3-D arbitrarily shaped deep cavities. An improved algorithm for testing the intersection of a ray and a triangular patch is proposed, which is 2.83 times faster than the traditional approach. Two efficient algorithms for ray tracing in 3-D discrete cavities - the sectional algorithm and the WACN algorithm - are also proposed. The WACN algorithm further boosts the efficiency by 2.83 times for convex cavities. The effects of using different reconstruction methods are explored. Numerical examples further show the validity and versatility of our approaches. Future work should address the implementation of these approaches on distributed computer systems.

REFERENCES:

[1] H. Ling, R. Chou and S. W. Lee *Shooting and Bouncing Rays: Calculating the RCS of an Arbitrarily Shape Cavity*, IEEE Trans. AP-37(2), pp.194-205, 1989.

[2] H. Ling, S. W. Lee and R. Chou *High Frequency RCS of Open Cavities with Rectangular and Circular Cross Sections*, IEEE Trans. AP-37(5), pp.648-654, 1989.

[3] R. J. Burkholder *High Frequency Asymptotic Methods for Analyzing the EM Scattering by Open-Ended Waveguide Cavities*, Ph.D. dissertation, The Ohio State Univ., 1989.

[4] P. H. Pathak and R. J. Burkholder *Modal, Ray, and Beam Techniques for Analyzing the EM Scattering by Open-Ended Waveguide Cavities*, IEEE Trans. AP-37 (5), pp.635-647, 1989.

[5] R. J. Burkholder and P. H. Pathak *Analysis of EM Penetration into and Scattering by Electrically Large Open Waveguide Cavities Using Gaussian Beam Shooting*, IEEE Proceedings. 79 (10), pp.1401-1412, 1991.

[6] P. H. Pathak and R. J. Burkholder *A Reciprocity Formulation for the EM Scattering by an Obstacle Within a Large Open Cavity*, IEEE Trans. MTT-41(4), pp.702-707, 1993.

[7] J. Liu and J. Jin *A Special Higher-order Finite Element Method for Scattering by Large Cavities*, IEEE AP-S Int. Symp., vol. 2, pp.1168 -1171, 2000.

[8] R. Lee and T-T Chia *Analysis of Electromagnetic Scattering from a Cavity with a Complex Termination by means of a Hybrid Ray-FDTD Method*, IEEE Trans. AP-41(11), pp.1560-1569, 1993.

[9] J. D. Foley, A. van Dam, S. K. Feiner and J. H. Hughes *Computer Graphics: Principals and Practice*, Addison Wesley, 2001.

[10] Z. Lou and G. Liao *Principles and Methods of Computer Graphics*, Fudan University Press, 1995.

Shumin Wang received the B.S. degree in physics from Qingdao University, P.R.China, and the M.S. degree in electronics from Beijing University, P.R.China, in 1995 and 1998 respectively. He is currently working towards the Ph.D. degree in electrical engineering at The Ohio State University. Since 1999, he has been a Graduate Research Associate with the ElectroScience Laboratory (ESL), The Ohio State University. His research interests include electro-static and magneto-static lens design, time-domain differential equation-based methods, high frequency asymptotic methods and their applications to scattering, packaging, microwave circuit and antenna analysis.

EM MODELING OF SURFACES WITH STOP OR GO CHARACTERISTICS – ARTIFICIAL MAGNETIC CONDUCTORS AND SOFT AND HARD SURFACES

Per-Simon Kildal[1] and Ahmed Kishk[2]

[1]Chalmers University of Technology, 41296 Gothenburg, Sweden, simon@kildal.se (www.kildal.se)
[2] University of Mississippi, University, MS 38677 USA, ahmed@olemiss.edu

Abstract:
We discuss and demonstrate by measurements and computations the relation between electromagnetic bandgap surfaces (EBG) used to realize artificial magnetic conductors and the so-called soft and hard surfaces in electromagnetics, with respect to their STOP and GO characteristics for surface waves. We show how the main characteristics of such surfaces can be modeled by using ideal surfaces representing perfect magnetic conductors (PMC) and PEC/PMC strip grids. Unfortunately, commercial codes do not allow such modeling for general shapes of the surfaces.

1. Introduction to EBGs, AMCs and soft and hard surfaces

In the last few years, there has been much research on using periodic structures to make new materials for application in the design of antennas and microwave components. Such materials are most often referred to as photonic bandgap structures (PBG), electromagnetic bandgap structures (EBG), or electromagnetic crystals. In some of this work, the main concern is the surface characteristics of the periodic structures, in the sense that the goal is to obtain a high surface impedance [1], or to remove surface waves from a dielectric substrate. This latter characteristic is herein referred to as a STOP-characteristic. A high impedance surface represents an artificial magnetic conductor (AMC). AMCs have the characteristic that electric current sources such as dipoles can be located at the surface and still radiate well. Thereby very low profile antennas can be realized [2]. Other applications of AMCs are to realize waveguides that can support TEM waves [3], which in this paper is referred to as a GO-characteristic. Actually, the waves should be regarded as quasi-TEM waves, as they only appear at the frequency where the surface impedance is infinite.

A classical relative to the above-mentioned surfaces is the transversely corrugated surface. These types of surfaces were originally been used as chokes to reduce coupling, see e.g. the recent papers [4] and [5], and in corrugated horn antennas that have found so many applications in large reflector antennas. In 1987 the relation between the corrugated surfaces and the so-called soft and hard surface described in diffraction theory and acoustics was discovered (in acoustics the soft and hard surfaces are actually soft and hard to touch). In terms of the boundary conditions of the fields, an edge in a transversely corrugated surface should be analyzed as an edge in a soft surface by using the soft diffraction coefficient, both in E-plane and H-plane (STOP-characteristics in both planes). In comparison, for a normal smooth conductor the edge is soft in H-plane and hard in E-plane. This fact was used to define soft and hard surfaces in electromagnetics [6]-[7] in terms of surface impedances and the boundary conditions in E- and H- planes. In short, the soft and hard surfaces are anisotropic. The soft surface behaves like a perfect electric conductor (PEC) in H-plane and as a perfect magnetic conductor (PMC) in E-plane, and visa versa for the hard surface, see Figure 1. The preferred illustration of an ideal soft-hard surface today is a PEC/PMC strip grid with zero strip period, or in other words, a surface with electric and magnetic conductivity in one (and the same) direction only, see Figure 2a. Note that the surfaces in the figure are color-coded with blue meaning PEC and gold meaning PMC. The PEC/PMC strip grid represents a hard surface when the strips are oriented in the same direction as the wave propagates (longitudinal strips), and a soft surface when they are oriented orthogonal to this direction (transverse strips). The concept of soft and hard surfaces has later been generalized to arbitrary orthogonal PEC/PMC anisotropy [8]-[9], but this will not be treated here.

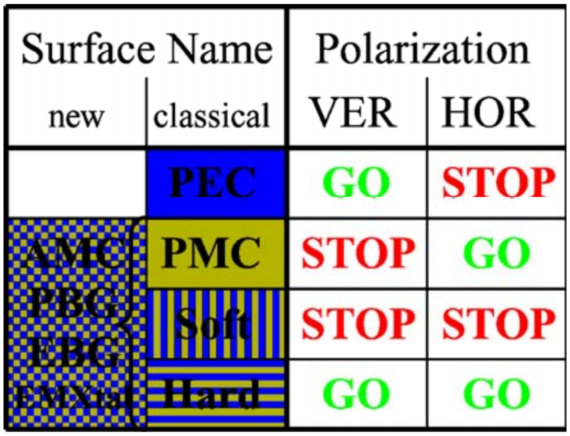

Surface Name		Polarization	
new	classical	VER	HOR
	PEC	GO	STOP
AMC PBG EBG EMXtal	PMC	STOP	GO
	Soft	STOP	STOP
	Hard	GO	GO

GO surfaces: Enhances propagation of waves along.
STOP surface: Stops propagation of waves along.
PEC = Perfect Electric Conductor
PMC = Perfect Magnetic Conductor
AMC = Artificial Magnetic Conductor
PBG = Photonic Bandgap Material
EBG = Electromagnetic Bandgap Material
EMXtals = Electromagnetic Crystals.

Figure 1. Characteristics of different types of surfaces with respect to propagation of surface waves for different polarizations (top), and explanation of abbreviations (bottom). Note that we here use the term surface waves in an extended sense, so that they even include grazing waves along a PEC surface (behaving like guided surface waves at cut-off).

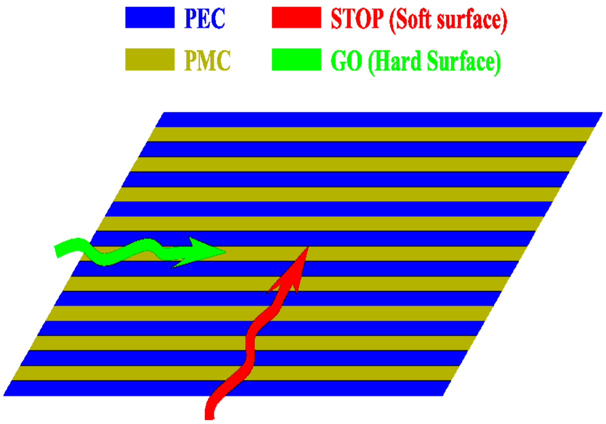

Figure 2a. PEC/PMC strip representations of ideal soft and hard surfaces. The red and green wave-shaped arrows represent the direction of propagation of the waves that makes the PEC/PMC strip surface soft and hard, respectively.

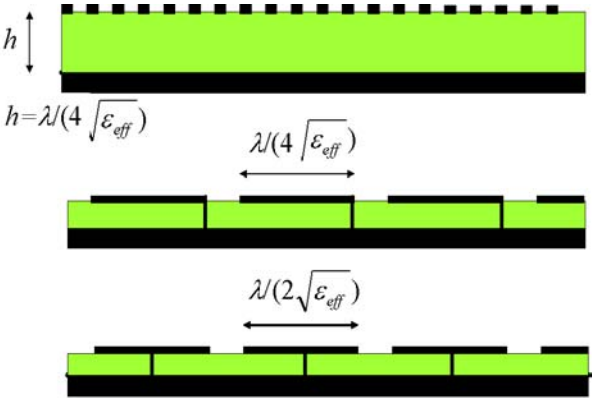

Figure 2b. Three modern realizations in terms of metal strips on grounded dielectric substrates. The upper case consists of close and narrow metal strips, in which case the thickness of the dielectric layer determines the frequency at which the surface is soft or hard. The lower case consists of wide metal strips, in which case the strip width determines the soft/hard frequency. The performance is considerably improved if the strip is grounded with metal posts or vias, as shown. In the middle case the metal posts or vias are located along one edge of the strips, in order to reduce the width to half. The effective permittivity in the formula is for the transverse strips (soft case) given by $\varepsilon_{eff} = \varepsilon_r$ *for the lower two geometries. For the hard case and the upper soft case they are given by* $\varepsilon_{eff} = \varepsilon_r - 1$.

2. EBG realizations of soft and hard surfaces

The original realizations of the soft and hard surfaces, which were initially proposed and studied, were transverse corrugations (soft), dielectric-filled longitudinal corrugations (hard), and dielectric substrates with transverse (soft) or longitudinal (hard) metal strips. These realizations give a thick surface compared to common EBGs, because the thickness $h = \lambda / 4\sqrt{\varepsilon_{eff}}$, where ε_{eff} is defined in the caption of Figure 2b. However, new and much thinner EBG-inspired realizations are readily available as shown in Figure 3, even if the detailed performance has not yet been investigated. The AMCs work also without metal posts , but the performance is reduced. In the same way the strip-loaded soft and hard surfaces work without metal posts or vias, but the performance is much better with them. The strip-loaded soft and hard surfaces suffer from severe problems with strip modes that are effectively killed with close metal connections to the ground such as posts or vias.

3. Applications of STOP Surfaces

An important application of EBGs and AMCs today is to reduce the sidelobes in E-plane (STOP-characteristic) for aperture [12] and microstrip antennas [11]. The principle of operation is readily explained in terms of the table in Figure 1. From this table it is also clear that a soft surface will provide sidelobe reduction (STOP-characteristic) of antennas in any plane and for any polarization, such as the cases treated in [13]. Different realizations of soft surfaces for sidelobe reduction are studied in [14]. Recent papers also propose metal strips in combination with an AMC (making it a soft surface) to reduce coupling [15].

4. Application of GO surfaces (quasi-TEM waveguide and hard horn)

Another application of AMCs and EBGs is, as already mentioned, TEM waveguides [3]. By using a PMC on the E-plane walls, a rectangular waveguide can support a TEM wave. Actually, if all the waveguide walls are made of a hard surface the TEM performance is better, because a TEM wave of any polarization can propagate in such a hard waveguide of arbitrary cross section. This was described already in the original papers on soft and hard surfaces. The first simulation of the field solution in a hard quasi-TEM waveguide was done by a FDTD code in [16]. The simulations were done both for realizations in terms of corrugations and strips, and the latter case included also a study of an homogenized asymptotic model for the strip grid [17]. Two simulated cases are shown in Figure 2. We see the uniform field distribution over the cross section and evanescent fringe fields around the strips (Figure 2a). In practice, the TEM waves of these ideal guides can only be present at the center frequency where the surfaces have close to ideal performance. Still, their bandwidth is sufficient to be attractive for use in cluster-fed multi-beam antennas for Ka band multimedia satellites. They are also studied at several places for use in quasi-optical grid amplifiers in the millimeter wave region (see e.g. [21]). Some attempts to realize hard horns with uniform aperture distribution were made more than 10 years ago, but at that time the numerical techniques were not developed sufficiently to control of the performance. Today, it is possible to analyze hard horns very accurately with commercial software based on FEM or FDTD approaches. The horns can be analyzed more time-efficiently by the special mode matching technique used in [22]-[23]. This makes use of asymptotic strip and corrugation boundary conditions [17] to simplify the analytical modal expansion in each cylindrical section (see Figure 4).

Hard surfaces can also be used to let waves GO past or through obstructions without generating blockage [24], and to let them GO along a metal cylinder [25].

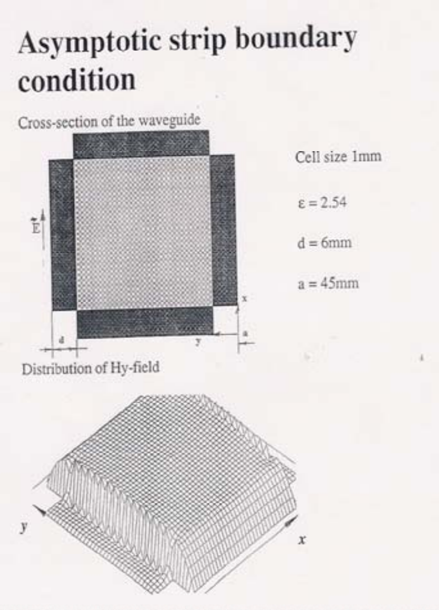

Figure 3a. Geometry (upper) and computed H-field distribution (lower) in dual-polarized quasi-TEM hard waveguide realized by strip-loaded dielectric substrate. This case has been computed by using the asymptotic strip boundary condition [17].

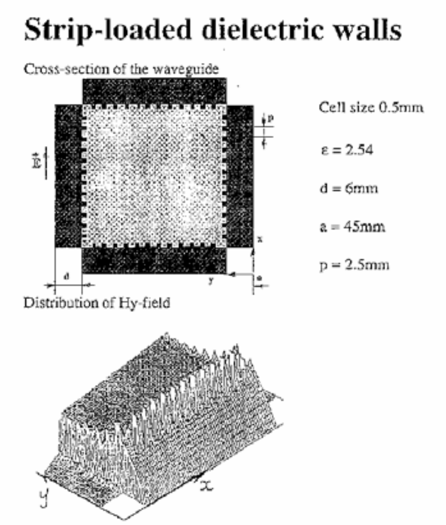

Figure 3b. Geometry (upper) and computed H-field distribution (lower) in dual-polarized quasi-TEM hard waveguide realized by modeling each metal strip of finite thickness. The computations have been done by FDTD as explained in [16].

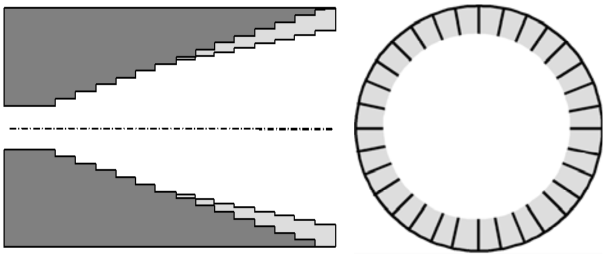

Figure 4. Hard horn geometry approximated as cascaded sections of cylindrical corrugated sections, for analysis by mode matching and generalized scattering matrices [23]. The fields in each corrugated cylindrical section is expanded in modes by making use of the asymptotic corrugation boundary condition [17]. A similar mode matching approach has been developed for strip-loaded hard horns.

5. About EM modelling of complex surfaces

The needs for future research on EM modelling in connection with AMCs and soft and hard surfaces can be divided in four categories:

A. Studies based on ideal surface models.
Existing literature does not contain any theoretical studies of characteristics of ideal PMCs or soft and hard surfaces, such as e.g. waveguide solutions and Green's functions. This would be desirable in order to foresee possible applications. Some Green's functions are available in [26] focusing mainly on studies of surface waves. Commercial codes can often model infinite plane PMCs, but finite PMCs and PEC/PMC strip models are not included. Sometimes the latter can be modelled approximately by locating PEC strips on an infinite AMC surface.

B. Studies based on homogenized boundary cond.
The major performance of a surface in different applications can most effectively be found if the periodicity of the surface can be removed by homogenization of the boundary condition. The asymptotic strip and corrugation boundary conditions in [17] are examples of homogenized boundary conditions. They have already been used in [16], [18]-[20], [23] and [26]. The homogenized strip and corrugation boundary conditions can also be used to derive analytical solutions of realized soft and hard waveguides, such as the circular strip-loaded guide in [27]. They have been used in FEM software [28], and they have been implemented in algorithms and software based on plane wave, cylindrical mode and spherical mode analysis of, respectively, planar, circular cylindrical and spherical multilayer structures [29]. They have also been implemented in software based on the moment method for cylindrical structures of arbitrary cross section, such as e.g. [30]. Commercial codes can normally not make use of homogenized boundary conditions. The impedance boundary condition is also a homogenized boundary condition that is applied to such surfaces [31]. However, it is not very convenient when modelling soft and hard surfaces because it will vary with angle of incidence. The asymptotic boundary conditions are much more accurate.

C. Studies based on exact modeling.
The exact modeling of the surfaces in all details is always desirable, but it can rarely be done due to the computational effort involved. The segment size often becomes too small to accurately model periodicity and thereby the computation time and memory becomes larger than for smooth surfaces.

D. Ray techniques.
The computational effort with FEM, FDTD and moment method for large structures can be reduced by using ray techniques. These will not be mentioned here, except referring to one of the papers in this area [32].

6. Experimental illustration of relation between AMC-type EBGs and soft and hard surfaces

In this section, we will illustrate the relation between AMCs and soft and hard surfaces by taking an AMC and transforming it to a soft/hard surface by using metal tape in the form of narrow strips, see Figure 5. The EBG surface was obtained from Ericsson AB. Some previous work on it was presented in [33]. It consists of two patch layers of Sievenpiper mushroom type [1] for 900 MHz applications. All the patches on both layers are connected to the metal ground plane by metal posts. We choose to measure coupling for both horizontal (HOR) and vertical (VER) polarizations between two quarterwave vertical monopoles and two horizontal parallel halfwave dipoles, respectively. The results in Figures 5c and 5d show the coupling after we have corrected for the mismatch of the two antennas by using the following formula:

$$C_{net} = 10\log\left\{\frac{|S_{21}|^2}{(1-|S_{11}|^2)(1-|S_{22}|^2)}\right\} \tag{1}$$

The formula represents the coupling that would be measured if we match both antennas and neglect multiple interactions between them (i.e. coupling to the

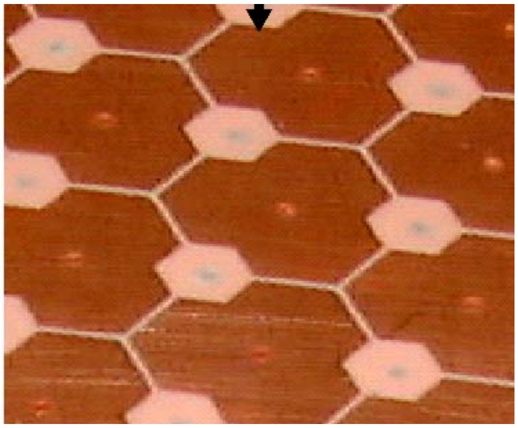

Figure 5a. Photo of the dual-layer mushroom-type AMC of Sievenpiper type.

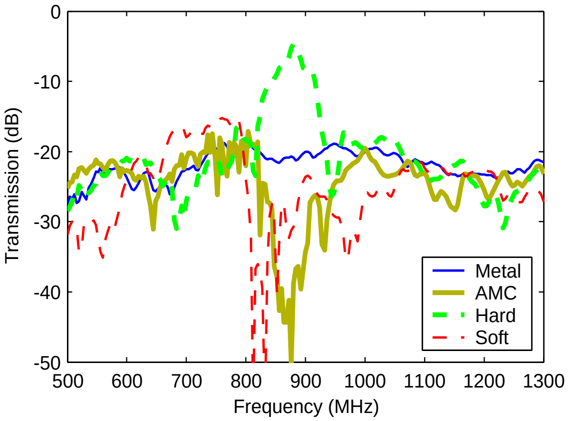

Figure 5c. Measured net transmissions between two vertical quarterwave monopoles on 4 different surfaces: The metal plate, the original AMC, the strip-loaded hard AMC (shown in Figure 5b), and the strip-loaded soft AMC.

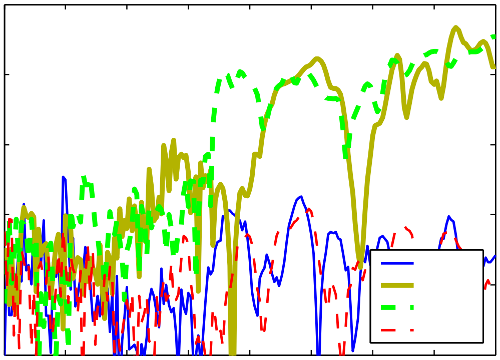

Figure 5d. Measured net transmission between two horizontal halfwave dipoles located 9mm above the 4 different surfaces.

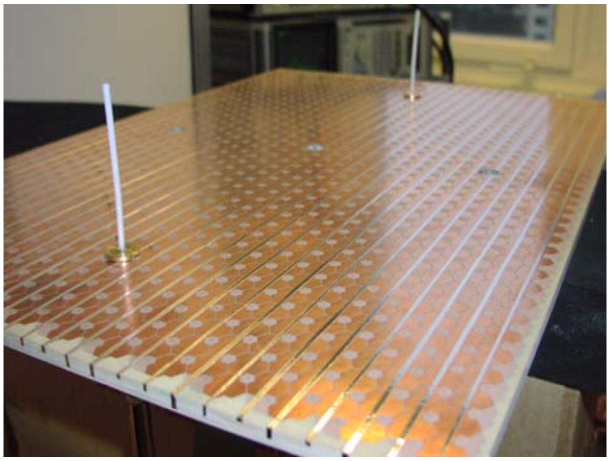

Figure 5b. Two monopoles on the dual-layer mushroom-type AMC in Figure 5a that has been transformed to a hard surface by providing it with longitudinal metal strips made from Aluminum tape. If the strips are taped to the surface in the opposite transverse direction, the surface becomes soft.

neighboring dipole and back again). This is satisfied if the distance between them is sufficiently large. We refer to (1) as the net coupling. The two antennas were mounted at a fixed distance, and four different cases were measured: metal ground plane of same size as the EBG (corresponding to a PEC), the original EBG surface working as an AMC, the EBG with longitudinal metal strips on it (corresponding to a hard surface, see Figure 5b), and the EBG with transverse metal strips on it (corresponding to a soft surface). The measured results show that both the AMC and the soft surface have a clear bandgap (i.e. STOP band) for VER polarization. For HOR polarization, there is a STOP band below 900 MHz, but a GO band above. Thus, the EBG surface acts as an AMC around 900 MHz for VER polarization, and it transforms gradually into STOP one at that frequency for HOR polarization. The PEC STOPs the waves for HOR polarization and lets them GO for VER polarization. The soft surface effectively stops the waves for both VER and HOR polarization, whereas the hard surface lets them GO. The STOP characteristics of the soft surface are not as good for VER polarization as for the AMC case, but this may be better if actual anisotropic soft EBGs of the kind shown in Figure 2b are realized. It seems to be possible to use the original EBG as a STOP surface for both HOR and VER polarization slightly below 900 MHz, due to some frequency shift between the AMC performances for the two polarizations. The GO characteristics of the hard surface are very clearly present for both polarizations.

7. Numerical results for ideal surfaces (PEC, PMC, soft and hard surfaces)

We have also computed the net coupling between VER monopoles and HOR dipoles located on the different corresponding ideal surfaces. For this we have used three different moment method codes, one commercial code WIPL-D [34] and two in-house codes. The latter are WireMoM [35] and G2DMULT [30].

1. The commercial code models the actual finite metal surfaces as an ideal PEC, and the currents on both the ground plane and the wires are solved for using the entire domain basis functions. The PMC modeling assumes an infinite ground plane. Soft and hard surfaces were modeled by locating metal strips on the PMC.

2. The WireMoM program calculates the current distribution on any wire antenna by using subsectional basis functions. The PEC and PMC ground planes are included by imaging.

3. G2DMULT uses a spectrum of two-dimensional solutions solved by the moment method to determine the coupling between antennas with a given cosine-shaped current distribution. It can handle all kind of ground planes: PEC, PMC, soft and hard. The finite widths of the different ground planes are included, which are assumed infinitely long.

The measured and computed results are shown in the Tables 1 and 2. Some values are missing in the tables because the codes could not be used, or the results were unreasonable. In particular, it was difficult to calculate horizontal dipoles located close to a PEC and a soft surface, and vertical monopoles on a PMC. The reasons are that the PEC and soft surface short-circuits HOR electric currents and make their impedances close to zero, and the impedances approach infinity for vertical monopoles on a PMC. The presented computed values correspond well to the measurements although we cannot of course predict the frequency variations due to the actual surfaces with such ideal models, but the major STOP and GO characteristics are well predicted.

8. Conclusion

We have demonstrated the relation between PBG surfaces of AMC-type and the soft and hard surfaces regarding their STOP and GO characteristics with respect to surface waves. We have also shown that there is a large need for being able to model finite and arbitrarily shaped ideal PMCs and soft and hard surfaces by commercial codes, but first the numerical techniques must be further developed to enable such code extensions.

Table 1. Measured net coupling levels in dB between wire antennas on different surfaces (ground planes) for an antenna spacing of 1.26λ in a frequency band of about 50 MHz around 900 MHz. VER means vertical, HOR means horizontal, h is height over ground. The STOP cases with low coupling are marked with bold. (Soft and hard are made by strips on AMC).

	VER monopoles	HOR dipoles	HOR dipoles
	E-plane	H-plane, h=0	H-plane, h=λ/4
Metal	-21	**-28 to -40**	**-22 to -35**
AMC	**-43 to -26**	-30 to -10	-20 to -11
Soft	**-32 to -23**	**-32 to -45**	**-22 to -35**
Hard	-5 to -14	-10 to -17	-11 to -15

Table 2. Computed net coupling levels in dB between wire antennas on different infinite ideal surfaces for an antenna spacing of 1.26λ at 900 MHz. The different results are obtained by using different codes based on the moment method. VER means vertical, HOR means horizontal, h is the height over ground and x represents missing data. The STOP cases with low coupling are marked with bold. (Soft and hard are made by PEC/PMC strips).

	VER monopoles	HOR dipoles	HOR dipoles
	E-plane	H-plane, h=0	H-plane, h=λ/4
PEC	-22, -20	**X, -30,X**	**-26, -26, -26**
PMC	**X, -30**	-20, -20, -21	-14, -13, -14
Soft	**-29, X**	**X, -30, X**	**-26, -23, X**
Hard	-10,**X**	-10,**X, X**	-13, **X**, **X**
Codes Used	G2DMULT, Wire Mom	G2DMULT, WIPL-D, Wire Mom	G2DMULT, WIPL-D, Wire Mom

Acknowledgements

The authors are thankful to Jan Carlsson and Jian Yang for providing some of the numerical results in Table 2, and to Ulf Carlberg and Jian Yang for the measured results in Table 1. We are also thankful to Björn Johannisson and Anders Derneryd at Ericsson AB for letting us use and modify their high impedance surface shown in Figure 5.

References

[1] D. Sievenpiper, L.J. Zhang, R.F.J Broas, N.G. Alexopolous, E. Yablonovitch, “High-impedance electromagnetic surfaces with a forbidden frequency band”, *IEEE Transactions on Microwave Theory and Techniques*, Vol. 47, No. 11, pp. 2059-2074, November 1999.

[2] W. E. McKinzie, R. R. Fahr, “A low profile polarization diversity antenna built on an artificial magnetic conductor,” *Proceedings of IEEE AP-S International Symposium*, San Antonio, Vol. 1, pp. 762-765, June 2002.

[3] F-R. Yang, K-P. Ma, Y. Qian, T. Itoh, “A novel TEM waveguide using uniplanar compact photonic-bandgap (UC-PBG) structure”, *IEEE Transactions Microwave Theory and Techniques*, Vol. 47, No. 11, pp. 2092 –2098, Nov. 1999.

[4] J. Carlsson and P.-S. Kildal, "Transmission through corrugated slots", *Transactions on Electromagnetic Compatibility*, vol. 37, 1, pp. 114-1121, Feb 1995.

[5] M. Albani M, P. Piazzesi, F. Capolino, S. Maci, R. Tiberio, “Shielding effect of a thick screen with corrugations”, *IEEE Transactions on Electromagnetic Compability*, Vol. 40, No. 3, pp. 235-239, August 1998.

[6] P.-S. Kildal, "Definition of artificially soft and hard surfaces for electromagnetic waves", *Electronics Letters*, vol. 24, 3, pp. 168 -170, Feb. 1988.

[7] P.-S. Kildal, "Artificially soft and hard surfaces in electromagnetics*", IEEE Transactions on Antennas and Propagation*, vol. 38, 10, pp. 1537-1544, Oct 1990.

[8] I.V. Lindell, “Ideal boundary and generalised soft and hard conditions”, *IEE Proceedings - Microwaves Antennas and Propagation*, Vol. 147, No. 6, pp. 495-499, December 2000.

[9] A.J. Viitanen, S.A. Tretyakov, I.V. Lindell, “On the realization of the generalized soft-and-hard surface”, *Radio Science*, Vol. 35, No. 6, pp. 1257-1264, November 2000.

[10] E. Lier, “Analysis of soft and hard strip-loaded horns using a circular cylindrical model”, *IEEE Transactions on Antennas and Propagation*, Vol. 38, No.. 6, pp. 783-793, June 1990.

[11] Y. Zhang, J. von Hagen, W. Wiesbeck, ”Patch array as artificial magnetic conductor for antenna gain improvement”, *Microwave and Optical Technology Letters*, Vol. 35, No. 3, pp. 172-175, Nov 5, 2002.

[12] D. Sievenpiper, J. Schaffner, J. Navarro, “Axial ratio improvement in aperture antennas using high-impedance ground plane”, *Electronic Letters*, Vol. 38, No. 23, pp. 1411-1412, 7th Nov., 2002.

[13] Ying and P.-S. Kildal, "Improvement of dipole, helix, microstrip path and aperture antennas with ground planes by using corrugated soft surfaces", *IEE Proceedings Part H*, Vol. 143, No. 3, pp. 244-248, June 1996.

[14] Z. Ying, P.-S. Kildal, and A. Kishk, "Study of different realizations and calculation models for soft surfaces by using vertical monopole on soft disk as test bed", *IEEE Transactions on Antennas and Propagation*, Vol. 44, No 11, pp. 1474-1481, Nov. 1996.

[15] H. Xin, K. Matsugatani, M. Kim, J. Hacker, J.A. Higgins, M. Rosker, M. Tanaka, “Mutual coupling reduction of low-profile monopole antennas on high-impedance ground plane”, *Electronics Letters*, Vol. 38, No. 16, pp. 849-850, 1st Aug. 2002.

[16] I. Novikova, P.-S. Kildal, M. Celuch-Marcysiak and W. Gwarek, "FDTD investigation of the field distribution in rectangular hard waveguides", *IEEE International Symposium on Antennas and Propagation*, Baltimore, July, 1996.

[17] P.-S. Kildal, A. Kishk, and Z.Sipus, "Asymptotic boundary conditions for strip-loaded and corrugated Surfaces", *Microwave and Optical Technology Letters*, Vol. 14, No. 2, pp. 99-101, Feb 1997.

[18] Ahmed A. Kishk, Per-Simon Kildal, A. Monorchio, and G. Manara" An asymptotic boundary conditions for corrugated surfaces and its application to calculate scattering from circular cylinders with dielectric filled corrugations," *IEE Proceedings, Microwaves, Antennas Propagation*, Vol. 145, No. 1, pp. 116-122, February 1998.

[19] Ahmed A. Kishk and Per_Simon Kildal," Asymptotic boundary conditions for strip-loaded scatterers applied to circular dielectric cylinders under oblique incidence," *IEEE Transactions on Antennas and Propagation,* Vol. 45, pp. 551-557, January 1997.

[20] Ahmed A. Kishk, “Analysis of Hard Surfaces of Cylindrical Structures of Arbitrarily Shaped Cross-Section Using Asymptotic Boundary Conditions,” To appear in *IEEE Transactions Antenna and Propagations*, April 2003.

[21] M.A. Ali, S.C. Ortiz, T. Ivanov, A. Mortazawi, “Analysis and measurement of hard-horn feeds for the excitation of quasi-optical amplifiers”, *IEEE Transactions on Microwave Theory and Techniques*, Vol. 47, pp. 479-487, April 1999.

[22] S. P. Skobelev, P-S. Kildal, "Analysis of a hard corrugated conical horn by using the method of generalized scattering matrices", *Proceedings of ICAP 2001*, Manchester, UK, April 2001.

[23] S. Skobelev, P-S. Kildal, “Influence of hard corrugated PBG wall design on performance of conical horn antenna”, *Microwave and Optical*

Technology Letters, Vol 32, No 4, pp 265-268, Feb. 2002.

[24] Per-Simon Kildal and A. A. Kishk and Audun Tengs, "Reduction of forward scattering from cylindrical objects using hard surfaces", *IEEE Transactions on Antennas and Propagation*, Vol. 44, No. 11, pp. 1509-1520, Nov. 1996.

[25] T. Ulversoey and P.-S. Kildal, "Improved element patterns for the line feeds of the spherical reflector antenna in Arecibo", *IEEE Transactions on Antennas and Propagation*, Vol. AP-37, 12, pp. 1624- 1627, Dec 1989.

[26] Z. Sipus, H. Merkel and P-S. Kildal, "Green's functions for planar soft and hard surfaces derived by asymptotic boundary conditions", *IEE Proceedings Part H*, Vol. 144, No. 5, pp. 321-328, Oct., 1997.

[27] A.A. Kishk, M. Morgan, “Analysis of circular waveguides with soft and hard surfaces realized by strip-loaded walls using asymptotic boundary conditions”, *Microwave and Optical Technology Letters*, Vol. 29, No. 6, pp. 433-436, June 2001.

[28] A. Freni, Z. Sipus and P-S. Kildal, "Analysis of strip loaded hard struts using finite element method and asymptotic strip boundary conditions", *Electronics Letters*, Vol. 34, No. 7, pp. 643-644, Apr., 1998.

[29] Z. Sipus, P-S. Kildal, R. Leijon and M. Johansson, "An algorithm for calculating Green's functions of planar, circular cylindrical and spherical multilayer substrates", *Applied Computational Electromagnetics Society Journal*, Vol. 13, No. 3, pp. 243-254, Nov. 1998.

[30] J. Yang, P-S. Kildal, “Presentation of the spectral electric and magnetic field integral equations used in G2DMULT for analyzing cylindrical structures of multimaterial regions,” *Microwave and Optical Technology Letters*, Vol. 34, No. 2, pp. 88-93, 20 July 2002.

[31] G. Manara, P. Nepa, G. Pelosi, “EM scattering from anisotropic impedance wedges at oblique incidence: Application to artificially hard and soft surfaces”, *Electromagnetics*, Vol. 18, No. 2, pp. 117-133, March/April 1998

[32] S. Maci, R. Tiberio, and A. Toccafondi, "Diffraction coefficient for artificially soft and hard surfaces", *Electronics Letters*, Vol. 30, No. 3, pp. 203-205, Feb 1994.

[33] J. Redvik, A. Derneryd, “PBG evaluation for base station antennas”, presented at 24th ESTEC Antenna Workshop on Innovative Periodic Antennas: Photonic Bandgap, Fractal and Frequency Selective Structures, ESTEC, Noordwijk, 30 May - 1 June 2001, The Netherlands.

[34] B. M. Kolundzija, J. S. Ognjanovic, and T. K. Sarkar, *WIPL-D: Electromagnetic modeling of composite metallic and dielectric structures, Software and User’s Manual*, Artech House, Inc., 2000.

[35] J. Carlsson, The wire antenna program WireMoM, private communications.

Per-Simon Kildal was born in Norway on July 4, 1951. He received the MSEE, PhD, and doctor technicae degrees from the Norwegian Institute of Technology (NTH), Trondheim, Norway, in 1976, 1982, and 1990, respectively. Dr. Kildal became a Member of IEEE in 1982, Senior Member in 1984 and Fellow in 1995. He was an elected member of IEEE AP-S AdCom (Administration Committee of IEEE Antennas and Propagation Society) for the period 1995-97, and served as an associate editor of the IEEE Transactions on Antennas and Propagation from June 1995 till July 1998.

He was with ELAB (the Electronics Research laboratory) at NTH from 1979 to 1989, as a principal research scientist from 1986. He is now a Professor at the Department of Microwave Technology at Chalmers University of Technology, Gothenburg, Sweden. He was since 1984 a consultant for Cornell University, Ithaca, NY, in connection with the upgrading of the radiotelescope in Arecibo, Puerto Rico. He is also consulting for others via his own company Kildal Antenna Consulting AB. This company also develops and markets commercial software for synthesis and analysis of reflector antennas.

Kildal is the principal author of more than 40 scientific articles in international journals, and he has in addition coauthored more than 30. All papers are within the area of antenna theory and design. His speciality is reflector antennas. He has also authored the textbook “Foundations of Antennas – A Unified Approach”, Studentlitteratur, April 2000 (www.studentlitteratur.se/antennas).

ELAB awarded his work in 1984, in connection with an industrial project where the results of his reflector antenna research were applied. He received the R.W.P. King Award for the best paper by a young author in IEEE Transaction on Antennas and Propagation in 1984 (about the EISCAT cylindrical reflector antenna). Later he received the S.A. Schelkunoff Transactions Prize Paper Award for the best paper in 1990 in the same IEEE Transactions (about the synthesis of the dual-reflector feed for the Arecibo radio telescope). He has given invited lectures in plenary sessions at four conferences (Antem 92 in Winnepeg, 23rd EuMC 93 in Madrid, MIKON 94 in Polen, JINA 94 in Nice, and AP2000 in Davos).

Kildal has been largely involved in the electrical design of some large antennas. The first was the cylindrical parabolic reflector antenna of the EISCAT Scientific Association. This antenna is located in North Norway and has an aperture that is l20m long and 40m wide. The second is the new Gregorian dual-reflector feed of the Arecibo radio telescope. This telescope has a spherical main reflector of 300m diameter. He has also designed feed horns for a radio telescope with 30m diameter.

Kildal is the inventor of three granted patents, and he has in addition applications that are not yet granted. Two of these designs relate to feeds for paraboloids, which are in production in Scandinavian companies. These are the dipole disk feed with beam-forming ring and the hat feed. The hat feed is also the basis of the new Swedish company COMHAT (www.comhat.se) for manufacturing of reflector antennas for millimeter wave link applications. Kildal has also started the company Bluetest AB (www.bluetest.se) for commercialization of a small reverberation chamber for testing of small antennas and mobile phones.

Kildal served 1991-94 as a Distinguished Lecturer of the IEEE Antennas and Propagation Society. He offered two lectures, on the concept of artificially soft and hard surfaces for electromagnetic waves, and on the techniques for synthesis and analysis of reflector antennas that was developed in connection with the design of the dual-reflector feed for the radiotelescope in Arecibo.

Ahmed A. Kishk was born in Egypt. He received the BS degree in Electronic and Communication Engineering from Cairo University, Cairo, Egypt, in 1977, and in Applied Mathematics from Ain_Shams University, Cairo, Egypt, in 1980. In 1981 he joined the Department of Electrical Engineering, University of Manitoba, Winnipeg, Canada, where he obtained his M.Eng and PhD degrees in 1983 and 1986, respectively.

From 1977 to 1981, he was a research assistant and an instructor at the Faculty of Engineering, Cairo University. From 1981 to 1985, he was a research assistant at the Department of Electrical Engineering, University of Manitoba. From December 1985 to August 1986, he was a research associate fellow at the University of Manitoba. In 1986, he joined the Department of Electrical Engineering, University of Mississippi. He is now a Professor at The University of Mississippi (since 1995). He was on sabbatical leave at Chalmers University of Technology during the 1994-1995 academic year. He was an Associate Editor of *Antennas & Propagation Magazine* from 1990 to 1993. He is now an Editor of *Antennas & Propagation Magazine*. He was a Co-editor of the special issue on Advances in the Application of the Method of Moments to Electromagnetic Scattering Problems in the *Applied and Computational Electromagentics Society* Journal. He was an Editor-in-Chief of the same *Journal* from 1998 to 2001.

Dr. Kishk research interest includes the areas: design of millimeter frequency antennas, feeds for parabolic reflectors, dielectric resonator antennas, microstrip antennas, soft and hard surfaces, phased array antennas, and computer aided design for antennas. He has published over 110 refereed Journal articles and book chapters. He is a coauthor of the ***Microwave Horns and Feeds*** book (London, UK, IEE, 1994; New York: IEEE, 1994) and a coauthor of chapter 2 on ***Handbook of Microstrip Antennas*** (Peter Peregrinus Limited, United Kingdom, Ed. J. R. James and P. S. Hall, Ch. 2, 1989). Dr. Kishk received the 1995 outstanding paper award for a paper published in the *Applied Computational Electromagnetic Society Journal*. He received the 1997 outstanding engineering educator award from Memphis section of the IEEE. He received the Outstanding Engineering Faculty Member of the 1998. He received the Award of Distinguished Technical Communication for the entry of IEEE Antennas and Propagation Magazine, 2001. He also received the 2001 Faculty Rsearch Award for Outstanding Performance in Research. Dr. Kishk is a ***Fellow*** member of IEEE (Antennas and Propagation Society and Microwave Theory and Techniques), a member of Sigma Xi society, a member of the U.S. National Committee of International Union of Radio Science (URSI) Commission B, a member of the Applied Computational Electromagnetics Society, a member of the Electromagnetic Academy, Chair of Physics and Engineering division of the Mississippi Academy of Science (2001-2002), and a member of Phi Kappa Phi Society.

Theoretical and Experimental Investigations of the Surge Response of a Vertical Conductor

Md. Osman Goni, Hideomi Takahashi

Abstract— **This paper describes the theoretical, simulation and experimental investigations of the surge response of a vertical conductor, including the effects of ground surface and without ground surface. One of the authors of this paper derived the formula of the surge impedance in case with ground surface and without ground surface. In this research, these theoretical formulas are examined by the simulation analysis of the vertical conductor using the Numerical Electromagnetic Code (NEC-2) as well as the experimental basis. The arrangement of the current lead wire in the vertical conductor model to be analyzed here is verified with the simulation result of the equivalent circuit model by the Electromagnetic Transients Program (EMTP).**

Keywords— **EMTP, Lightning surge, Numerical electromagnetic field analysis, Tower surge impedance, Vertical conductor.**

I. INTRODUCTION

PREDICTION of lightning surges is very important for the design of electric power systems and telecommunication systems. In particular, tower surge impedance is an important factor in analysis of the lightning performance of transmission lines. Therefore, a number of experimental and theoretical studies on tower surge impedance have been carried out [1]–[11].

The first theoretical formulation of tower surge impedance was proposed by Jordan [1]. The tower was approximated as a vertical cylinder having a height equal to that of the tower, and a radius equal to the mean equivalent radius of the tower. Theoretical formulations of tower surge impedance based on the electromagnetic field theory were proposed by Lundholm *et al.* [2], Wagner and Hileman [3], Sargent and Darveniza [4] and Okumura and Kijima [5], considering effects of the vector potential generated by the injection current into the tower only.

Another experimental value for actual transmission towers was reported by Kawai [6]. He used a direct method to measure tower surge impedance. His experimental results showed that the tower response to a vertical current is different from the response to a horizontal current. Scale-model measurements were reported by Chisholm [7], [8] and Wahab *et al.* [9]. These measurements results showed that the tower surge impedance is strongly influenced by the angle of current injection.

Recently, theoretical work was reported by Ishii and Baba [10]. They estimated the surge response of a tower by numerical electromagnetic field analysis. The calculated results were compared with the field test results [11]. The analysis showed that surge response and surge impedance of the tower depend on the arrangement of the current lead wire.

One of the authors derived the formula of surge impedance with ground surface: $Z = 60 \cdot \{ln(2\sqrt{2}h/r_0) - 1.983\}\,(\Omega)$ and without ground surface: $Z = 60 \cdot \{ln(2\sqrt{2}h/r_0) - 1.540\}\,(\Omega)$ [12]. The theoretical formula of surge impedance with the ground surface is very close to the well known experimental formula of Hara *et al.* [13]. In this paper, we investigate the surge impedance of the vertical conductor on the basis of experimental and simulation analysis. These analysis results agree satisfactorily with the theoretical values.

II. METHOD OF ANALYSIS

For the present analysis, the Numerical Electromagnetic Code (NEC-2) is employed. It is a widely used three-dimensional electromagnetic modeling code based on the method of moments [14] in the frequency domain, and is particularly effective in analyzing the electromagnetic response of antennas or of other metallic structures composed of thin wires. A vertical conductor system needs to be decomposed into thin wire elements, and the position, orientation and the radius of each element constitute the input data, along with the description of the source and frequencies to be analyzed. In the analysis, all the elements in the systems are treated as perfect conductors. To solve the time-varying electromagnetic response, Fourier transform and inverse Fourier transform are used.

The validity of the computed results when NEC-2 is applied to the analysis of surge response of a vertical conductor has been verified by comparing with experimental results. In the simulation and experimental analysis, a reduced-scale model is chosen in order to make the experiment simple and flexible. However, it is not possible to achieve the same accuracy as with the full-scale model, especially in simulating the direct method, since the geometrical size of the measuring devices is large relative to the whole system.

In the lightning surge analysis with Electromagnetic Transients Program (EMTP), the vertical conductor model has been represented by an equivalent circuit of the transmission-line type since it can be easily interfaced with EMTP. Then, the basic parameters are its surge impedance, the travelling wave propagation velocity, and the attenuation and deformation characteristics of the travelling wave. Of these, the attenuation and deformation characteristics of the travelling wave determine the reflected wave from the base of vertical conductor; that is, the wave tail after its peak in the vertical conductor's potential-rise waveform.

III. THEORETICAL FORMULA OF SURGE IMPEDANCES

One of the author's theory is able to apply widely in case of ground surface and without ground surface. Suppose that the surge electric current invades to the vertical conductor whose height is h and radius is r_0. Then the surge current wave is reflected at the ground of the perfect conductor and returns to the top of the vertical conductor.

Introducing the electric current reflectivity $\beta = 1$ and the magnetic field reflectivity $\gamma(\gamma_i, \gamma_r) = 0$, the theoretical formula of surge impedance which is very close to the well known experimental formula [13] is obtained as follows;

$$Z = 60 \cdot (\ln(\frac{h}{2r_0}) - \frac{1}{4})$$

$$= 60 \cdot (\ln(\frac{2\sqrt{2}h}{r_0}) - 1.983) \qquad (1)$$

However, if it is considered that $\beta = \gamma_i = \gamma_r = 1$, it became

$$V(t) = \frac{c\mu_0 I_0}{2\pi}\left(\ln\frac{(ct + 2r_0)}{2r_0} - \frac{ct}{2(ct + r_0)}\right)$$

The above equation can be modified by substituting $ct = 2h$ and assuming $h \gg r_0$ as follows;

$$Z = 60 \cdot (\ln(\frac{h}{r_0}) - \frac{1}{2})$$

$$= 60 \cdot (\ln(\frac{2\sqrt{2}h}{r_0}) - 1.540) \qquad (2)$$

On the other hand, if there is no ground, the following formula is induced [15].

$$V(t) = \int_0^{ct} (-E_i \cdot dl)$$

$$= \frac{c\mu_0 I_0}{2\pi}\left(\ln\frac{(ct + 2r_0)}{2r_0} - \frac{ct}{2(ct + r_0)}\right)$$

Substituting $ct = 2h$ and assuming $h \gg r_0$ in the above equation, we get

$$Z = 60 \cdot (\ln(\frac{h}{r_0}) - \frac{1}{2})$$

$$= 60 \cdot (\ln(\frac{2\sqrt{2}h}{r_0}) - 1.540) \qquad (3)$$

This formula given by (3) is the same as (2).

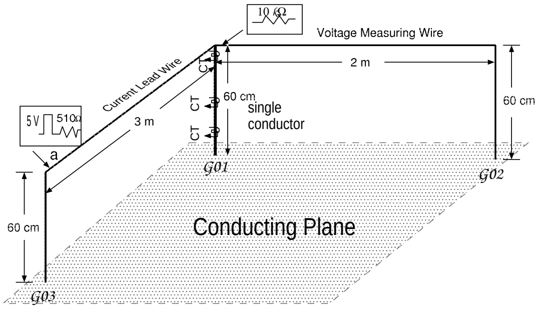

(a) With ground surface.

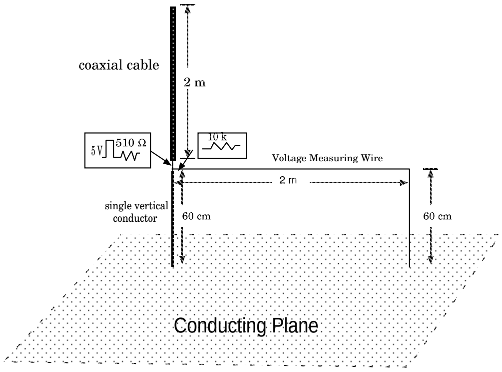

(b) Without ground surface.

Fig. 1. Arrangement of the vertical conductor system.

TABLE I
SPECIFICATIONS OF MEASURING EQUIPMENT

	Equipment	Frequency	Sensitivity
Current sensor	Tektronix CT-1	25kHz∼ 1GHz	5mV/mA ± 3% into 50Ω load.
Voltage sensor	Tektronix P6243	DC∼ 1GHz	10:1
Power supply	Tektronix 1103	40∼ 440Hz	± 5VDC ± 2%
Recording equipment	HP54616B	DC∼ 500MHz	2Gsa/s, 8 bit word
Pulse Generator	HP8131A	DC∼ 500MHz	100mV∼ 5Vpp into 50 ohm

IV. EXPERIMENTAL AND SIMULATION ANALYSIS OF SURGE IMPEDANCE

Fig. 1 shows the reduce-scale model of the vertical conductor system for the simulation analysis. The arrangement of the current lead wire connected to the top of the vertical conductor with the existence of the ground surface and without ground surface are indicated in Fig. 1(a) and 1(b) respectively. Whereas, Fig. 1(b) is also the case of the lightning phenomena caused by the return stroke [16]. The other type of the lightning phenomena caused by a downward travelling current wave can also be examined. For the simulation of this situation, a pulse current generator needs to be placed remotely above the

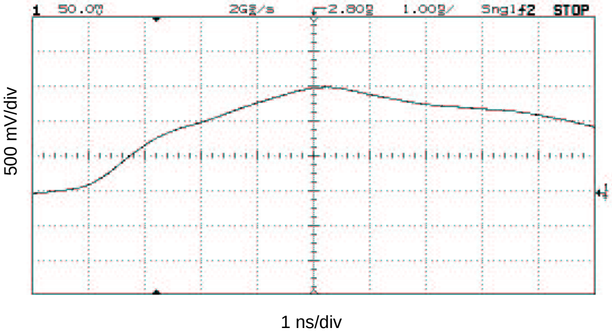

(a) Measured voltage waveform.

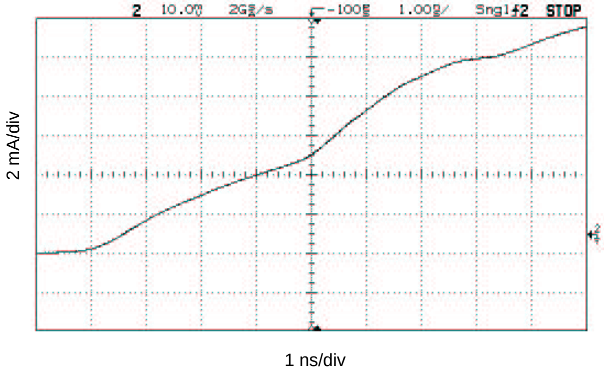

(b) Measured current waveform.

Fig. 2. Experimental results of voltage and current considering with ground surface.

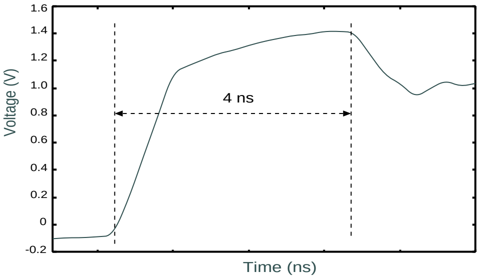

(a) Computed voltage waveform.

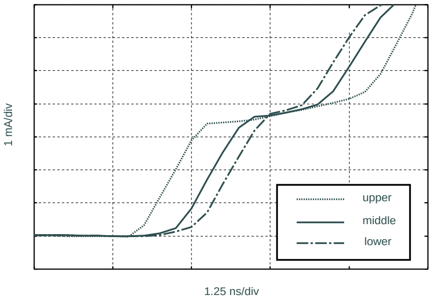

(b) Computed current waveforms.

Fig. 3. Computed waveforms of voltage at the top and currents in the various parts of the vertical conductor in case with ground surface.

channel. However, the computed waveforms for this case of current injection, a current wave travelling down the current lead wire, are similar to those of return stroke type.

The experimental arrangement of the vertical conductor system with the existence of ground surface is a little different from the simulation arrangement and is indicated in Fig. 5 of [15]. However, the experimental arrangement without ground surface is similar to Fig. 1(b). A voltage measuring wire of 200 cm in length is placed perpendicular to the current lead wire and is connected to the top of the vertical conductor which is 60 cm in height and radius of 0.05 cm. The ends of the horizontal voltage measuring wire in both cases are stretched down and connected to the ground through matching resistance. This termination condition does not affect the phenomena at the vertical conductor within 17.33 ns.

A step current pulse generator having pulse voltage of 5 V in magnitude, rise-time of 1 ns and pulse width of 40 ns is installed as indicated in both cases which is meant to incorporate the influence of the induction from the lightning channel hitting the vertical conductor. For the simulation analysis, and to save the computation time, the conductors of the system are divided into 10 cm segments. To evaluate the voltage of the top of a structure, 10 kΩ resistance was inserted between the top of the structure and the end of the voltage measuring wire. The voltage at the top of vertical conductor is measured by a voltage probe with high resistance and low capacitance(1MΩ and ¡1pF). The injection current is measured by current transformer. The specifications of the measuring equipment are shown in Table I. The waveform of current flowing through the vertical conductor is also obtained from the experiment and simulation analysis. The system of structures under those analysis was postulated to be on the perfectly conducting ground. Then we calculate the surge impedance which is defined by the ratio of the instantaneous values of the voltage to the current at the moment of voltage peak.

As the pulse applied to the current lead wire according to Fig. 1(b), the current starts flowing through the vertical conductor instantly. However, for the arrangement of Fig. 1(a), the current through the vertical conductor is delayed by the round-trip time of the travelling wave in the conductor. While in both cases, the reflection wave from the ground reaches the top of the vertical conductor at $t = 2h/c$, where c is the velocity of light. And that is why the maximum potential of the vertical conductor will occur at time $t = 2h/c$.

A. *With Ground Surface*

Considering with Fig. 1(a), we want to find the voltages and currents experimentally and with the simulation by the NEC-2. Fig. 2 shows the experimental results of the voltage and current with the ground sur-

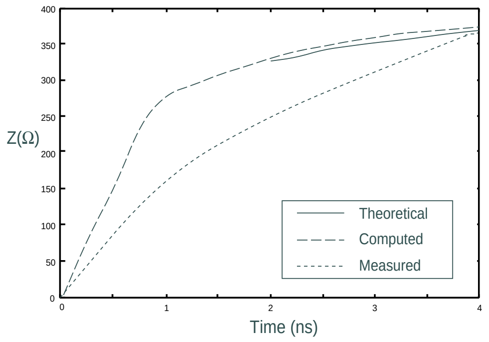

Fig. 4. Surge impedances of the vertical conductor with the ground surface at $0 < t \leq 2h/c$.

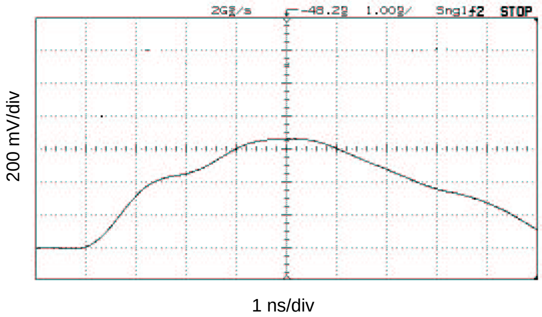

(a) Measured voltage waveform.

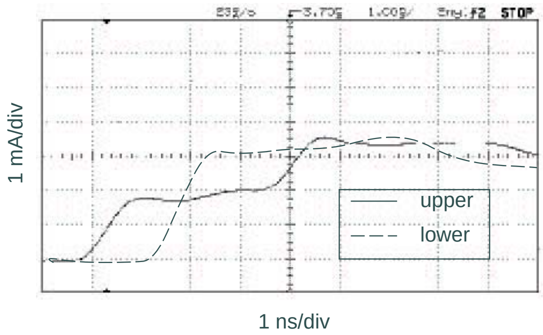

(b) Measured current waveforms.

Fig. 5. Experimental results of voltage and current considering with no ground surface.

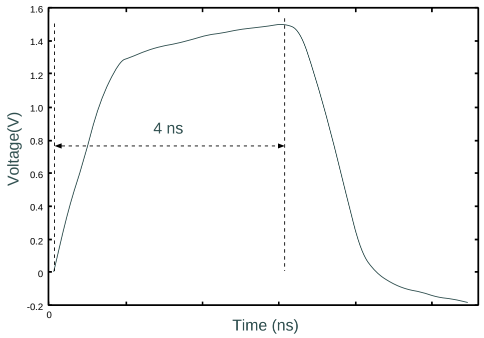

(a) Computed voltage waveform.

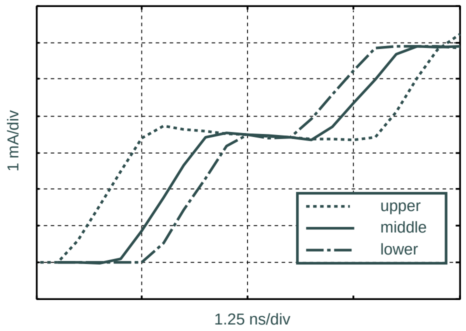

(b) Computed current waveforms.

Fig. 6. Computed waveforms of voltage at the top and currents in the various parts of the vertical conductor in case with no ground surface.

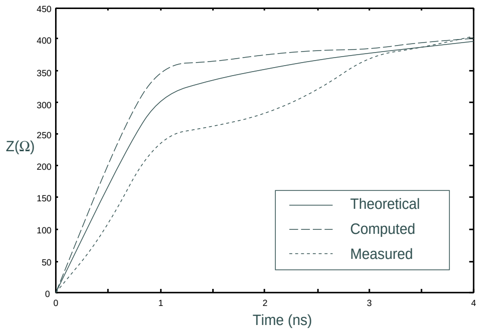

Fig. 7. Surge impedances of the vertical conductor at $0 < t \leq 2h/c$ with no ground surface.

face. Fig. 3 shows the simulation results by the NEC-2. In Fig. 3(a), the influence of the reflected wave from the ground reaches the top of the conductor is observed at $t = 2h/c = 4$ ns exactly which means that the travelling wave is propagating at the velocity of light. Fig. 3(b) shows the computed waveforms of current flowing through the vertical conductor as indicated by the mark 'CT' in Fig. 1(a). As the pulse generator is placed 300 cm from the vertical conductor, the current through the vertical conductor is being delayed approximately 10 ns. The waveforms start rising after 10 ns which can be noticed from Fig. 3. The existence of the ground surface can be observed in Fig. 3(b), where the field produced by the current injected horizontally induce current of small magnitude before the actual surge current flowing through the vertical conductor. These simulation results of currents in Fig. 3(b) obtained by the NEC-2 exactly coincide with the experimental results [15]. Then, we compare the theoretical value of the surge impedance considering the ground surface given by the (1) with the simulation and experimental results of that. Fig. 4 shows that the vertical conductor surge impedances. The theoretical values of surge impedance calculated by using (1) is just after the surge electric current reaches the ground and produce reflected current wave. As we need to know surge impedance at $t = 2h/c = 4$ ns. In these results,

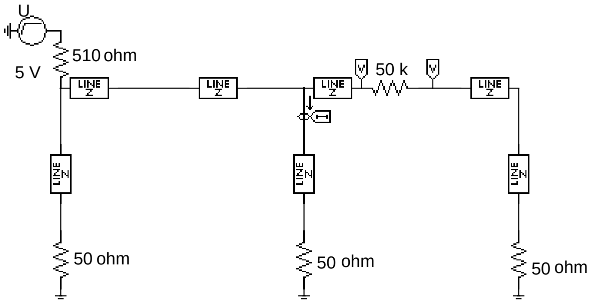

(a) With ground surface.

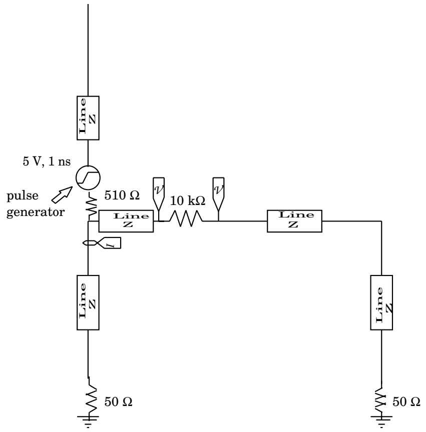

(b) Without ground surface.

Fig. 8. Equivalent circuits of the vertical conductor models.

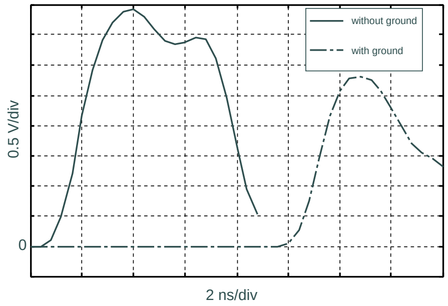

(a) Voltages across the voltage measuring resistance.

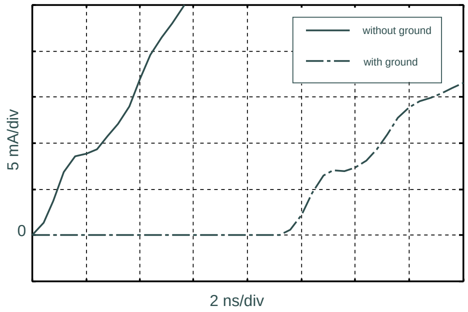

(b) Currents through the vertical conductor.

Fig. 9. Simulation results of voltages and currents by the EMTP at $0 < t \leq 2h/c$.

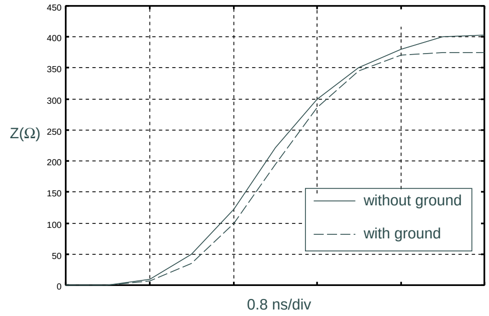

Fig. 10. Simulation results of surge impedances by the EMTP at $0 < t \leq 2h/c$.

theoretical, computed and experimental values of surge impedances are approaching closely at $t \approx 2h/c$.

B. ***Without Ground Surface***

Fig. 5 shows the experimental results of the voltage across the voltage measuring wire and currents through upper and lower parts of the vertical conductor in the absence of ground surface. The simulation results of voltage at the top of the vertical conductor and currents through different parts of it are shown in Fig. 6. However, in this case of analysis, the waveforms of current through the vertical conductor are somewhat different from Fig. 3(b) at the starting region because of absence of the ground surface. Also, the current starts flowing instantly through the vertical conductor without being delayed. Finally, the theoretical, computed and measured values of surge impedances are shown in Fig. 7. Here also we see that the values of surge impedances approach closely at $t \approx 2h/c$.

V. VERTICAL CONDUCTOR MODELS FOR EMTP ANALYSIS

The Electromagnetic Transients Program (EMTP) is probably the most widely-used power system transients simulation programs in the world today. In this section, the EMTP simulations based on the circuit theory were perfomed for the vertical conductor model with ground and without ground surface. In the circuit model, the line was represented by a distributed R-L-C circuit with the skin effect being neglected. The NEC-2 cannot exactly model the structures of actual towers or vertical conductors, and in addition it cannot directly interfaced with the EMTP. For the EMTP simulations, therefore, it is practical to employ an equivalent circuit of the transmission-line type for representing the vertical conductor system. In developing the model or in determining its parameters, characteristics stated in the preceding sections should be taken into consideration. In this section, vertical conductor models used so far are reviewed with emphasis on their performance in reproduction of measured waveforms of current through the vertical conductor and voltage at the top of it. The surge impedance is then calculated from the ratio of the maximum potential at the conductor top to the current through it at the time of voltage peak. Fig. 8 shows the equivalent circuit representation for the vertical conductor system considering with the existence of ground surface and without ground surface. The dimensions of these circuit models are the same as considered for the simulation and experimental model systems of Fig. 1. The voltage sensors and the current sensors indicated in Fig. 8 represent the measuring points. The surge impedances of the distributed line are used as the input data for the EMTP analysis, and are of different values depending on the height of the conductors. As the analysis with EMTP, it can be easily handled to the horizontal conductor but cannot be handled just as it is to the perpendicular conductor. Therefore, to solve the problem, the perpendicular conductor can be divided into the horizontal conductors as it makes a center level at the axis in each conductor.

Fig. 9 shows the simulation results of voltages and currents with the existence of ground surface and without the ground surface by the EMTP analysis for the equivalent circuit representation of Fig. 8. The solid lines of Fig. 9 correspond to circuit representation of Fig. 8(b) and the chain lines for the Fig. 8(a). The starting time of current flowing through the vertical conductor depends on the position of the pulse generator. As the pulse is injected at 300 cm from the vertical conductor with ground surface as in Fig. 8(a), the currents start flowing after 10 ns of currents through it in case with no ground surface. The occurrence of the reflection can also be observed in Fig. 9. Then the EMTP results of the surge impedances of the vertical conductor with ground surface and without ground surface are shown in Fig. 10.

TABLE II

Surge Impedances of the Vertical Conductor at $t \approx 2h/c$

	With ground	Without ground
Theoretical	368	395
Computed	373	402
Measured	366	406
EMTP	375	403

Theoretical, experimental and computed by the NEC-2 and EMTP results can be summarized in the Table II at $t = 2h/c$ so as to make quantitative evaluation. The surge impedance for the ground surface is naturally much lower than without ground surface that can also be realized by the (1) and (2). The theoretical values of surge impedance agree well with the computed and experimental values.

VI. CONCLUSIONS

The theoretical values of surge impedances are verified by comparing the computed and experimental results on simple structures. The difference is less than about 5%, which is within the accuracy maintained in the analysis. Also, the travelling wave propagates at nearly the velocity of light. The surge characteristics have some influence on the type of the lightning current with the presence of ground surface and without the ground surface. The difference comes from the different electromagnetic field around the vertical conductor influenced mainly by the electric fields associated with the currents propagating the vertical conductor and current lead wire. Also the restriction of the size of the perfectly conducting ground plane and the effect of the voltage probes might cause small difference in the experimental results of voltage and current waveforms.

References

[1] C. A. Jordan, “Lightning Computation For Transmission Line with Ground Wires,” *General Electric Review*, vol. 34, pp. 180–185, 1934.

[2] R. Lundholm, R. B. Finn, Jr., and W. S. Price, “Calculation of Transmission Line Lightning Voltage by Field Concepts,” *AIEE Trans.*, pt. 111, vol. 77, pp. 1271-1283, 1958.

[3] C. F. Wagner and A. R. Hileman, “A New approach to calculation of lightning performance of transmission lines(part II, III),” *AIEE Trans.*, pt. III, vol. 78/79, pp. 996-1021/589–603, 1959/1960.

[4] A. Sargent and M. Darveniza, “Tower surge impedance,” *IEEE Trans.*, vol. PAS-88, pp. 680–687, 1969.

[5] K. Okumura and A. Kijima, “A method for computing surge impedance of transmission line tower by electromagnetic field theory,” *IEE of Japan Trans. B*, vol. 105, pp. 733–740, 1985.

[6] M. Kawai, “Studies of the surge response on a transmission line tower,” *IEEE Trans.*, vol. PAS-83, pp. 30–34, 1964.

[7] W. A. Chisholm, Y. L. Chow, and K. D. Srivastava, “Lightning surge response of transmission towers,” *IEEE Trans.*, vol. PAS-102, pp. 3232–3242, 1983.

[8] W. A. Chisholm and Y. L. Chow, “Travel time of transmission tower,” *IEEE Trans.*, vol. PAS-104, pp. 2922–2928, 1985.

[9] M. A. A. Wahab, I. Matsubara, and H. Kinoshita, “An experimental evaluation of some factors affecting tower surge impedance,” *Trans. IEE of Japan*, vol. 107, pp. 171–177, 1987.

[10] M. Ishii and Y. Baba, “Numerical electromagnetic field analysis of tower surge response,” *IEEE Trans., PWRD*, vol. 12, pp. 483–488, 1997.

[11] T. Yamada, A. Mochizuki, J. Sawada, E. Zaima, T. Kawamura, A. Ametani, M. Ishii, and S. Kato, “Experimental evaluation of a LTHV tower model for lightning surge analysis,” *IEEE Trans., PWRD*, vol. 10, pp. 393–402, 1995.

[12] H. Takahashi, “A Consideration on the vertical conductor problem,” *Proc. of ICEE*, pp. 635–638, 2001.

[13] T. Hara, O. Yamamoto, M. Hayashi, and C. Uenosono, “Empirical formulas of surge impedance for single and multiple vertical cylinder”(in Japanese), *Journals of IEEJ*, 110-B, p-129, 1990.

[14] R. F. Harrington, *Field computation by moment methods*, New York: Macmillan company, 1968.

[15] H. Takahashi, E. kaneko, K. Yokokura, K. Nojima, T. Shiori, and I. Ohshima, “New Derivation method of the surge impedance on the tower model of a vertical conductor by the electromagnetic field theory (Part 3: Introduction of confined gauge potential and experimental analysis) ”(in japanese), *Proc. of IEE of Japan*, vol. 1, pp. 229–234, 1995.

[16] Y. Baba and M. Ishii, “ Numerical electromagnetic field analysis on lightning surge response of tower with shield wire,” *IEEE Trans. PWRD*, vol. 15, pp. 1010–1015, no. 3, Jul. 2000.

Md. Osman Goni was born in Bangladesh on February, 1971. He received his B.S. degree in electrical and electronic engineering from Bangladesh Institute of Technology, Khulna in 1993 and his M.S. degree from the University of the Ryukyus, Japan in 2001. He joined the Institute in 1994. He is currently a Ph.D student at the University of the Ryukyus. His research interests are electromagnetic theory, the FDTD method, surge response, MoM, NEC-2, EMTP etc. He is a member of IEEE, AGU and IEE of Japan.

Hideomi Takahashi was born in Tokyo, Japan, on November 13, 1940. He received B.S. degree from Tokyo Institute of Technology in 1963, and M.S. degree from the University of Tokyo in 1965. He joined in Toshiba Corporation and engaged in the research and development on high voltage engineering, especially vacuum interrupter and ozonizer etc. He received D.Eng. degree from the University of Tokyo in 1986. He is a professor of University of the Ryukyus. He has been engaged in education and research on power system engineering. Dr. Takahashi is a senior member of IEEE.

A Floating Random-Walk Algorithm based on Iterative Perturbation Theory: Solution of the 2D, Vector-Potential Maxwell-Helmholtz Equation

K. Chatterjee

Electrical and Computer Engineering Department
California State University, Fresno
Fresno, CA 93740-8030
Email: kchatterjee@csufresno.edu, Tel: (559) 278-6038, Fax: (559) 278-6297

Y. L. Le Coz

Department of Electrical, Computer, and Systems Engineering
Rensselaer Polytechnic Institute
Troy, NY 12180-3590
Email: lecozy@rpi.edu, Tel: (518) 276-2937, Fax: (518) 276-8761

ABSTRACT

At present multi-GHz operating frequencies, the electrical properties of high-end, multilevel IC interconnects must be described with Maxwell's equations. We have developed an entirely new floating random-walk (RW) algorithm to solve the 2D time-harmonic Maxwell-Helmholtz equation. The algorithm requires no numerical mesh, thus consuming a minimum of computational memory—even in complicated problem domains, such as those encountered in IC interconnects. The major theoretical challenge of deriving an analytical Green's functions in arbitrary heterogeneous problem domains has been successfully resolved by means of an accurate approximation: iterative perturbation theory. Initial numerical verification of the algorithm has been achieved for the case of a "skin-effect" problem within a uniform circular conductor cross section, and also for a heterogeneous "split-conductor" problem, where one segment of a square domain is conducting material, while the other segment is insulating. As an example of electrical parameter extraction using this algorithm, we have extracted the frequency-dependent impedance of the uniform circular cross-section previously mentioned. Excellent agreement has been obtained between the analytical and RW solutions, supporting the theoretical formulation presented here.

Index Terms—Floating random-walk, Helmholtz equation, Maxwell equations, perturbation theory, skin effect, IC interconnect.

I. INTRODUCTION

Advances in digital IC technology have resulted in multi-GHz operation frequencies. At such frequencies, circuit designers must account for electromagnetic phenomena that are difficult to calculate. They include skin-effect loss, frequency-dependent inductance and capacitance, slow-wave substrate coupling, distributed transmission-line propagation and high-frequency radiation. Our principal objective here is to invent a new numerical algorithm capable of efficiently describing these increasingly significant electromagnetic phenomena. Our hope is to establish a new approach for the modeling and design of complex, multilevel IC-interconnects.

Traditional numerical methods for solving electromagnetic problems, unfortunately, require a discretization mesh. Mesh size and the resultant difficulty of solution become somewhat unmanageable in complicated 3D problem domains. The random walk (RW) algorithm [1] that we present here does not employ a mesh. In essence, the algorithm executes a Monte Carlo integration [2] of an infinite series of multi-dimensional integrals by means of RWs through the problem domain. These integrals contain "surface" and "volume" Green's function kernels. Note, importantly, the RW method is inherently parallel, requiring minimal inter-processor communication.

A large portion of the traditional RW literature treats the Helmholtz equation in homogeneous problem domains [3]. This is principally because of the absence of an exact analytical Green's function in arbitrary heterogeneous domains [4]. The RW algorithm we present in this work, on the other hand is applicable to heterogeneous problem domains—essential for IC-interconnect modeling.

The primary objective of this work is the detailed theoretical formulation of a novel floating RW algorithm based on iterative perturbation theory. In Section II, we develop a vector-potential formulation of the 2D Maxwell-Helmholtz equation, suitable for skin-effect analysis. A derivation of the relevant Green's functions for the 2D Maxwell-Helmholtz equation using iterative perturbation theory is given in Section III. In Section IV, we apply the Green's functions defined in Section III to define a specific floating RW algorithm. Section V presents the results of a numerical 2D skin-effect problem analysis within a circular conductor cross section, including the frequency-dependence impedance per unit length for the circular cross section at different frequencies. This section also contains the results for a heterogeneous "split-conductor" problem, where one segment of a square cross section is electrically conducting, while the other is insulating. For each one of these problems, comparison with an exact, analytical solution is provided. Lastly, Section VI summarizes our work and indicates possible future directions.

II. PROBLEM FORMULATION

Consider a 2D solid-conductor cross section in the xy plane, where we impress a z-directed current density at the conductor surface. We define a corresponding current-density phasor J_z in the harmonic steady state. We, furthermore, neglect any free-charge density as an approximation. Time-harmonic Maxwell's equations require that the electric-field phasor within the conductor cross section satisfy the scalar Helmholtz equation [5]:

$$\nabla^2 E_z - \gamma^2 E_z = 0. \tag{1}$$

Above, $\nabla^2 = \partial^2/\partial x^2 + \partial^2/\partial y^2$; $E_z = E_z(x, y)$; $\gamma^2 = -\mu_0 \varepsilon \omega^2 + i\mu_0 \sigma \omega$; ω, μ_0, ε and σ are operation frequency, free-space magnetic permeability, permittivity and conductivity, respectively. At the conductor surface, the impressed current density expresses itself as a boundary condition in electric field by means of the Ohm's Law constitutive relation:

$$E_z = \frac{J_z}{\sigma}. \tag{2}$$

Equations (1) and (2) essentially describe the so-called 2D "skin-effect problem" in our conductor. Electric field, or equivalently, current density, will vary within the conductor as a function of frequency and material parameters, subject to an applied surface boundary condition. We choose now to reformulate the problem, using vector potential $\mathbf{A} = A_z(x, y)\hat{\mathbf{e}}_z$, with $\nabla \times \mathbf{A} = \mathbf{B}$ in the Coulomb gauge $\nabla \cdot \mathbf{A} = 0$ [6]. This formulation is useful in a future 3D extension of this work, because it conveniently decouples field components in the governing equations.

Equations (1) and (2), in the vector-potential formulation, generate a "forced" Maxwell-Helmholtz system:

$$\nabla^2 A_z - \gamma^2 A_z = -\mu_0 \sigma \frac{\partial \varphi}{\partial z}, \tag{3}$$

$$J_z = -i\sigma\omega A_z - \sigma \frac{\partial \varphi}{\partial z}, \tag{4}$$

where, at the conductor surface,

$$A_z = 0. \tag{5}$$

The quantity $-i\sigma\omega A_z$ above is the so-called "eddy-current density". In deriving (3) and (4) from Maxwell's equations, we observe that for no free-charge density, the scalar potential function φ is frequency independent and it is completely decoupled from vector potential A_z.

In addition, as $\partial\varphi/\partial z$ generally depends solely on x and y, and not ω, it must, as well, satisfy (4) in the dc limit $\omega \to 0$. Accordingly, $-\sigma\partial\varphi/\partial z$ can be identified as the dc current density phasor. It should be noted, that though this phasor has a non-constant harmonic temporal variation $\exp(i\omega t)$ for any $\omega \neq 0$, its spatial dependence remains identical to that at dc.

We require, as well, correspondence with surface condition (2). We must be careful, therefore, to impress a surface current density in (2) consistent with (4) and (5). In other words, we define an ideal source as one that excites our conductor cross section according to (4) and (5). An ideal source maintains the dc current-density phasor spatial dependence at the conductor surface, with the proviso that the phasor temporal dependence is of the form exp($i\omega t$).

III. ITERATIVE PERTURBATION THORY BASED GREEN'S FUNCTION

The Green's function equation corresponding to the 2D Maxwell-Helmholtz equation (3) is

$$\nabla^2 G - \gamma^2 G = \delta(\mathbf{r}-\mathbf{r_o}), \qquad (6)$$

where $G = G(\mathbf{r}\,|\,\mathbf{r_o})$ is the Green's function at (x, y) position coordinate $\mathbf{r}$ due to a 2D Dirac delta-function source at $\mathbf{r}_o$. Equation (6) does not, generally, have an analytical solution for arbitrary $\gamma(\mathbf{r})$. We will derive, nonetheless, using iterative perturbation theory [7], an approximate expression for G on the circular domain, with arbitrary radius R, shown in Fig. 1. This Green's function will allow us to later develop a novel RW algorithm for the solving 2D skin-effect equation (3). The Green's function G is assumed to be zero on the boundary of the circular domain, as the problems under consideration are Dirichlet [8] problems.

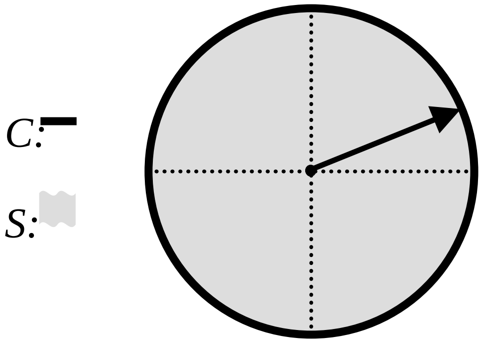

Figure 1: A circle of arbitrary radius R over which the Green's function in (6) is estimated.

Let us define the zeroth-order approximation $G^{(0)}$ for G as the solution to (6) with $\gamma = 0$. Therefore,

$$\nabla^2 G^{(0)} = \delta(\mathbf{r}-\mathbf{r_o}). \qquad (7)$$

Above, $\mathbf{r}$ (ρ, θ) is the point where the zeroth-order approximation is calculated given a delta function centered at $\mathbf{r_o}$ (ρ_o, θ_o).

Using (6) for iteration, we can then generate a first-order approximation $G^{(1)}$ in terms of $G^{(0)}$:

$$\nabla^2 G^{(1)} = \delta(\mathbf{r}-\mathbf{r_o}) + \gamma^2 G^{(0)}. \qquad (8)$$

The solution to Poisson equation (7) is well known; it has the form, in polar coordinates [9]

$$G^{(0)} = \frac{1}{4\pi}\ln\left[R^2\,\frac{A}{B}\right].$$
$$A = \rho^2 + \rho_{\mathbf{o}}^2 - 2\rho\rho_{\mathbf{o}}\cos(\theta-\theta_{\mathbf{o}}). \qquad (9)$$
$$B = \rho^2\rho_{\mathbf{o}}^2 + R^4 - 2\rho\rho_{\mathbf{o}}R^2\cos(\theta-\theta_{\mathbf{o}}).$$

Now, we are in a position to evaluate $G^{(1)}$ from (8). Using the expression for $G^{(0)}$, and with the right side of (8) as the Poisson source term, we find an expression for the first-order approximation to (6) given by [10]

$$\begin{aligned} G^{(1)}(\mathbf{r}\,|\,\mathbf{r_o}) &= \iint_S d^2 r_S\, G^{(0)}(\mathbf{r}\,|\,\mathbf{r}_S) \\ &\quad \left[\delta(\mathbf{r}_S-\mathbf{r_o}) + \gamma^2(\mathbf{r}_S)G^{(0)}(\mathbf{r}_S\,|\,\mathbf{r_o})\right] \qquad (10) \\ &= G^{(0)}(\mathbf{r}\,|\,\mathbf{r_o}) + \\ &\quad \iint_S d^2 r_S\, \gamma^2(\mathbf{r}_S)\, G^{(0)}(\mathbf{r}\,|\,\mathbf{r}_S) G^{(0)}(\mathbf{r}_S\,|\,\mathbf{r_o}). \end{aligned}$$

Note that $G^{(1)}$ given by (10), is an approximate expression for G as given by (6). The integration variable in (10) represents an infinitesimal area element on the circular-domain surface S in Fig. 1. Note, as mentioned earlier, homogeneous Dirichlet conditions have been employed in obtaining (9) and (10).

We next use this approximate Green's function $G^{(1)}$ to develop a general solution to skin-effect equation (3) within our circular domain in Fig. 1. Two integral terms arise—a line integral about the domain circumference C which takes into account the effect of boundary conditions, and a surface integral throughout the domain S itself, which takes into account the effect of the source term, and the vector-potential at the center of the circular domain is given by [11]

$$A_z\,(\mathbf{center}) = \oint_C A_z\,(R,\theta)\nabla_{\mathbf{r_o}}\,G(\mathbf{r}\,|\,\mathbf{r_o})\cdot\hat{\mathbf{n}}dc \;+ \iint_S \left(-\mu_o\sigma\frac{\partial\phi}{\partial z}\right)G(\mathbf{r}\,|\,\mathbf{r_o})ds. \tag{11}$$

Substituting (10) in (11) and after some mathematical manipulation, we obtain, for A_z at the domain center

$$\begin{aligned} A_z\,(\mathbf{center}) \approx \textstyle\int_0^{2\pi} d\theta\; A_z\,(R,\theta) \\ \left[\frac{1}{2\pi}+\frac{1}{4\pi^2}\sum_q W_q\,(\theta)\right] \\ -\left(\mu_0\sigma\frac{\partial\varphi}{\partial z}\right) \\ \textstyle\int_0^R d\rho\int_0^{2\pi} d\theta\;\rho\left[\frac{1}{2\pi}\ln\!\big(\rho/R\big)+\frac{1}{8\pi^2}\sum_q F_q\,(\rho,\theta)\right] \end{aligned} \tag{12}$$

where

$$\begin{aligned} W_q\,(\theta) &= \gamma_q^2\int_0^R d\eta\int_{(q-1)\pi/2}^{q\pi/2} d\xi\,\frac{C}{D} \\ C &= \eta\ln(\eta/R)(R^2-\eta^2) \\ D &= R^2+\eta^2-2R\eta\cos(\theta-\xi). \end{aligned} \tag{13}$$

and

$$\begin{aligned} F_q\,(\rho,\theta) &= \gamma_q^2\int_0^R d\eta\int_{(q-1)\pi/2}^{q\pi/2} d\xi\,\eta\ln(\eta/R)\ln\left[\frac{E}{F}\right] \\ E &= \rho^2R^2+\eta^2R^2-2\rho\eta R^2\cos(\theta-\xi) \\ F &= \rho^2\eta^2+R^4-2\rho\eta R^2\cos(\theta-\xi). \end{aligned} \tag{14}$$

For simplicity, above, we take γ^2 to be piecewise constant with respective values γ_q in θ-quadrants q = 1, 2, 3, and 4. The quantities within square brackets in (12) are 2D versions, respectively, of surface and volume Green's functions encountered in 3D problem domains. These Green's functions consist of two auxiliary functions W_q and F_q defined in (13) and (14). The functions represent perturbative corrections arising from the $\gamma^2 A_z$ term in the original Maxwell-Helmholtz equation (3). In (13) and (14), η and ξ are variables of integration. η takes values between 0 and R, while θ assumes values between $(q-1)\pi/2$ to $q\pi/2$ for a particular quadrant. Equations (12)–(14) are the starting point for defining a RW algorithm for solving (3) in 2D domains with arbitrary piecewise-constant spatial variation in γ, subject to arbitrary Dirichlet boundary conditions.

The total current, I, through the cross section can be calculated by integrating the current density given in (4) over the problem domain (ds being an infinitesimal area unit) and can be written as

$$I = \iint_S ds\left[-i\sigma\omega A_z - \sigma\frac{\partial\varphi}{\partial z}\right]. \tag{15}$$

The integral expression for vector potential from (12) is substituted in (15) to obtain a multi-dimensional integral expression for total current through the conductor surface.

The internal impedance per unit length is defined as[12]

$$Z_i = \frac{E_z\,(dc\,value) = \dfrac{\partial\varphi}{\partial z}}{I}. \tag{16}$$

At this point, the crucial thing to note is that for estimating frequency-dependent impedance, we need not estimate field or vector potential at a large number of points within the problem domain, or for that matter, at any point within the problem domain. The problem of impedance extraction is reduced to estimating the overall multi-dimensional integral expression for current obtained from (15) within the FRW framework to be described in the next section, and then using (16) to evaluate the internal impedance per unit length.

IV. THE FLOATING RW ALGORITHM

As mentioned earlier, the floating RW algorithm is a Monte Carlo evaluation of an infinite series of multi-dimensional integrals. The kernels of these integrals consist of products of surface and volume Green's functions. In this section, we describe the floating RW algorithm in detail in context of the skin-effect problem in a circular cross section. As shown in Fig.

2, we define RWs to start at a point, where we need to estimate A_z in (3).

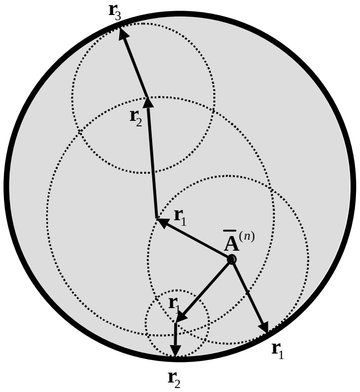

Figure 2: A schematic diagram of a circular cross section is shown. One-, two- and a three- hop RWs are represented.

The RWs propagate as "hops" of different sizes from circle centers to circumferences, consistent with a statistical interpretation [1] of (12). Maximally sized circles, subject to limitations imposed by iterative perturbation theory, are used with hop-location probability rules again consistent with (12).

We define, with each hop, a numerical weight factor derived from (12). The product of these weight factors over a walk, multiplied by the solution at the problem boundary—where the walk must terminate—gives a statistical estimate for A_Z at the RW starting point. All this, again, is entirely consistent with a statistical interpretation of (12). We can thus obtain an accurate statistical estimate for A_Z by averaging over a statistically large number of RWs. Mathematically, we can write such an estimate

$$\overline{A}_z \approx \frac{1}{N} \sum_{n=1}^{N} \overline{A}_Z^{(n)}, \tag{17}$$

where N is the number of walks and $\overline{A}_z^{(n)}$ is the nth-walk estimate. Referring, again, to Fig. (2), we see examples of three representative RWs: a one-hop, a two-hop, and a three-hop walk. The contributions from these three RWs can be written as

$$\begin{aligned}
\overline{A}_z^{(1)} &= K_S(\mathbf{r}_1), \\
\overline{A}_Z^{(2)} &= K_S(\mathbf{r}_1) + K_C(\mathbf{r}_1) K_S(\mathbf{r}_2), \\
\overline{A}_z^{(3)} &= K_S(\mathbf{r}_1) + K_C(\mathbf{r}_1) K_S(\mathbf{r}_2) + \\
&\quad K_C(\mathbf{r}_1) K_C(\mathbf{r}_2) K_S(\mathbf{r}_3).
\end{aligned} \tag{18}$$

Above, K_C represents the weight factor associated with the "surface" Green's function, the θ-integral term in (12). The function K_S represents the weight factor associated with the "volume" Green's function, the (ρ,θ)-integral term in (11). Assuming the hops are uniformly distributed in (ρ,θ), these weight factors have the form, from (12),

$$K_C = R\left(1 + \frac{1}{2\pi} \sum_q W_q(\theta)\right) \tag{19}$$

and

$$\begin{aligned}
K_S = &-\left(\mu_0 \sigma \frac{\partial \varphi}{\partial z} R^2\right) \\
&\left[\frac{1}{2} \ln(\rho / R) + \frac{1}{8\pi} \sum_q F_q(\rho,\theta)\right].
\end{aligned} \tag{20}$$

For estimating the frequency-dependent impedance per unit length as given in (16) a similar exercise is carried out using a statistical interpretation of (15). For heterogeneous problems, there are a couple of differences. First of all, the maximum hop size, which is decided by the validity of iterative perturbation theory, is different for different medium. In this paper, the maximum hop size is estimated to be the minimum of two numbers. First, we allow the first-order correction in the expression for the volumetric Green's function given in (12) to be equal to ten percent of the zeroth-order approximation and calculate a maximum hop size under this assumption. A similar process is carried out for the surface Green's function term in (12) and a maximum hop size is calculated under this assumption. The maximum hop size for our RW algorithm is the smaller of these two numbers. Secondly, the random hops are restricted by material interfaces in heterogeneous problems.

We close this section with a pseudo-code listing that defines our floating RW algorithm for estimating vector-potential.

—Floating Random-Walk Algorithm Pseudo-Code—

```
1)  Choose the point where $A_z$ need be estimated; call it AZ.
2)  Evaluate $\delta'$ = the maximum hop size as determined by validity of perturbation theory,
    according to the procedure described previously in this section.
3)  $\Delta$ = a pre-defined small number.
4)  NMAX = a pre-defined large integer.
5)  N = 0.
6)  TOTAL_SUM = 0.
7)  SUM = 0.
8)  Evaluate the maximal radius that contacts the closest problem-domain boundary,
    without passing through it; call it RMAX.
9)  RAD = MIN (RMAX, $\delta'$).
10) Draw a circle of radius RAD.
11) Hop to a point on the circumference in conformity with a uniform probability
    distribution in $\theta$.
12) Evaluate the exact weight factor $K_C$ from (13) and (19); call it KC.
13) Evaluate the exact weight factor $K_S$ from (14) and (20); call it KS.
14) KC (zeroth hop) = 1; INCREMENT = KC (previous hop) * KS (present hop).
15) SUM = SUM + INCREMENT.
16) IF (a boundary is not reached) THEN (repeat steps 8 –15).
17) IF (a boundary is reached) THEN (terminate walk; N = N + 1; SUM_TOTAL =
    SUM_TOTAL + SUM).
18) IF (N < NMAX) THEN (repeat Steps 7–17).
19) IF (N $\geq$ NMAX) THEN (AZ = SUM_TOTAL / NMAX).
20) Evaluate exact, analytical solution AZ(exact).
21) ERROR = $|$AZ – AZ(exact)$|$.
22) IF (ERROR > $\Delta$) THEN (NMAX = NMAX * 1.2; repeat steps 5 –21).
23) IF (ERROR $\leq \Delta$) THEN (AZ = estimated value of $A_z$).
```

V. VERIFICATION WITH THE HELP OF BENCHMARK PROBLEMS

The principal objective of this work is to formulate and to define a novel RW algorithm for 2D Maxwell-Helmholtz equation solution. We have benchmarked our formulation against two known solutions. As said earlier, the first problem is a single circular cross section, where an alternating current of single frequency is impressed. Using the algorithm developed earlier, we estimate the current density profile across the cross section as well as the internal impedance. The analytical solution for the current density along a uniform, circular-conductor cross section of radius *R* is [12]

$$\frac{J_z(\rho)}{J_z(0)} = \frac{J_0(i\gamma\rho)}{J_0(i\gamma R)}, \qquad (21)$$

where J_0 is the zeroth-order Bessel function. The variable ρ here denotes radial coordinate from the conductor center. For this circular cross section, an analytical expression for the internal impedance per unit length as defined in (16) is given by [12]

$$Z_i = -\frac{i\gamma J_0(i\gamma R)}{2\pi R\sigma J_0'(i\gamma R)}. \qquad (22)$$

As mentioned earlier, the second problem solved is a heterogeneous "split-conductor" problem, where a square domain is divided into two unequal rectangular domains of insulating and conducting material, as shown in Fig. (3).

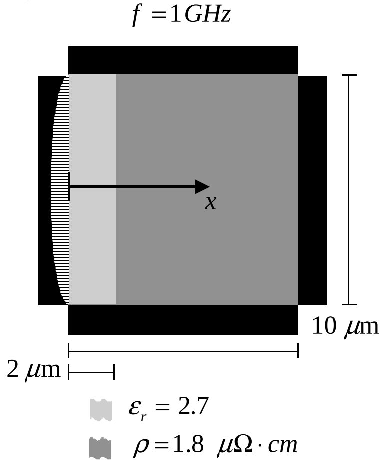

Figure 3: 2D, split-conductor problem, the geometry.

The insulating region is represented in light gray, while the conducting region is represented in dark gray. The boundary regions, where the *z*-component of the vector potential is known, are represented in black. The boundary conditions are chosen such that $A_z = 0$ in the top, bottom and right boundary regions, while $A_z = \sin(\pi y / L)$ in the left boundary region (*L* being the length of the side of the square) where the origin coincides with the left and bottom corner. Assuming the continuity of the solution and its derivative at the material interface (L_0 being the length of the dielectric), the analytical solution to this heterogeneous problem is given by [13]

$$\begin{gathered} A_z = \sin(ky) \\ \left[A \sinh\left(k_d x\right) + \cosh\left(k_d x\right)\right], 0 \le x < L_0 . \\ A_z = \sin(ky) \\ \left[C \sinh\left\{k_c \, (x - L)\right\}\right], L_0 \le x < L. \end{gathered} \tag{23}$$

The constants in (23) are given in (24) and (25) as:

$$\begin{gathered} k = \frac{\pi}{L}. \\ k_d = \sqrt{\gamma_d^2 + k^2}. \\ k_c = \sqrt{\gamma_c^2 + k^2}. \\ A = \frac{\begin{vmatrix} a_3 & a_2 \\ b_3 & b_2 \end{vmatrix}}{\begin{vmatrix} a_1 & a_2 \\ b_1 & b_2 \end{vmatrix}}. \\ C = \frac{\begin{vmatrix} a_1 & a_3 \\ b_1 & b_3 \end{vmatrix}}{\begin{vmatrix} a_1 & a_2 \\ b_1 & b_2 \end{vmatrix}}. \end{gathered} \tag{24}$$

$$\begin{gathered} a_1 = \sinh\left(k_d L_0\right), a_2 = -\sinh\left[k_c \left(L_0 - L\right)\right], \\ a_3 = -\cosh\left(k_d L\right). \\ b_1 = \sqrt{\varepsilon} a_1, b_2 = \sqrt{\frac{-j\sigma}{\omega}} a_2, b_3 = \sqrt{\varepsilon} a_3. \\ \gamma_d^2 = -\mu\varepsilon\omega^2, \gamma_c^2 = i\mu\sigma\omega. \end{gathered} \tag{25}$$

We coded the algorithm in MATLAB 5.0™, using a 400-MHz Apple PowerBook G3™ development platform. The resistivity for conducting material is given by $\rho = 1.8\,\mu\Omega - \text{cm}$ and relative permittivity of dielectric material is given by $\varepsilon_r = 2.7.$ The radius of the circular cross section is given by R = 5μm while for the split-conductor problem, the dimensions of the square cross section is given by $10\,\mu\text{m} \times 10\,\mu\text{m}.$ The respective dimensions of the insulating and the conducting materials in the split-conductor problems are shown in Fig. (3). The operating frequency $f = \omega/2\pi$ = 1GHz corresponds to a skin depth δ_s = 2.1μm and a wavelength of $1.8 \times 10^5\,\mu\text{m}.$ The propagation-constant squared (γ^2) is equal to $4.386 \times 10^{11} i/\text{m}^2$ within the conductor and equal to $-1185.431197\text{m}^{-2}$ within the dielectric at 1 GHz. Based on these numbers and the criterion given in Section IV, the maximum radius of hops inside conducting material is 0.95μm, and the maximum radii of hops within the dielectric material is $1.8 \times 10^4\,\mu$m, which is about twice the dimensions of a chip (based on a 1 cm×1cm chip). Thus we see that this perturbation theory based approach has the potential to allow meaningful interconnect analysis.

Figures (4) and (5) show the magnitude ratio and phase lag, respectively, of the skin-effect current density phasor. A total of 20,000 RWs were performed per solution point. The figures show excellent agreement between the analytical and RW solutions. The mean absolute error between exact and RW solutions was 0.001 for magnitude and 0.012rad for phase.

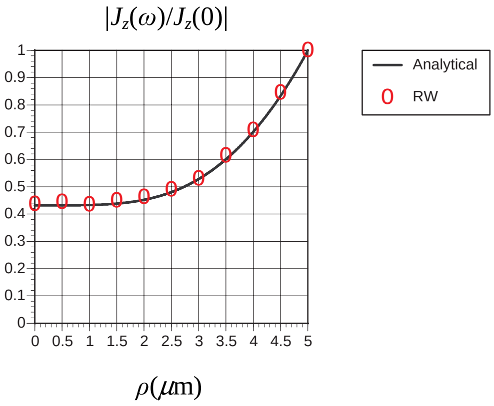

Figure 4: 2D skin-effect problem in a homogeneous circular conductor cross section, relative magnitude. Problem radius R = 5μm and ω = 1GHz.

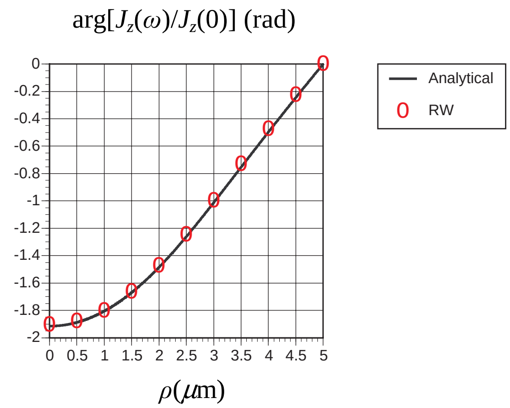

Figure 5: 2D skin-effect problem in a homogeneous circular conductor cross section, phase lag. Problem radius $R = 5\mu$m and $\omega = 1$GHz.

As expected, the total current density is maximum and equal to the dc value at the boundary, and reaches its minimum at the center of the cross section. The characteristic skin-depth decay scale is well in evidence in Fig. (4). In addition, the expected maximum phase lag occurs at $\rho = 0$ in Fig. (5). Table (1) summarizes the results for the skin-effect problem, while Table (2) shows the results for the frequency-dependent self impedance of a cross section of radius 1.0 μm at frequencies of 1 GHz, 5 GHz and 10 GHz. As expected, both the frequency-dependent inductance and frequency dependent inductance increases with frequency. For extracting impedance, a total of only 1,000 RWs were performed per points. It can be seen from Table (2), that the error in the estimate of frequency-dependent resistance and inductive impedance is around 1 percent in all three cases. Table (3) summarizes the results for the heterogeneous problem, while Figures (6) and (7) illustrates the results for the same. Again, excellent conformity was obtained between the analytical and RW solutions.

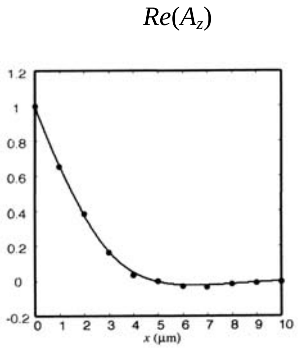

Figure 6: 2D, split-conductor problem, the real part of the solution.

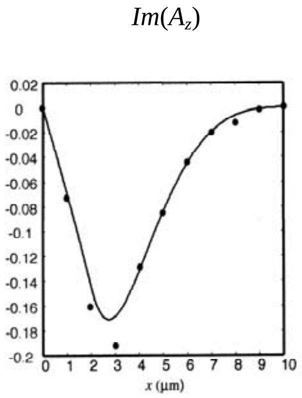

Figure 7: 2D, split-conductor problem, the imaginary part of the solution.

Frequency (GHz)	Random Walks Per Solution Point	Mean Absolute Error For Relative Magnitude	Mean Absolute Error For Relative Phase
1	20000	0.001 on a solution range (0·42 – 1·0).	0.012 on a solution range (–1·9 – 0).

Table 1: Numerical results for the 2D skin-effect problem in a circular conducting cross section.

Frequency (GHz)	Time (Seconds)	Analytical Result (Ω/m)	RW Result (Ω/m)	Error (Ω/m)
1	20	5735 + 314i	5738 + 312i	3 - 2i
5	30	5870 + 1552i	5917 + 1534i	47 - 18i
10	45	6262 + 2997i	6315 + 2962i	53 - 35i

Table 2: Numerical results for the frequency-dependent self-impedance of a conducting circular cross section.

Frequency (GHz)	Random Walks Per Solution Point	Mean Absolute Error for the Real Part of the Solution	Mean Absolute Error for the Imaginary Part of the Solution
1	2500	0.005 Solution range: –0·02 – 1·0.	0.005 Solution Range: –0·17 – 0·0.

Table 3: Numerical results for the "split-conductor" heterogeneous benchmark problem.

We will finish our discussion in this section by making a few comments on the accuracy of the solution, time and memory requirement. We have already observed the close agreement of the RW results with that of known analytical solutions. The accuracy of the solution of the solution can be enhanced by simply increasing the number of RWs as the error is proportional to $1/\sqrt{N}$, N being the number of RWs. This particular fact is a direct consequence of Central Limit Theorem [14]. The memory requirements for this technique are low as this approach does not require any numerical meshing. The time requirements of this algorithm can be further reduced by the use of variance-reduction techniques [2] and by parallelization. We plan to investigate all these issues in detail after we have applied our algorithm to more complicated structures.

VI. CONCLUSION

We have presented the theoretical basis of a novel floating RW algorithm for solving the 2D Maxwell-Helmholtz equation. The algorithm employs iterative perturbation theory. We have, as well, verified the algorithm's integrity by applying it to a homogeneous and a heterogeneous problem, possessing analytical solutions. The applicability to heterogeneous problems is a significant improvement on existing RW algorithms, an application we wish to explore further in our future work. Our algorithm can be readily extended to multi-conductor systems in full 3D. In this work, we have further demonstrated that this algorithm can be used to extract electrical parameters such as frequency-dependent impedance. We believe that with additional development, the algorithm may prove useful for electromagnetic analysis of complex, multilevel IC-interconnect structures.

Importantly, the algorithm is fully parallel. Thus, we expect significant performance acceleration in any future parallel software or hardware implementation.

Acknowledgement - This work has been sponsored by the Defense Advanced Research Projects Agency (DARPA); the New York State Office of Science, Technology, and Academic Research (NYSTAR); and the Semiconductor Research Corporation (SRC) Microelectronics Advanced Research Corporation (MARCO). The authors sincerely thank the sponsors for their support of this work.

REFERENCES

[1] Y.L. Le Coz and R.B. Iverson, "A Stochastic Algorithm for High Speed Capacitance Extraction in Integrated Circuits", *Solid-State Electronics*, vol. 35, pp. 1005–12, 1992.

[2] Ilya M. Sobol, *A Primer for the Monte Carlo Method*, Boca Raton, FL: CRC Press, 1994.

[3] K.K. Sabelfeld, *Monte Carlo Methods in Boundary Value Problems*, New York, NY: Springer-Verlag, 1991.

[4] K. Chatterjee, *Development of a Floating Random-Walk Algorithm for Solving Maxwell's Equations in Complex IC-Interconnect Structures*, pp. 28–31, Doctoral Thesis, Rensselaer Polytechnic Institute, Troy, NY, April 2002.

[5] D.M. Pozar, *Microwave Engineering, 2nd Edition*, pp. 16-7, New York, NY: John Wiley & Sons, 1998.

[6] J.D. Jackson, *Classical Electrodynamics*, *3rd Edition*, pp. 241-2, New York, NY: John Wiley & Sons, 1999.

[7] Van Dyke, *Perturbation Methods in Fluid Mechanics*. Stanford, CA: Parabolic Press, 1975.

[8] R. Haberman, *Elementary Applied Partial Differential Equations with Fourier Series and*

Boundary Value Problems, *3rd Edition*, pp. 155-7, Upper Saddle River, NJ: Prentice Hall, 1998.

[9] R. Haberman, *Elementary Applied Partial Differential Equations with Fourier Series and Boundary Value Problems*, *3rd Edition*, pp. pp. 420-1, Upper Saddle River, NJ: Prentice Hall, 1998.

[10] R. Haberman, *Elementary Applied Partial Differential Equations with Fourier Series and Boundary Value Problems*, *3rd Edition*, pp. 406-8, Upper Saddle River, NJ: Prentice Hall, 1998.

[11] R. Haberman, *Elementary Applied Partial Differential Equations with Fourier Series and Boundary Value Problems*, *3rd Edition*, pp. 422-3, Upper Saddle River, NJ: Prentice Hall, 1998.

[12] S. Ramo, J. R. Whinnery, and T.V. Duzer, *Fields and Waves in Communication Electronics*, *3rd Edition*, pp. 180-4, New York, NY: John Wiley & Sons, 1993.

[13 K. Chatterjee, *Development of a Floating Random-Walk Algorithm for Solving Maxwell's Equations in Complex IC-Interconnect Structures*, pp. 153-4, Doctoral Thesis, Rensselaer Polytechnic Institute, Troy, NY, April 2002.

[14] A. Papoulis and S.U. Pillai, *Probability, Random Variable and Stochastic Processes*, *4th Edition*, McGraw Hill, 2001.

Kausik Chatterjee was born on 8 October, 1969. In June 1992, he received a Bachelor of Engineering degree in Electrical Engineering from Jadavpur University, Calcutta, India. Subsequently, in June, 1995, he received a Master of Technology degree in Nuclear Engineering from Indian Institute of Technology, Kanpur, India, and in May, 2002, he received his Ph.D degree in Electrical Engineering from Rensselaer Polytechnic Institute, Troy, New York. In August 2002, he joined the faculty, full-time, at California State University, Fresno as an Assistant Professor of Electrical and Computer Engineering. His current research interests include the development of stochastic algorithms for important equations in nature and a theory for high temperature superconductors. He has been awarded a Government of India Fellowship at Indian Institute of Technology, Kanpur, a University Fellowship at Ohio State University and an Intel Doctoral Fellowship. He has also received the Charles M. Close Doctoral Prize at Rensselaer Polytechnic Institute. He is a member of American Physical Society.

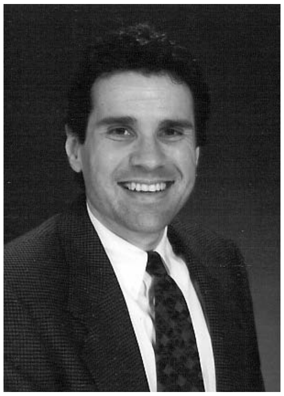

Yannick Louis Le Coz was born on 26 September 1958. In May 1980, he received a BS degree in Electrical Engineering from Rensselaer Polytechnic Institute, Troy, New York. Subsequently, in May 1982 and January 1988, respectively, he received M.S. and Ph.D. degrees in Electrical Engineering from the Massachusetts Institute of Technology, Cambridge, Massachusetts. His doctoral thesis, entitled "Semiconductor Device Simulation: A Spectral Method for Solution of the Boltzmann Transport Equation", was supervised by Prof. Alan L. McWhorter. In January 1988, he joined the faculty, full time, at Rensselaer Polytechnic Institute, as an Assistant Professor of Electrical, Computer, and Systems Engineering. He was awarded a tenured Associate Professorship in 1995. His research interests include transport in semiconductor devices, equilibrium heterojunction theory, and random-walk algorithms for the physical design of ICs. He is currently developing a novel random-walk algorithm for solving Maxwell's equations in complex, IC interconnect structures. With Dr. R.B. Iverson, he has also commercialized a random-walk IC-interconnect capacitance extractor *QuickCap*®, currently considered a "gold standard" in the chip-design industry. Dr. Le Coz has been a Digital Equipment Corporation Fellow, a Visiting Faculty at Sandia National Laboratories (Livermore, CA), a Connecticut State Scholar, and a General Motors Scholar. He has received the American Cyanamid, Perkin-Elmer, and Rensselaer Physics Awards. He is a member of Tau Beta Pi, Eta Kappa Nu, Sigma Xi, and the American Physical Society.

Implementation of Generalized Transmission-Line Equations to Transmission Line Parameter Extraction

Y. W. Liu, D. S. Zhao, and K. K. Mei

Dept. of Electronic Engineering, City University of Hong Kong
E-mail: eeliuy@cityu.edu.hk, Phone: (852) 2788-9861, Fax: (852)2788-7791

Abstract: It is usually ignored that the transmission line parameters extracted by conventional transmission line equations are variable with the internal impedance of excitation source and the loading of the line. To obtain the correct parameters, the match for both excitation and loading has to be applied. Problem is that exact matches for some extreme cases are not easy to realize. To solve this problem, in this paper, generalized transmission-line equations are implemented to the transmission-line parameter extraction with the cooperation of full-wave solver Zeland IE3D. The parameters extracted by the generalized transmission line equations are invariant to both excitation and loading. Except for this, the local radiation parameters generated from the transmission line discontinuities can also be found.

Keywords: generalized transmission line equation, parameters extraction, and invariance.

I. INTRODUCTION

For a simply shaped uniform transmission-line, its per-unit-length parameters are easily found by analytical formula and the transmission-line equations can be used to solve the line's problem with arbitrary excitation and load. For a complicatedly shaped non-uniform transmission-line, however, its per-unit-length parameters are hard to be determined by analytical formula, and have to be extracted by numerical methods. When the conventional transmission-line equations are used to extract line's per-unit-length parameters, what we find is that the extracted parameters vary with the excitation internal impedance and the line load. The reason for this is that the derivation of the conventional transmission-line equations is based on the assumption of an infinite line or non-reflection that is equivalent to the matching conditions for both excitation and load. In other words, the extracted parameters are incorrect if the matching condition for both excitation and load is not satisfied. It should be emphasized that the matched condition has been used in finding correct equation coefficients only. After the parameters (equation coefficients) are determined, the equations can be used to solve the line's problem with arbitrary excitation and load. Unfortunately, the exact matches for some extreme cases, such as a dipole antenna, are hard to be obtained. To solve this problem, in this paper, generalized transmission-line equations are implemented to the transmission-line parameter extraction. Since the derivation of the generalized transmission-line equations is based on the assumption of the finite rather than infinite line, the parameters extracted by the generalized transmission-line equations are invariance to both excitation and load. In comparison with the derivation of the conventional transmission-line equations, the generalized transmission-line equations have introduced two new terms, the dependent voltage source αV and dependent current source βI , which are interpreted as the local radiation sources. Here, V and I stand for the voltage and current at each discrete segment of the transmission-line, while α and β are the coefficients of V and I , respectively. In order to extract the line parameters by using the generalized transmission line equations, two pairs of voltage and current solutions along the line have to be used. By means of the MoM commercial software like Zeland IE3D, Sonnet, and Ensemble, the two pairs of solutions for two different loads can be obtained. Thus, the parameters can be found by substituting these two pairs of solutions into the generalized transmission line equations. The parameters extracted by the generalized equations are invariant to both internal source impedance and loads. To show the invariance of the extracted parameters to the excitation and load, in this paper, two numerical examples of microstrip line structures are given. Except for this, the local radiation effects from the discontinuities can also be obtained when the generalized equations are applied to non-uniform transmission line structures.

II. IMPLEMENTATION OF GENERALIZED EQUATIONS INTO PARAMETER EXTRACTION

As is well known, the following conventional transmission line equations have been derived from Kirchhoff's laws on a basis of an infinite-length line and TEM mode assumption [2]

$$\begin{aligned} \frac{dV(z)}{dz} &= -Z(z)\cdot I(z) \\ \frac{dI(z)}{dz} &= -Y(z)\cdot V(z) \end{aligned} \qquad (1)$$

where $Z = j\omega L + R$ and $Y = j\omega C + G$ are per-unit-length series impedance and shunt admittance, respectively. To let the equations be used, the per-unit-length line parameters L , R , C and G (i.e., coefficients of the equations) must be found by using either analytical formula or numerically extracted technique. In the past years, almost all literatures resorted to directly solving Maxwell's equations to find the parameters under static and quasi-static field assumption [2] – [5]. However, when equations (1) are used in the parameter extraction, one of things, which is easily ignored, is that the extracted parameters are directly dependant on internal impedance and line's load impedance. In other words, to obtain correct parameters, both excitation and loading matches have to be imposed so that the assumption of the infinite line can be satisfied. The problem is that exact matches at both ends of the line are not easy to realize because the characteristic impedance of the line is unknown. To solve this problem, the following generalized transmission line equations derived from a finite line [6]

$$\begin{aligned} \frac{dV}{dl} &= -Z(l)I(l) + \alpha(l)V(l) \\ \frac{dI}{dl} &= -Y(l)V(l) + \beta(l)I(l) \end{aligned} \qquad (2)$$

are implemented. For a lossless line, the distributed parameters $Z(l)$ and $Y(l)$ can be written as $j\omega L(l)$ and $j\omega C(l)$, and the corresponding definitions are exactly like those in the conventional transmission-line equations.

Comparing the conventional transmission-line equations (1), the generalized equations introduce two new parameters $\alpha(l)$ and $\beta(l)$, which can be interpreted as the coefficients of dependent voltage source and dependent current source in circuit theory, or be interpreted as the coefficients of local radiations between discontinuities of neighboring segments in field theory. When the transmission-line is a uniform structure, the values of $\alpha(l)$ and $\beta(l)$ are to be zero so that the generalized equations have the same formulations as the conventional uniform line equations. At first glance, the generalized equations seem to be more complex than the conventional equations because there are four parameters to be extracted at each discrete segment. In fact, as stated above, the two additional parameters make the extracted parameters be invariant to line's excitation and load so that the correct line's parameters can easily extracted. Since there are four line parameters $Z(l)$, $Y(l)$, $\alpha(l)$ and $\beta(l)$ at each discrete segment in generalized equations (2), we need to use two pairs of the distributed voltage and current solutions along the transmission-line to determine the line four parameters. Now most full-wave solver tools like Zeland IE3D, Sonnet, and Ensemble can be used for this purpose.

III. NUMERICAL EXAMPLES

To show how to implement the generalized equations to the line parameter extraction, the following two examples are presented. One is a finite-length uniform microstrip line. Another is a microstrip bend with two arms. For these two structures, the relative dielectric constant ε_r of the substrate is 9.8, the height *h* between the metal strip and ground is 0.635mm, the thickness *t* of the metal strip is 2μm, and the width *w* of the metal strip is 0.6mm. For simplicity, the metal are supposed to be lossless. The full-wave simulation tool, Zeland IE3D Software [7], is used to compute the distributed voltages and currents along the microstrip structures.

For the first example, the line parameters *L*(*l*), *C*(*l*), $\alpha(l)$ and $\beta(l)$ for three cases are extracted by the generalized transmission line equations. The first case is for short and open loads (A1). The second case is for the loads with complex numbers of 20+20j and 100+100j (B1). The third case is for the complex number internal impedance of 20+20j and 100+100j for excitation source (C1). The internal source impedances for the first two cases are $50\,\Omega$, and terminated load for the last case is $50\,\Omega$. All of the parameters *L*(*l*), *C*(*l*), $\alpha(l)$ and $\beta(l)$ along the uniform microstrip line found by the equations (2) are shown in Figures 1-4, respectively. It can be seen that the extracted parameters are almost the same for the three cases. This implies that the line parameters extracted by the generalized equations are invariant to

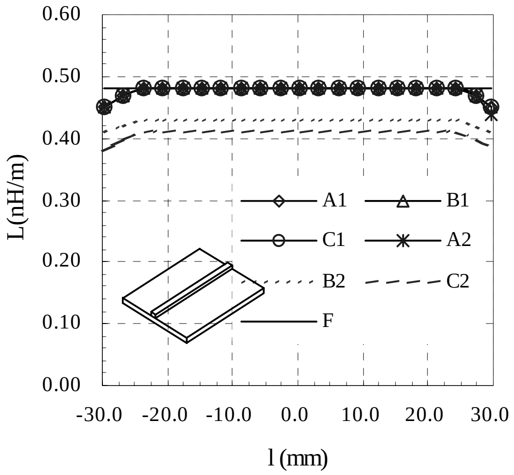

Fig. 1 Comparison of inductance obtained from generalized equations and traditional equations at 1GHz.

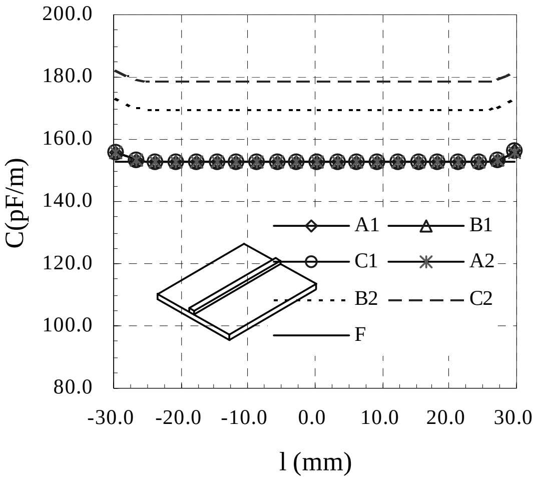

Fig. 2 Comparison of capacitance obtained from generalized equations and traditional equations at 1GHz.

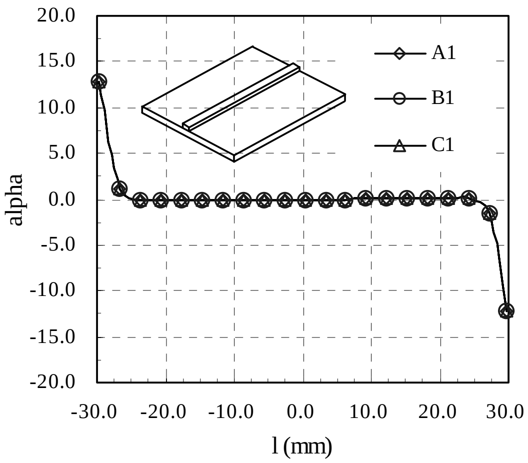

Fig. 3 Distributions of alpha obtained from generalized equations at 1GHz.

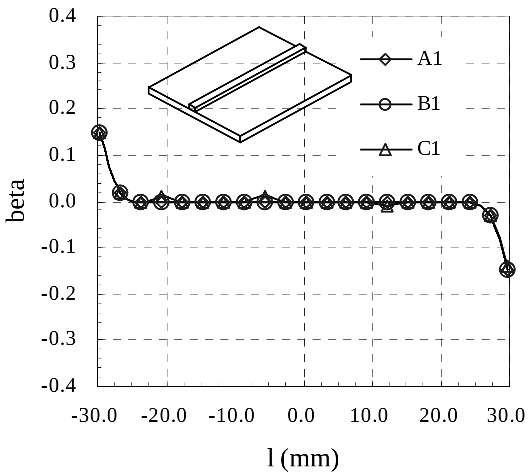

Fig. 4 Distributions of beta obtained from generalized equations at 1GHz.

both internal source impedance and termination loads. While the same cases are applied to the conventional equations (1) (corresponding to cases A2, B2 and C2), the extracted $L(l)$ and $C(l)$ are variant with both excitation and load except for the excitation and load matching conditions (case F), as show in Figs. 1 and 2. In other words, the values of $L(l)$ and $C(l)$ extracted by the conventional equations (1) at matching conditions (case F) are of a good agreement with those extracted by generalized equations (2) and calculated by analytical formulae [3], but the values of $L(l)$ and $C(l)$ extracted by the conventional equations (1) at mismatching conditions are at a great difference from those extracted with generalized equations (2). In addition, we find that the local radiation coefficients $\alpha(l)$ and $\beta(l)$, as shown in Fig. 3 and Fig. 4, are near to zero except for in the vicinity of both line ends. The non-zero $\alpha(l)$ and $\beta(l)$ in the vicinity of both line ends are reasonable because the line ends for a finite-length transmission line itself just are discontinuous places of the line. For second example, the microstrip bend is not uniform structure, so the conventional transmission line equations could not be directly applied to it. However, the generalized equations can be directly used. Two cases are calculated for this bend structure. Both cases have the excitation source of 50Ω. The first case is for short and open loads (A1). The second case is for 20+20j and 100+100j loads (B1).

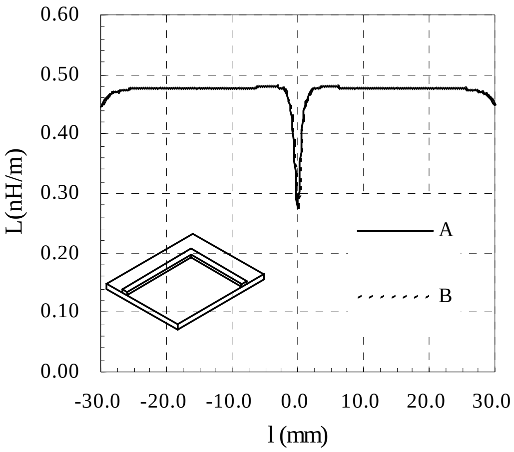

Fig. 5 Comparison of inductance obtained from generalized equations with different loads at 1GHz.

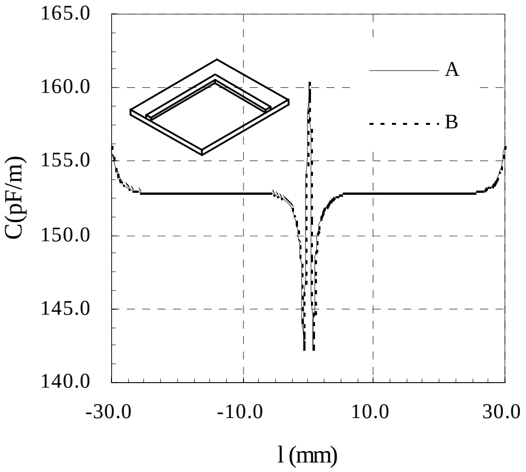

Fig. 6 Comparison of capacitance obtained from generalized equations with different loads at 1GHz.

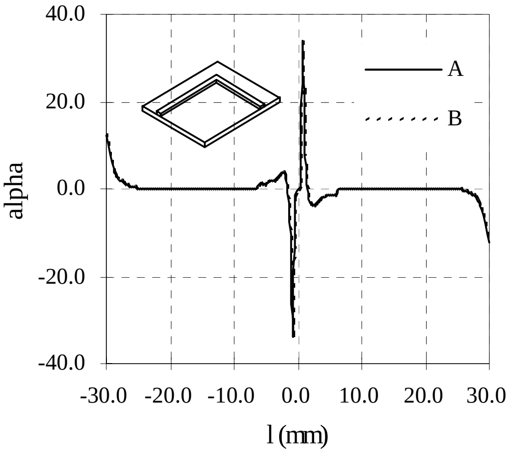

Fig. 7 Comparison of alpha obtained from generalized equations with different loads at 1GHz.

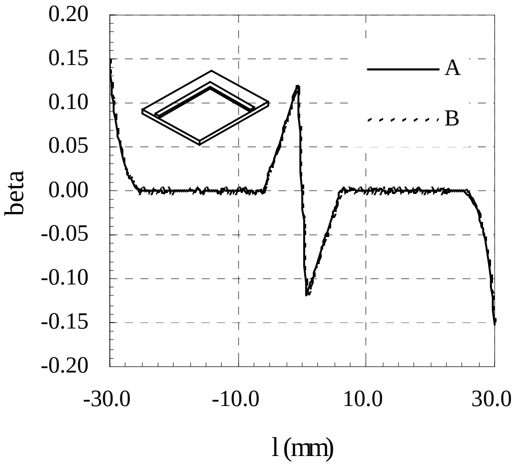

Fig. 8 Comparison of beta obtained from generalized equations with different loads at 1GHz.

The line parameters $L(l)$, $C(l)$, $\alpha(l)$ and $\beta(l)$ are extracted by the generalized equations (2). Figures 5-8 show the results of $L(l)$, $C(l)$, $\alpha(l)$ and $\beta(l)$ along the whole bend structure. For the second case, the line characteristic impedance is far away from that of traveling waves. However, like the first example, the two cases of parameters are also invariant to the port conditions. In addition, the characteristics of the bend discontinuity can be also obtained, as shown in Fig. 7 and Fig. 8, where the larger values of $\alpha(l)$ and $\beta(l)$ appear around the corner of bend while near-zero values occur at the flat part of two arms.

IV. CONCLUSION

In this paper, the generalized transmission-line equations are implemented to extract the transmission line parameters by means of numerical simulation tools like Zeland IE3D Software. The distinguished property for the general equations is that the extracted line parameters are invariant to both internal source impedance and terminated loads. Besides, the local radiation effects from line discontinuities can also be obtained during the process of the parameter extraction.

ACKNOWLEDGEMENTS

This work was partly supported by Hong Kong Research Grant Council, CERG 9040578 and Strategic Research Funds 7001130 and 7001210 at the City University of Hong Kong.

REFERENCE

[1] Y. W. Liu, J. S. Hong, and K. K. Mei, "Radiation parameter extraction from transmission-line interconnects by using method of moments solutions," *Microwave and Optical Technology Letters*, vol. 31, no.1, pp. 37-39, Oct. 2001.

[2] D. M. Pozar, Microwave Engineering (Second Edition), New York: Willey, 1998.

[3] B. C. Wadell, Transmission Line Design Handbook, Norwood: Artech House, 1991.

[4] A. Gopinath, and B. Easter, " Moment method of calculating discontinuity inductance of microstrip right-angle bends," *IEEE Transactions on Microwave Theory and Techniques*, vol. MTT-22, no.10, pp. 880-883, Dec. 1974.

[5] E. Barke, "Line-to-ground capacitance calculation for VLSI: a comparison," *IEEE Transactions on Computer-aided Design*, vol. 7, no. 2, pp. 295-298, Feb. 1988.

[6] Y. W. Liu, K. K. Mei and J. S. Hong, "Radiation extraction for transmission-line interconnects," *IEEE AP-S International Symposia*, vol. 1, pp.580 –583, July 2001.

[7] J. X. Zheng, Zeland IE3D 6.0, Zeland Software, Inc. 48890 Milmont Dr., 105D, Fremont, CA9458, USA.

Yaowu Liu received the M.S. and Ph.D. degrees from the University of Electronic Science and Technology of China, in 1981 and 1984, respectively. He was a research associate with the Department of Electrical Engineering, University of Utah, Salt Lake City, from April to November in 1986 and a research Scientist with the Department of Electrical Engineering, State University of New York at Binghamton, from May to August in 1993, respectively. From 1986 to 1995, he was a research Scientist with the Department of Electrical Engineering and Computer Science, University of California at Berkeley. Since March 1995, he has jointed in the Department of Electronic Engineering, City University of Hong Kong and now is an Assistant Professor. His research interests include electromagnetic theory and numerical computational methods to solve electromagnetic problems such as scattering, antennas, microwave circuits, and very large-scale integration interconnects.

Deshuang Zhao was born in China in 1974. He received the B.S.E.E. degree from Hennan Normal University in 1998 and the M.S.E.E degree from Electronic Science and Technology of China (UESTC) in 2001. He is now a Research Assistant in Department of Electronic Engineering, City University of Hong Kong. His research interests include electromagnetic theory, microwave circuits, and numerical method.

Kenneth K. Mei received the B.S.E.E., M.S., and Ph.D. degrees in electronic engineering from the University of Wisconsin, Madison, in1959, 1960, and 1962, respectively. He joined the faculty of the Department of Electrical Engineering and Computer Science of the University of California, Berkeley in 1962 where he was a Professor from 1972 to 1994. Since 1994 he has been a Professor in the Department of Electronic Engineering, City University of Hong Kong and now is an Adjunct Professor in Shanghai University. He was a Director of Wireless Communications Research Center, City University of Hong Kong from 1998 to 2002. He began his research in electromagnetics in the area of computation, including the method of moments, finite element/difference, hybrid methods time-domain methods and most recently, the measured equation of invariance and Maxwellian circuits.

Dr. Mei received the Best Paper Award and Honourable Mention of the Best Paper Award in 1967 and 1974, respectively, from the IEEE Antennas and Propagation Society. He is a member of RSI/USNC.

ACES COPYRIGHT FORM

This form is intended for original, previously unpublished manuscripts submitted to ACES periodicals and conference publications. The signed form, appropriately completed, MUST ACCOMPANY any paper in order to be published by ACES. PLEASE READ REVERSE SIDE OF THIS FORM FOR FURTHER DETAILS.

TITLE OF PAPER:

AUTHORS(S)

PUBLICATION TITLE/DATE:

RETURN FORM TO:
Dr. Atef Z. Elsherbeni
University of Mississippi
Dept. of Electrical Engineering
Anderson Hall Box 13
University, MS 38677 USA

PART A - COPYRIGHT TRANSFER FORM

(NOTE: Company or other forms may not be substituted for this form. U.S. Government employees whose work is not subject to copyright may so certify by signing Part B below. Authors whose work is subject to Crown Copyright may sign Part C overleaf).

The undersigned, desiring to publish the above paper in a publication of ACES, hereby transfer their copyrights in the above paper to The Applied Computational Electromagnetics Society (ACES). The undersigned hereby represents and warrants that the paper is original and that he/she is the author of the paper or otherwise has the power and authority to make and execute this assignment.

Returned Rights: In return for these rights, ACES hereby grants to the above authors, and the employers for whom the work was performed, royalty-free permission to:

1. Retain all proprietary rights other than copyright, such as patent rights.
2. Reuse all or portions of the above paper in other works.
3. Reproduce, or have reproduced, the above paper for the author's personal use or for internal company use provided that (a) the source and ACES copyright are indicated, (b) the copies are not used in a way that implies ACES endorsement of a product or service of an employer, and (c) the copies per se are not offered for sale.
4. Make limited distribution of all or portions of the above paper prior to publication.
5. In the case of work performed under U.S. Government contract, ACES grants the U.S. Government royalty-free permission to reproduce all or portions of the above paper, and to authorize others to do so, for U.S. Government purposes only.

ACES Obligations: In exercising its rights under copyright, ACES will make all reasonable efforts to act in the interests of the authors and employers as well as in its own interest. In particular, ACES REQUIRES that:

1. The consent of the first-named author be sought as a condition in granting re-publication permission to others.
2. The consent of the undersigned employer be obtained as a condition in granting permission to others to reuse all or portions of the paper for promotion or marketing purposes.

In the event the above paper is not accepted and published by ACES or is withdrawn by the author(s) before acceptance by ACES, this agreement becomes null and void.

AUTHORIZED SIGNATURE — TITLE (IF NOT AUTHOR)

EMPLOYER FOR WHOM WORK WAS PERFORMED — DATE FORM SIGNED

Part B - U.S. GOVERNMENT EMPLOYEE CERTIFICATION

(NOTE: if your work was performed under Government contract but you are not a Government employee, sign transfer form above and see item 5 under Returned Rights).

This certifies that all authors of the above paper are employees of the U.S. Government and performed this work as part of their employment and that the paper is therefor not subject to U.S. copyright protection.

AUTHORIZED SIGNATURE — TITLE (IF NOT AUTHOR)

NAME OF GOVERNMENT ORGANIZATION — DATE FORM SIGNED

PART C - CROWN COPYRIGHT

(NOTE: ACES recognizes and will honor Crown Copyright as it does U.S. Copyright. It is understood that, in asserting Crown Copyright, ACES in no way diminishes its rights as publisher. Sign only if *ALL* authors are subject to Crown Copyright).

This certifies that all authors of the above Paper are subject to Crown Copyright. (Appropriate documentation and instructions regarding form of Crown Copyright notice may be attached).

AUTHORIZED SIGNATURE TITLE OF SIGNEE

NAME OF GOVERNMENT BRANCH DATE FORM SIGNED

Information to Authors

ACES POLICY

ACES distributes its technical publications throughout the world, and it may be necessary to translate and abstract its publications, and articles contained therein, for inclusion in various compendiums and similar publications, etc. When an article is submitted for publication by ACES, acceptance of the article implies that ACES has the rights to do all of the things it normally does with such an article.

In connection with its publishing activities, it is the policy of ACES to own the copyrights in its technical publications, and to the contributions contained therein, in order to protect the interests of ACES, its authors and their employers, and at the same time to facilitate the appropriate re-use of this material by others.

The new United States copyright law requires that the transfer of copyrights in each contribution from the author to ACES be confirmed in writing. It is therefore necessary that you execute either Part A-Copyright Transfer Form or Part B-U.S. Government Employee Certification or Part C-Crown Copyright on this sheet and return it to the Managing Editor (or person who supplied this sheet) as promptly as possible.

CLEARANCE OF PAPERS

ACES must of necessity assume that materials presented at its meetings or submitted to its publications is properly available for general dissemination to the audiences these activities are organized to serve. It is the responsibility of the authors, not ACES, to determine whether disclosure of their material requires the prior consent of other parties and if so, to obtain it. Furthermore, ACES must assume that, if an author uses within his/her article previously published and/or copyrighted material that permission has been obtained for such use and that any required credit lines, copyright notices, etc. are duly noted.

AUTHOR/COMPANY RIGHTS

If you are employed and you prepared your paper as a part of your job, the rights to your paper initially rest with your employer. In that case, when you sign the copyright form, we assume you are authorized to do so by your employer and that your employer has consented to all of the terms and conditions of this form. If not, it should be signed by someone so authorized.

NOTE RE RETURNED RIGHTS: Just as ACES now requires a signed copyright transfer form in order to do “business as usual”, it is the intent of this form to return rights to the author and employer so that they too may do “business as usual”. If further clarification is required, please contact: The Managing Editor, R. W. Adler, Naval Postgraduate School, Code EC/AB, Monterey, CA, 93943, USA (408)656-2352.

Please note that, although authors are permitted to re-use all or portions of their ACES copyrighted material in other works, this does not include granting third party requests for reprinting, republishing, or other types of re-use.

JOINT AUTHORSHIP

For jointly authored papers, only one signature is required, but we assume all authors have been advised and have consented to the terms of this form.

U.S. GOVERNMENT EMPLOYEES

Authors who are U.S. Government employees are not required to sign the Copyright Transfer Form (Part A), but any co-authors outside the Government are.

Part B of the form is to be used instead of Part A only if all authors are U.S. Government employees and prepared the paper as part of their job.

NOTE RE GOVERNMENT CONTRACT WORK: Authors whose work was performed under a U.S. Government contract but who are not Government employees are required so sign Part A-Copyright Transfer Form. However, item 5 of the form returns reproduction rights to the U. S. Government when required, even though ACES copyright policy is in effect with respect to the reuse of material by the general public.

January 2002

APPLIED COMPUTATIONAL ELECTROMAGNETICS SOCIETY JOURNAL
http://aces.ee.olemiss.edu

INFORMATION FOR AUTHORS

PUBLICATION CRITERIA

Each paper is required to manifest some relation to applied computational electromagnetics. **Papers may address general issues in applied computational electromagnetics, or they may focus on specific applications, techniques, codes, or computational issues.** While the following list is not exhaustive, each paper will generally relate to at least one of these areas:

1. **Code validation.** This is done using internal checks or experimental, analytical or other computational data. Measured data of potential utility to code validation efforts will also be considered for publication.

2. **Code performance analysis.** This usually involves identification of numerical accuracy or other limitations, solution convergence, numerical and physical modeling error, and parameter tradeoffs. However, it is also permissible to address issues such as ease-of-use, set-up time, run time, special outputs, or other special features.

3. **Computational studies of basic physics.** This involves using a code, algorithm, or computational technique to simulate reality in such a way that better, or new physical insight or understanding, is achieved.

4. **New computational techniques**, or new applications for existing computational techniques or codes.

5. **"Tricks of the trade"** in selecting and applying codes and techniques.

6. **New codes, algorithms, code enhancement, and code fixes.** This category is self-explanatory, but includes significant changes to existing codes, such as applicability extensions, algorithm optimization, problem correction, limitation removal, or other performance improvement. **Note: Code (or algorithm) capability descriptions are not acceptable, unless they contain sufficient technical material to justify consideration.**

7. **Code input/output issues.** This normally involves innovations in input (such as input geometry standardization, automatic mesh generation, or computer-aided design) or in output (whether it be tabular, graphical, statistical, Fourier-transformed, or otherwise signal-processed). Material dealing with input/output database management, output interpretation, or other input/output issues will also be considered for publication.

8. **Computer hardware issues.** This is the category for analysis of hardware capabilities and limitations of various types of electromagnetics computational requirements. Vector and parallel computational techniques and implementation are of particular interest.

Applications of interest include, but are not limited to, antennas (and their electromagnetic environments), networks, static fields, radar cross section, shielding, radiation hazards, biological effects, electromagnetic pulse (EMP), electromagnetic interference (EMI), electromagnetic compatibility (EMC), power transmission, charge transport, dielectric, magnetic and nonlinear materials, microwave components, MEMS technology, MMIC technology, remote sensing and geometrical and physical optics, radar and communications systems, fiber optics, plasmas, particle accelerators, generators and motors, electromagnetic wave propagation, non-destructive evaluation, eddy currents, and inverse scattering.

Techniques of interest include frequency-domain and time-domain techniques, integral equation and differential equation techniques, diffraction theories, physical optics, moment methods, finite differences and finite element techniques, modal expansions, perturbation methods, and hybrid methods. This list is not exhaustive.

A unique feature of the Journal is the publication of unsuccessful efforts in applied computational electromagnetics. Publication of such material provides a means to discuss problem areas in electromagnetic modeling. Material representing an unsuccessful application or negative results in computational electromgnetics will be considered for publication only if a reasonable expectation of success (and a reasonable effort) are reflected. Moreover, such material must represent a problem area of potential interest to the ACES membership.

Where possible and appropriate, authors are required to provide statements of quantitative accuracy for measured and/or computed data. This issue is discussed in "Accuracy & Publication: Requiring, quantitative accuracy statements to accompany data," by E. K. Miller, *ACES Newsletter,* Vol. 9, No. 3, pp. 23-29, 1994, ISBN 1056-9170.

EDITORIAL REVIEW

In order to ensure an appropriate level of quality control, papers are refereed. They are reviewed both for technical correctness and for adherence to the listed guidelines regarding information content.

JOURNAL CAMERA READY SUBMISSIN DATES

March issue	deadline 8 January
July issue	deadline 20 May
November issue	deadline 20 September

Uploading an acceptable camera ready article after the deadlines will result in a delay in publishing this article.

STYLE FOR CAMERA-READY COPY

The ACES Journal is flexible, within reason, in regard to style. However, certain requirements are in effect:

1. The paper title should NOT be placed on a separate page. The title, author(s), abstract, and (space permitting) beginning of the paper itself should all be on the first page. The title, author(s), and author affiliations should be centered (center-justified) on the first page.

2. An abstract is REQUIRED. The abstract should be a brief summary of the work described in the paper. It should state the computer codes, computational techniques, and applications discussed in the paper (as applicable) and should otherwise be usable by technical abstracting and indexing services.

3. Either British English or American English spellings may be used, provided that each word is spelled consistently throughout the paper.

4. Any commonly-accepted format for referencing is permitted, provided that internal consistency of format is maintained. As a guideline for authors who have no other preference, we recommend that references be given by author(s) name and year in the body of the paper (with alphabetical listing of all references at the end of the paper). Titles of Journals, monographs, and similar publications should be in italic font or should be underlined. Titles of papers or articles should be in quotation marks.

5. Internal consistency shall also be maintained for other elements of style, such as equation numbering. As a guideline for authors who have no other preference, we suggest that equation numbers be placed in parentheses at the right column margin.

6. The intent and meaning of all text must be clear. For authors who are NOT masters of the English language, the ACES Editorial Staff will provide assistance with grammar (subject to clarity of intent and meaning).

7. Unused space should be minimized. Sections and subsections should not normally begin on a new page.

MATERIAL, SUBMITTAL FORMAT AND PROCEDURE

The preferred format for submission and subsequent review, is 12 point font or 12 cpi, double line spacing and single column per page. All submissions should be uploaded to ACES server through ACES web site (http://aces.ee.olemiss.edu) by using the upload button, journal section. Only pdf files are accepted for submission. The file size should not be larger than 5MB, otherwise permission from the Editor-in-Chief should be obtained first. The Editor-in-Chief will acknowledge the electronic submission a few minutes after the upload process is successfully completed

Only camera-ready electronic files are accepted for publication. The term **"camera-ready" means that the material is neat, legible, and reproducible.** The preferred style is Times Roman 10 point (or equivalent) such as that used in this text. A double column format similar to that used here is required. Full details can be found on ACES site, Journal section.

ACES reserves the right to edit any uploaded material, however, this is not generally done. It is the author(s) responsibility to provide acceptable camera ready pdf files. Incompatible or incomplete pdf files will not be processed, and authors will be requested to re-upload revised acceptable version.

COPYRIGHTS AND RELEASES

Each primary author must sign a copyright form and obtain a release from his/her organization vesting the copyright with ACES. Copyright forms are available at ACES, web site (http://aces.ee.olemiss.edu). To shorten the review process time, the executed copyright form should be forwarded to the Editor-in-Chief immediately after the completion of the upload (electronic submission) process. Both the author and his/her organization are allowed to use the copyrighted material freely for their own private purposes.

Permission is granted to quote short passages and reproduce figures and tables from and ACES Journal issue provided the source is cited. Copies of ACES Journal articles may be made in accordance with usage permitted by Sections 107 or 108 of the U.S. Copyright Law. This consent does not extend to other kinds of copying, such as for general distribution, for advertising or promotional purposes, for creating new collective works, or for resale. The reproduction of multiple copies and the use of articles or extracts for commercial purposes require the consent of the author and specific permission from ACES. Institutional members are allowed to copy any ACES Journal issue for their internal distribution only.

PUBLICATION CHARGES

ACES members are allowed 12 printed pages per paper without charge; non-members are allowed 8 printed pages per paper without charge. Mandatory page charges of $75 a page apply to all pages in excess of 12 for members or 8 for non-members. Voluntary page charges are requested for the free (12 or 8) pages, but are NOT mandatory or required for publication. A priority courtesy guideline, which favors members, applies to paper backlogs. Authors are entitled to 15 free reprints of their articles and must request these from the Managing Editor. Additional reprints are available to authors, and reprints available to non-authors, for a nominal fee.

ACES Journal is abstracted in INSPEC, in Engineering Index, and in DTIC.